Lateral vehicle dynamics control and vehicle state estimation: A tyre force measurement based approach

Kunnappillil Madhusudhanan, Anil

DOI
10.4233/uuid:9cadd5c4-0a61-49ad-9fb7-8d0d2b07dc65

Publication date
2016

Document Version
Final published version

Citation (APA)
Kunnappillil Madhusudhanan, A. (2016). *Lateral vehicle dynamics control and vehicle state estimation: A tyre force measurement based approach*. [Dissertation (TU Delft), Delft University of Technology]. https://doi.org/10.4233/uuid:9cadd5c4-0a61-49ad-9fb7-8d0d2b07dc65

Important note
To cite this publication, please use the final published version (if applicable).
Please check the document version above.

LATERAL VEHICLE DYNAMICS CONTROL AND VEHICLE STATE ESTIMATION

A TYRE FORCE MEASUREMENT BASED APPROACH

Proefschrift

ter verkrijging van de graad van doctor
aan de Technische Universiteit Delft,
op gezag van de Rector Magnificus prof. ir. K.C.A.M. Luyben,
voorzitter van het College voor Promoties,
in het openbaar te verdedigen op
woensdag 22 juni 2016 om 15:00 uur

door

Anil KUNNAPPILLIL MADHUSUDHANAN

Ingenieur Systems and Control,
Technische Universiteit Delft, Nederland,
geboren te Thodupuzha, India.

Dit proefschrift is goedgekeurd door de

promotors: prof. dr. ir. E.G.M. Holweg en prof. dr. ir. M. Corno

Samenstelling promotiecommissie:

Rector Magnificus,	voorzitter
Prof. dr. ir. E.G.M. Holweg,	Technische Universiteit Delft
Prof. dr. ir. M. Corno,	Politecnico di Milano, Italy
Onafhankelijke leden:	
Prof. dr. ir. J. Hellendoorn,	Technische Universiteit Delft
Prof. dr. ir. N. van de Wouw,	Technische Universiteit Eindhoven
Prof. dr. ir. B. Jacobson,	Chalmers Tekniska Högskola, Sweden
Dr. ir. R. Happee,	Technische Universiteit Delft
Dr. ir. W. Pasillas-Lépine,	CNRS-L2S-Supélec, France

The research in this thesis was supported by TNO Automotive, Helmond and SKF Automotive Division, Nieuwegein.

Keywords: Vehicle Dynamics Control, Road-Tyre friction, Vehicle Sideslip, Vehicle Yaw Rate, Tyre Utilization Coefficient.

Printed by: Gildeprint, Enschede, the Netherlands

Front & Back: A. Kunnappillil Madhusudhanan

ISBN/EAN: 978-94-6186-668-4

An electronic version of this dissertation is available at
http://repository.tudelft.nl/.

To Indira, Madhu, Haridas, Arun and Lakshmi.

CONTENTS

SUMMARY

In assessing and controlling vehicle dynamics, tyre forces are the most important variables as they are the only points of interaction with the road. Estimating tyre forces is difficult because of their nonlinear characteristics. Therefore, most of the lateral vehicle dynamics controllers and estimators in the literature use a tyre model that introduces modeling error because of the tyre model nonlinearities and uncertainties. This may degrade the controller and estimator performance. On the other hand, modeling with tyre force measurements improves the model accuracy and therefore might improve the controller and estimator performance.

The primary objective of this PhD research is to study the benefits of tyre force measurement on lateral Vehicle Dynamics Control (VDC) and Vehicle State Estimation (VSE). The lateral VDCs and VSEs studied in this dissertation are therefore based on tyre force measurement. This PhD research is a part of an ongoing research at TU Delft on Load Sensing Bearing (LSB) based VDC. The LSB technology is invented at SKF and it measures individual tyre forces. In the previous PhD dissertation, longitudinal VDC using the LSB technology has been the main focus of research. In this PhD dissertation, lateral VDCs and VSEs using tyre force measurements are studied.

This dissertation shows that the force based methods can be adapted to many VDC aspects. In particular, the contributions of this dissertation are the proposed Tyre Utilization Coefficients Control using steering actuators, yaw rate control using braking actuators, vehicle sideslip estimator and the road-tyre friction estimator considering combined tyre slip. The estimators are also validated using test data. Overall, this dissertation offers a positive recommendation on LSB based VDC and VSE but more work needs to be done on the LSB technology.

SAMENVATTING

In de beoordeling en controle van de voertuigdynamiek, band krachten zijn de belangrijkste variabelen zoals ze zijn het enige interactie met de weg. Schatten band forces is lastig vanwege hun niet-lineaire kenmerken. Het merendeel van de laterale voertuigdynamiek controllers en afvalgerelateerde schatters in de literatuur gebruik een bandtype dat introduceert modelling fout vanwege het bandenmodel nonlinearities en onzekerheden. Dit kan een negatieve invloed hebben op de controller en schatter prestaties. Aan de andere kant, modeling met band kracht metingen verbetert het model accuraat en dus betere controller en schatter prestaties.

Het primaire doel van dit promotieonderzoek is het bestuderen van de voordelen van band krachtmeting op laterale voertuigdynamica en raming. De laterale voertuigdynamiek controllers (VDC) en afvalgerelateerde schatters (VSE) studeerde in dit proefschrift zijn dus gebaseerd op bandenmaat kracht meting. Dit promotieonderzoek maakt deel uit van een lopend onderzoek aan de TU Delft op Load Sensing lager (LSB) gebaseerde voertuigdynamica. De LSB-technologie is uitgevonden op SKF en kunt meten individuele band krachten. In de vorige proefschrift, overlangse voertuigdynamica met het LSB-technologie is het belangrijkste aandachtspunt van het onderzoek. In dit proefschrift, laterale voertuigdynamica en schatting met band kracht metingen worden bestudeerd.

Dit proefschrift laat zien dat de kracht gebaseerde werkwijzen kunnen worden aangepast aan vele aspecten VDC. Met name de bijdragen van dit proefschrift zijn de voorgestelde Tyre Gebruik coefficienten controle met behulp van besturing actuators, gierhoeksensor controle met behulp van remmen actuatoren, voertuig sideslip schatter en de weg-band wrijving schatter overweegt gecombineerd band slip. De schatters zijn ook gevalideerd met testgegevens. Kortom, dit proefschrift heeft een positief advies over LSB gebaseerd VDC en VSE, maar meer werk moet worden gedaan aan de LSB-technologie.

1

INTRODUCTION

SAFE vehicles are important in today's world which is strongly dependent on vehicles. Figure 1.1 shows the world car population during the period 2006 – 13 [1]. It is interesting to observe that even during the major financial crisis of 2007 – 08, the number of passenger cars kept increasing. This demonstrates our strong dependency on vehicles. As the number of vehicles increases, unless sufficient preventive measures are taken, it is difficult to reduce the number of fatal accidents.

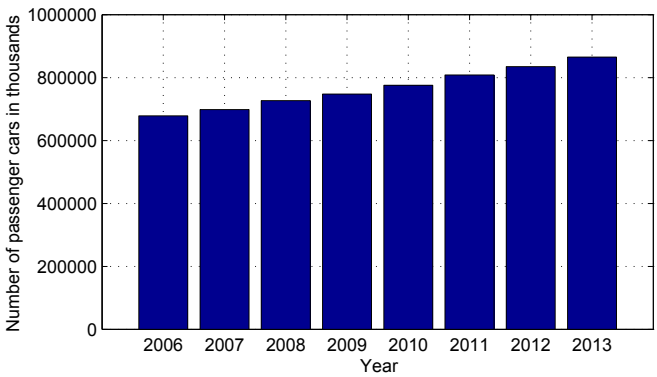

Figure 1.1: World car population during the period 2006 – 13.

According to the Association For Safe International Road Travel (ASIRT), road accidents cause approximately 3287 deaths per day worldwide and they are the leading cause of death among young people in the age group 15 – 29. In addition, these accidents cost approximately 518 billion USD per year which is approximately 1.42 billion USD per day. These are unacceptable human and financial losses. Therefore, it is crucial to make driving safer so that the fatal accidents could be reduced as much as possible. As shown in Figure 1.2, there are mainly three areas of improvement to reduce these losses. First is to

improve the quality of drivers using better driver trainings. The second is to improve the vehicle transport infrastructure, and the third is to improve vehicle safety using vehicle safety systems.

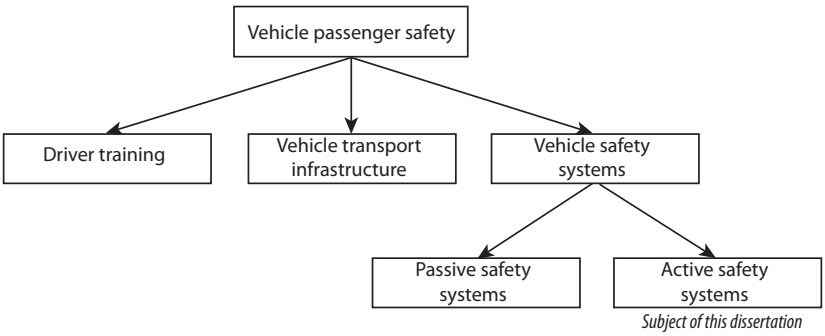

Figure 1.2: Different areas of improvement for better vehicle passenger safety.

Further, as shown in Figure 1.2, vehicle safety systems can be categorized into passive safety systems and active safety systems. Passive safety systems attempt to reduce the degree of human injuries once an accident has happened, for example, airbag and seat belt systems. On the other hand, active safety systems monitor the vehicle state and in case the system detects an undesirable state, they apply automatic correction using braking or steering actuator to prevent an accident from happening. Some vehicles are also equipped with pre-crash systems that provide warning to the driver in case of an impending accident. Their functions might also include pretensioning the front seat belts, closing the windows and bringing the front seats to an upright position. Some vehicles are nowadays equipped with post-crash systems that automatically inform the emergency services as soon as an accident has happend because the first hour is the most crucial in accidents causing serious human injuries. In this dissertation, different components of the active safety systems are studied. They are studied using tyre force measurement based approach where the tyre-road forces of individual tyres are measured.

A typical active safety system has five major components as shown in Figure 1.3; sensors, estimator, reference generator, controller and actuators. The sensors measure some of the variables that describe the vehicle motion such as longitudinal and lateral accelerations, angular velocities and yaw rate, whereas the estimator estimates the important vehicle variables that are not measured, for example vehicle longitudinal and lateral velocities. The reference generator generates reference values of the vehicle variables that are controlled by the controller and the control action is realized using the available actuators, for example braking actuator and/or steering actuators.

In addition to conventional driver driven vehicles, active safety systems are crucial in the growing field of autonomous driving [2, 3]. Instead of the *Driver* block in Figure 1.3, autonomous vehicles are designed to follow a reference trajectory using steering, braking and throttle actuators, and active safety systems. For example, Adaptive Cruise Control is an important active safety system for autonomouse vehicles as it maintains safe distance from the vehicles ahead. The reference trajectory of an autonomouse ve-

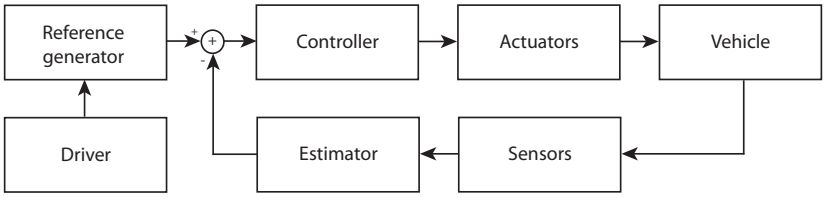

Figure 1.3: Block diagram of a typical active safety system.

hicle is typically generated using the passenger destination, multiple sensor inputs and a trajectory model.

The controller in Figure 1.3 can be categorized into longitudinal, lateral and vertical dynamics control. This dissertation focuses on two types of Lateral Vehicle Dynamics Control (LVDC) schemes; Tyre Utilization Coefficient Control (TUCC) and Yaw Rate Control. Tyre Utilization Coefficient (TUC) is an indication of how much the tyre is engaged with respect to the maximum force it can exert. LVDC is an important research area as unstable lateral vehicle dynamics can potentially result in accidents where the vehicle gets into the wrong lane or even outside the road, both of which can be dangerous. This dissertation also focuses on road-tyre friction estimator and vehicle sideslip estimator as they are needed to implement the TUCC and Yaw Rate Control. Vehicle sideslip is defined as the angle between the vehicle longitudinal axis and the vehicle velocity vector.

1.1. PRIMARY OBJECTIVE OF THIS DISSERTATION

THE primary objective of this dissertation is to study the benefits of tyre force measurement on active safety systems for lateral vehicle dynamics. The controllers and estimators studied in this dissertation are therefore based on tyre force measurement.

This dissertation is a part of an ongoing research at Delft University of Technology on Load Sensing Bearing (LSB) based active safety systems. The LSB technology is invented at SKF [60] and it measures individual tyre forces. In the previous PhD dissertation [4], longitudinal vehicle dynamics control using the LSB technology has been the main focus of research [14–16]. In this dissertation, lateral vehicle dynamics control and estimation using tyre force measurements are studied. In the next section, tyre force measurement is introduced.

1.2. TYRE FORCE MEASUREMENT

CURRENTLY, the state-of-the-art tyre force sensing is represented by measurement wheels (for example the Corrsys system [62]). These systems are accurate, but are not viable for commercial use because of their cost, encumbrance and complex calibration procedures. In the past few years, several solutions to provide more cost-effective tyre force sensing have been proposed. Some of them are Load Sensing Bearing (LSB) technology from SKF [14, 60], embedded force sensor [50], lateral tyre force sensor from NSK [51–53] and wheel force transducer proposed in [54]. Although none of them is currently at production level, cost effective tyre force sensing is expected to become a reality. The embedded force sensor proposed in [50] embeds the sensor inside the tyre as a small

patch. Therefore, there is only one measurement per revolution. In [51–53], the lateral tyre force sensor from NSK is used to control vehicle motion. However, for sideslip estimation, the longitudinal tyre forces are also required if the vehicle is not travelling at a constant speed. The embedded force sensor in [50] and the wheel force transducer in [54] require wireless transmission of the measurements. The Load Sensing Bearing (LSB) technology from SKF [60] is one of the most interesting solutions because it estimates tyre forces in addition to their primary objective of acting as a bearing. The main advantage against other tyre-based sensors is that the sensing mechanism in installed on a non-rotating element that is not subject to tear as the tyre is. Its potential applications in active safety systems are studied in this dissertation.

The LSB technology is discussed further in Chapter 2. In the following sections, each of the controllers and estimators studied in this dissertation is introduced.

1.3. TYRE UTILIZATION COEFFICIENT CONTROL

LATERAL vehicle dynamics controllers (LVDC) are used to improve vehicle performance and safety. They keep the vehicle stable when a driver pushes the vehicle towards its unstable region of operation. An average skilled driver might do so as parameters such as tyre-road friction and vehicle load are prone to change depending on different driving conditions.

The literature on LVDC is rich and diverse. Many of the existing systems are based on yaw rate measurement. Vehicle yaw rate is compared with a reference and a corrective control is applied using braking or steering actuators [5–7]. Another LVDC approach is to act up on the error between estimated vehicle sideslip and its reference [8]. The yaw rate based approaches are limited because a reasonable yaw rate reference model requires the knowledge of the surface to calculate the maximum yaw rate reference magnitude. The sideslip based approaches are more robust to changes of surface, but a reliable, robust and cost-effective estimation of the sideslip is still an open problem [9, 10] because of the nonlinearities and uncertainties of the sideslip model.

In [5], a linear tyre model is used and this might cause the yaw rate control action to be not optimal when the tyres are in the nonlinear operating region. In [6], the nonlinear tyre model from Pacejka [11] is used to address this issue. However, the nonlinear tyre model from Pacejka is prone to change as the friction characteristic changes. Then the tyre force calculations may not be correct and therefore control action using yaw rate or vehicle sideslip may not be optimal. However, the yaw rate and vehicle sideslip dynamics are dependent on tyre forces, and undesired yaw rate or vehicle sideslip is a result of undesired tyre forces. Therefore, controlling tyre forces instead of yaw rate or vehicle sideslip could bring considerable benefits in stability and performance.

1.3.1. CONTRIBUTIONS OF THIS DISSERTATION

The recent introduction of tyre force sensing technology [14] facilitates tyre force based control. This paradigm avoids the need of complex estimation algorithms and at the same time directly accounts for road conditions. Tyre force based control has proven successful in longitudinal vehicle dynamics control [14–16]; this dissertation investigates the potential of a force based LVDC called Tyre Utilization Coefficient Control (TUCC).

TUC is an indication of how much the tyre is engaged with respect to the maximum force it can exert. The basic principle of the TUCC is to equalize the left and right TUCs of the front axle using active independent front steering. By doing so, saturation during cornering can be avoided or delayed, thereby improving stability. Although steer-by-wire is not yet an off-the-shelf technology, active steering is being researched very actively. This warrants the study and design of VDC systems based on active steering. With the availability of force sensors as discussed in section 1.2, measuring tyre forces and therefore calculating and controlling TUCs is feasible.

The TUCC employs independent front wheel steering actuators and it does not use braking actuators. The proposed TUCC has the following properties.

- The nonlinearities and uncertainties of the vehicle model are considered. In order to address them, an output tracking Sliding Mode Control (SMC) is designed and validated. The final SMC is gain scheduled with respect to vehicle velocity.
- An active steering system model is considered to incorporate steering actuator dynamics.
- The effect of the proposed controller on vehicle lateral acceleration is studied. On a typical dry road, as shown in Figure 1.4, the lateral tyre force has a peak value corresponding to a certain tyre side slip angle. This implies that, if a driver applies more steering assuming he will get more lateral acceleration and stability is not lost in the process, he might in fact be settling for a lower lateral acceleration. With the proposed controller, a vehicle can maintain the maximum possible lateral tyre forces and therefore maintain the maximum possible lateral acceleration for higher steering angles.

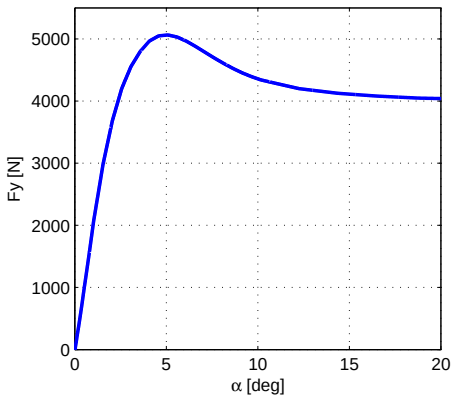

Figure 1.4: Typical lateral tyre force characteristics on a dry road.

- The SMC is studied for its robustness against vehicle velocity, force measurement noise and road-tyre friction.

The proposed TUCC is discussed in detail in Chapter 3. In the next section, the yaw rate control problem is introduced.

1

1.4. YAW RATE CONTROL

As discussed in the previous section, vehicle safety systems are increasingly present in today's passenger cars as they are effective in reducing fatal accidents [29]. For example, electronic stability control (ESC) is able to reduce fatal accidents by approximately 23% [30]. An ESC, also know as LVDC, controls vehicle yaw rate or vehicle sideslip angle or both to keep the vehicle stable in the lateral direction.

Literature on yaw rate control is quite diverse. Several control methods are studied in the literature because of its nonlinear dynamics and uncertainties based on external factors such as temperature, road friction, etc. In [31, 32], an optimal yaw moment control is proposed using Linear Quadratic Regulator (LQR) theory and is found to be effective in improving lateral stability. However in the vehicle model, tyre models are linearized using cornering stiffness. This might cause the control to be non optimal as the tyre behavior is nonlinear, which in turn might affect the controller robustness. In addition, linearizing the tyre models introduces speed dependency on the vehicle model. This might make the closed loop performance sensitive to vehicle speed.

In [33], in order to account for the linearization errors, an H_∞ based yaw moment controller is designed using μ analysis, considering the vehicle nonlinearities as uncertainty. Although this approach is robust compared to a LQR, the resulting controller might be conservative. In [34], yaw moment control is realized with an adaptive control law which is updated based on estimated cornering stiffness. Although it shows positive simulation results in terms of stabilizing the vehicle, there are high yaw rate oscillations of the order 34 deg/s and the cornering stiffness estimate seems to saturate during steady state to an incorrect value. In [35], a State Dependent Riccati Equation based control is proposed to account for the linearization errors. Although the closed loop performance may be better than a LQR, it is computationally expensive and therefore needs a powerful processor for implementation.

1.4.1. CONTRIBUTIONS OF THIS DISSERTATION

In this dissertation, yaw rate control is studied without linearizing the yaw rate dynamics. As a result, the control design and control gain do not directly depend upon the vehicle speed and vehicle sideslip. This is achieved by combining tyre force sensing and Lyapunov function based control. The objective here is to design a yaw rate controller, given a typical consumer car and tyre force sensors. The proposed controller is therefore designed using braking actuators and it does not use steering actuators. In addition, the controller is computationally inexpensive due to its simplicity.

The proposed yaw rate control is discussed in detail in Chapter 4. In the next section, the road-tyre friction estimation is introduced.

1.5. ROAD-TYRE FRICTION ESTIMATION

ROAD-TYRE friction is an important variable for active safety systems such as ESC, Anti-lock Braking System (ABS), Traction Control System (TCS) and Adaptive Cruise Control (ACC), especially during winter. It is defined as the maximum force the tyre can exert, normalized by the vertical load. Availability of road-tyre friction helps in estimating the physical limits of the vehicle, and therefore, may improve ESC, ABS, TCS and ACC

performance. Road-tyre friction estimator is needed to implement the TUCC in Chapter 3 and it can improve the yaw rate controller proposed in Chapter 4.

There are several methods in the literature on the topic of friction estimation. Some of them use longitudinal tyre dynamics and some, lateral tyre dynamics. In [44], a friction estimator is proposed based on LuGre friction model and the longitudinal dynamics. Although the paper shows interesting results, as only longitudinal tyre dynamics is considered, the method might be inaccurate in the presense of lateral tyre dynamics. In addition, there is an assumption that the LuGre friction model represents the tyre forces accurately. In [23, 45, 46], real-time friction estimators are proposed based on the assumption that there is a linear relationship between the slope of longitudinal tyre slip versus longitudinal tyre force characteristics and friction as shown in Figure 1.5. These methods are effective only during the linear region of the tyre force characteristics, and as the tyre forces are estimated, the estimate accuracy depends heavily on the accuracy of the force estimates. In addition, the method requires the vehicle to drive straight which is not realisitic, especially during critical maneuvers. In [46], it is concluded that the longitudinal slip-force slope based friction estimate error is significant because of the significant noise levels in the slope estimate. The parameter changes such as tyre type, temperature and tyre stiffness affect the relationship between the slope and friction. These parameter uncertainties affect the longitudinal slip-force slope based estimator robustness.

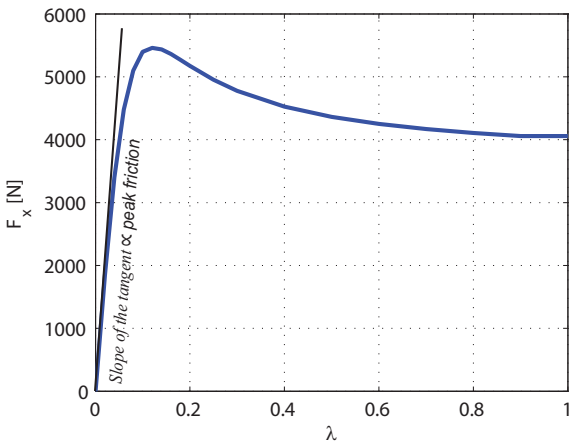

Figure 1.5: The relationship between the slope of longitudinal tyre slip λ versus longitudinal tyre force F_x characteristics and friction, as proposed in [23, 45, 46]. Here $\propto$ stands for *is proportional to.*

In [47], three nonlinear state observers using lateral vehicle dynamics are studied to estimate friction. It is an interesting line of research as it uses lateral vehicle dynamics. The proposed methods show good results on low friction surfaces. However, the estimates are inaccurate on high friction surfaces as the estimates oscillate considerably. In [48], a Burckhardt tyre model based adaptive lateral tyre force estimator is used to estimate the road-tyre friction. As the estimator is adaptive, it shows good results compared

to the nonadaptive case. However, the estimator might not be effective in the presence of longitudinal dynamics as longitudinal dynamics is neglected. In [49], a friction estimator is proposed using Recursive Least Square (RLS) and is based on a two degree of freedom (DOF) vehicle model using Dugoff tyre model. The estimator is studied in a simulator environment using an 8 DOF vehicle model. Although the simulations results are satisfying, the Dugoff tyre model coefficients are assumed to be known. Therefore, the method might not be robust to tyre wear, temperature and other factors that could influence the tyre model coefficients.

1.5.1. CONTRIBUTIONS OF THIS DISSERTATION

In the literature, mostly it is seen that road-tyre friction estimation is either based on pure longitudinal dynamics or pure lateral dynamics, whereas real life situations might involve both longitudinal and lateral dynamics. The longitudinal and lateral tyre dynamics depend on each other. Figure 1.6 shows the friction ellipse describing the maximum longitudinal and lateral tyre forces. Here F_x is the longitudinal tyre force and F_y is the lateral tyre force. The ellipse represents the maximum possible longitudinal tyre force and lateral tyre force for a given lateral tyre force and longitudinal tyre force respectively. F_x and F_y are highly nonlinear functions of slip ratio, side slip angle, camber and vertical load. It can be seen from the friction ellipse that as the magnitude of longitudinal tyre force increases, the maximum possible lateral tyre force decreases and vice versa. Because of this interdependency, considering either longitudinal or lateral dynamics and neglecting the other can affect the friction estimation accuracy.

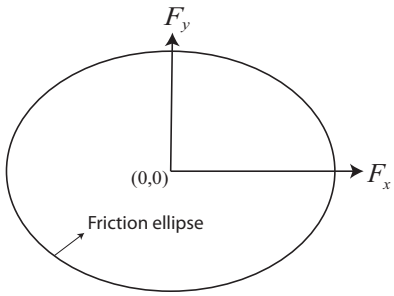

Figure 1.6: Friction ellipse describing the maximum longitudinal and lateral tyre forces.

Another issue is the estimator robustness to changes in the tyre model. Most of the works discussed above use a parameterized tyre model and this might affect the estimator robustnes as the tyre model parameters are prone to change depending on several factors such as temperature, tyre wear, vertical load, camber and toe angles. In this dissertation, a road-tyre friction estimator is proposed considering both longitudinal and lateral dynamics, and the estimator is robust to changes in the tyre parameters as tyre force measurements are used. Another benefit of the proposed method is that it can be applied to individual tyres.

Road-tyre friction estimators can be categorized depending on the level of required tyre dynamics excitation. In the first category, the estimator tries to extract some information about the tyre characteristics during low levels of tyre dynamics excitation and

this information is extrapolated to estimate the road-tyre friction [23, 45, 46]. The second category estimates the friction when the peak tyre force is crossed. The estimator proposed in this disseration belongs to the second category. The advantage of the first category is that it does not require the car to drive beyond the peak tyre force and the disadvantage is that the estimate is guessed based on the tyre model. The friction estimation is a form of extrapolation that heavily depends on the tyre model used. The advantage of the second type is a precise knowledge of the peak friction, but the car needs to drive beyond the peak. This means that when the tyres are far from their saturation limit, the friction estimate may not be current. Therefore, it is crucial to make sure that the lateral dynamics control is robust to this condition. For this reason, the proposed road-tyre friction estimation is designed and integrated with the yaw rate controller in Chapter 4 with the objective of improving the controller performance.

The proposed road-tyre friction estimator uses tyre force measurements. As road-tyre friction is reflected highly on tyre forces and there are not many studies present in the literature, this approach deserves attention. The proposed friction estimator is needed to implement and test the TUCC in Chapter 3 and to improve the performance of the yaw rate controller in Chapter 4. The following are the main contributions of the friction estimator.

- A road-tyre friction estimator is proposed considering combined slip situations. Therefore the estimator is effective during longitudinal, lateral and combined slip situations. As the estimator is applied to individual tyres, it is possible to estimate road-tyre friction of each of the tyres. It should be noted that the proposed estimator estimates the peak friction in whichever direction the tyre force is acting, ranging from purely longitudinal to purely lateral. This can introduce an error of up to 10 % as the longitudinal road-tyre peak friction is typically slightly higher than the lateral road-tyre peak friction.

- The proposed estimator uses tyre force measurements. Therefore the estimator is robust to changes in the tyre parameters due to tyre wear, temperature and other factors such as vertical load, cambre and toe. The estimator might be sensitive to the LSB sensor wear as it has moving parts. However, the sensor wear is expected to be a slower process than the tyre wear.

- The estimator is also studied during jump mu situation where the road friction changes.

- The estimator is studied in closed loop with the yaw rate controller proposed in [58] to see whether the proposed friction estimator improves vehicle safety.

- The estimator is also validated using test data from several maneuvers performed on a BMW test vehicle instrumented with LSB technology.

The proposed road-tyre friction estimator is discussed in detail in Chapter 5. In the next section, vehicle sideslip estimation is introduced.

1

1.6. VEHICLE SIDESLIP ESTIMATION

VEHICLE sideslip is one of the variables controlled by active safety systems like ESC [41, 67, 68]. It is defined as the angle between the vehicle longitudinal axis and the vehicle velocity vector. The vehicle sideslip affects the vehicle yaw moment sensitivity to steering angle [36, 69, 70]. This characteristic makes the vehicle yaw moment less sensitive to steering at higher vehicle sideslips. For certain range of vehicle sideslip and its time derivative, the vehicle motion is stable whereas outside this range i.e. outside this stability area, the vehicle yaw dynamics is unstable. In addition, as the steering angle increases, the stability area shrinks [71]. This is undesirable for an average driver. Therefore it is important to estimate and control the vehicle sideslip for better vehicle safety.

Vehicle sideslip is usually estimated as measuring it requires expensive sensors. In the literature, there are many methods to estimate vehicle sideslip. Based on the type of sensors used, the estimators can be classified into three main categories; using only inertial measurement sensors, using inertial measurement sensors and GPS, and using more exotic sensors. The estimator proposed in [72] uses GPS and it gives accurate results. GPS facilitates better vehicle velocity measurement compared to inertial measurement sensor based velocity estimation. However, it is not reliable in urban environment as buildings can degrade GPS accuracy.

In [73], based on the estimation method, four types of sideslip estimators; a linear observer, a nonlinear observer, a extended Kalman filter and a sliding-mode observer, are designed and compared. From this insightful comparison, the best among the four, the sliding-mode observer, is studied using a test vehicle in [74]. But for lateral accelerations higher than 0.6 g, the estimate is not accurate.

The sideslip estimators can also be categorized into physical model based and kinematic model based. The physical model based estimators are potentially more accurate and do not suffer from observability issues assuming the vehicle accelerations and yaw rate are measured. However, they require an accurate model of the dynamics. But some of the model parameters are difficult to measure, whereas some others are time varying and they should be identified online which makes the problem complex. There are several physical model based estimators in the literature. For example, in [75], an extended Kalman filter using adaptive linear tyre force model is studied and this method uses tyre cornering stiffnesses. However, the tyre saturation characteristic is not considered in this work. Also for the method to work, the lateral tyre forces should be more than 2000 N. The estimator proposed in [76] is interesting as it uses online tyre cornering stiffness estimation. However, it does not work on low friction surfaces such as ice and snow. In [77], a nonlinear observer is designed to estimate vehicle sideslip by solving Linear Matrix Inequalities (LMIs) and the estimator gives accurate results. However, solving LMIs real-time is computationally expensive.

Kinematic model based estimators have the advantage of being more efficient and simple. However, they suffer from sensor biases and observability problems while driving straight. For example, in [78], a kinematic model, describing vehicle longitudinal and lateral velocities, accelerations and yaw rate is used to design the vehicle sideslip estimator. This estimator is robust to the tyre nonlinearities which is not the case with physical model based estimators described in the previous paragraph. But the estimate is not accurate in the presence of roll and pitch dynamics. Moreover, because of the unobserv-

ability issue when the yaw rate is close to zero, the estimate drifts when the yaw rate is zero. Another issue that affects the kinematic model based estimators is the sensor bias. In [79], a real-time sensor bias compensation using disturbance observer is proposed to address this issue. However, the observability issue when the yaw rate is close to zero is not yet addressed. In [80], a sideslip estimator is proposed using both physical model based and kinematic model based estimators. At low frequencies of the lateral dynamics bandwidth, the physical model based estimator is used and at high frequencies of the lateral dynamics bandwidth, the kinematic model based estimator is used. This work shows accurate results but it might require roll and pitch angle estimators in the presence of roll and pitch dynamics.

1.6.1. CONTRIBUTIONS OF THIS DISSERTATION

In this dissertation, a vehicle sideslip estimator is proposed using a kinematic model. Therefore, it is robust to the tyre nonlinearities. It also has the benefit that the estimate is accurate even in the presence of roll and pitch dynamics. In addition, a heuristic method to overcome the unobservability issue is proposed. Therefore, the estimate does not drift when the yaw rate is close to zero.

The proposed kinematic model based estimator uses tyre force measurements and it is needed to implement and test the TUCC in Chapter 3. The main contributions of the proposed sideslip estimator are:

1. A force measurement based Kalman Filter is proposed to estimate vehicle sideslip. The proposed vehicle sideslip estimator uses a Kalman filter based on a kinematic model relating vehicle velocities and forces in the longitudinal and lateral directions, and yaw rate. The estimator performance is studied using Root Mean Square Error analysis.

2. A heuristic method to overcome the estimate drift, caused by the unobservability when the vehicle yaw rate is close to zero, is also proposed. It is further studied with the help of simulation as well as experimental results.

3. The estimator is studied for robustness against measurement noise and different road frictions.

4. The estimator is validated using test data from several maneuvers performed on a BMW test vehicle instrumented with LSB technology.

The proposed vehicle sideslip estimator is discussed in detail in Chapter 6.

1.7. LIST OF PUBLICATIONS

THIS section lists the publications produced from the research content of this dissertation.

1.7.1. JOURNAL PUBLICATIONS

1. A. K. Madhusudhanan, M. Corno and E. Holweg, “Sliding Mode Based Lateral Vehicle Dynamics Control Using Tyre Force Measurements," *Vehicle System Dynamics*,

vol. 53, no. 11, pp. 1599-1619, 2015.
doi: 10.1080/00423114.2015.1066018

2. A. K. Madhusudhanan, M. Corno, M. A. Arat and E. Holweg, “Load Sensing Bearing Based Road-Tyre Friction Estimation Considering Combined Tyre Slip," *Mechatronics*, 2016. Article in press.
doi: 10.1016/j.mechatronics.2016.03.011

3. A. K. Madhusudhanan, M. Corno and E. Holweg, “Vehicle Sideslip Estimator using Load Sensing Bearings," *Control Engineering Practice*, 2016. Accepted.
doi: 10.1016/j.conengprac.2016.05.008

1.7.2. CONFERENCE PUBLICATIONS

1. A. K. Madhusudhanan, M. Corno and E. Holweg, “Lateral Vehicle Dynamics Control Based On Tyre Utilization Coefficients and Tyre Force Measurements," *the* 52^{nd} *IEEE Conference on Decision and Control*, Florence, Italy, pp. 2816-2821, 10-13 December 2013.
doi: 10.1109/CDC.2013.6760310

2. A. K. Madhusudhanan, M. Corno and E. Holweg, “Vehicle Sideslip Estimation Using Tyre Force Measurements," *the 23rd Mediterranean Conference on Control & Automation*, Torremolinos, Spain, pp. 88-93, June 16-19, 2015.
doi: 10.1109/MED.2015.7158734

3. A. K. Madhusudhanan, M. Corno and E. Holweg, “Vehicle Yaw Rate Control Using Tyre Force Measurements," *the 14th European Control Conference*, Linz, Austria, pp. 2582-2587, July 15-17, 2015.
doi: 10.1109/ECC.2015.7330926

2

EXPERIMENTAL SETUP AND LOAD SENSING BEARING

2.1. EXPERIMENTAL SETUP

THIS chapter describes the experimental setup used in this dissertation. It is used to collect the experimental test data used in Chapter 5 and 6. A BMW 5 Series E60 model is used as the experimental setup. The test vehicle is equipped with Load Sensing Bearings (LSB) on all four tyres for tyre force measurements. The vehicle is also equipped with front road wheel steer angle sensors, longitudinal and lateral accelerometers, wheel angular velocity sensors and yaw rate sensor. The vehicle is also equipped with Corrsys sensors to calibrate and compare the LSB tyre force measurements. A dSpace real-time processor is used to process and collect the sensor measurements. The real-time processor also collects data from the vehicle Controller Area Network (CAN) bus.

(a) The instrumented test vehicle.

(b) The LSB technology from SKF.

Figure 2.1: The instrumented test vehicle and LSB technology from SKF.

2.2. LOAD SENSING BEARING

The Load Sensing Bearing (LSB) is a bearing technology from SKF [60] that estimates tyre forces in addition to its primary objective of acting as a bearing. Figure 2.1(b) shows a LSB unit from SKF. It uses six strain gauges to measure strains acting at six different locations inside the bearing. These strains are then processed and transformed into the longitudinal, lateral and vertical components of the road-tyre forces. The mapping between the six strain gauges and the tyre forces is approximated with Mutliple Linear Regression Analysis (MLRA) between the LSB strain gauges and the Corrsys sensor measurements [61]. In addition to the six LSB strain gauge measurements, the MLRA uses lateral acceleration and brake pressure measurements from the vehicle Controller Area Network (CAN) bus. This is because the LSB technology needs further development before it can be robust and can measure tyre forces without the additional variables. Research is being carried out in this direction at TU Delft.

The next section shows the comparison between the LSB and Corrsys measurements during different steering maneuvers[1].

2.2.1. STEERING MANEUVERS

The LSB and Corrsys measurements are compared during a J turn, Slalom and Lane Change maneuver. Figure 2.2-2.4 show the LSB longitudinal and lateral tyre force measurements of all four test vehicle tyres during the J turn, Slalom and Lane Change maneuver.

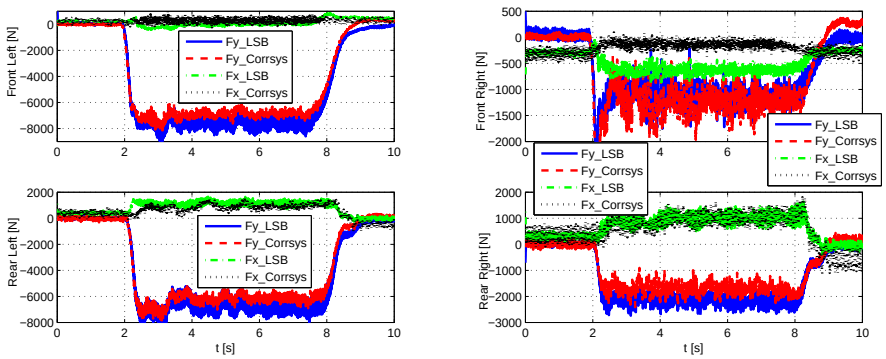

(a) Left tyre forces.

(b) Right tyre forces.

Figure 2.2: LSB and Corrsys tyre force measurements during a J turn maneuver at an initial speed of 100 km/h.

From the longitudinal and lateral tyre force measurements of all four tyres during the three maneuvers, it is seen that the LSB and Corrsys sensor measurements are overall strongly correlated both dynamically and statically. Table 2.1 shows the standard deviation (SD) between the LSB and Corrsys measurements from the three maneuvers. Here

[1]The test data has been collected by SKF and TNO in 2005.

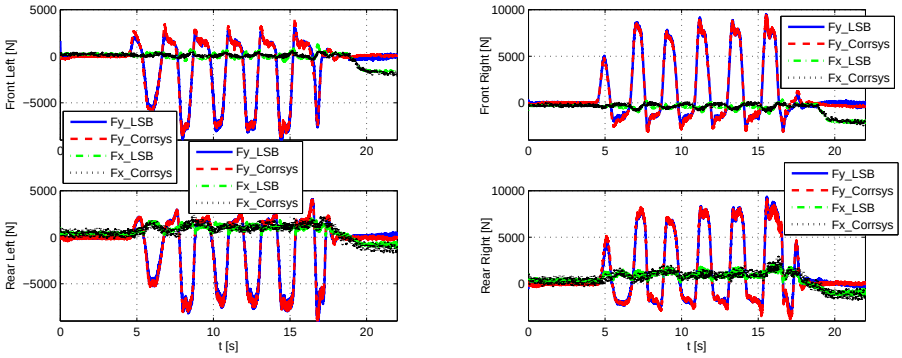

(a) Left tyre forces. (b) Right tyre forces.

Figure 2.3: LSB and Corrsys tyre force measurements during a Slalom maneuver at an initial speed of 60 km/h.

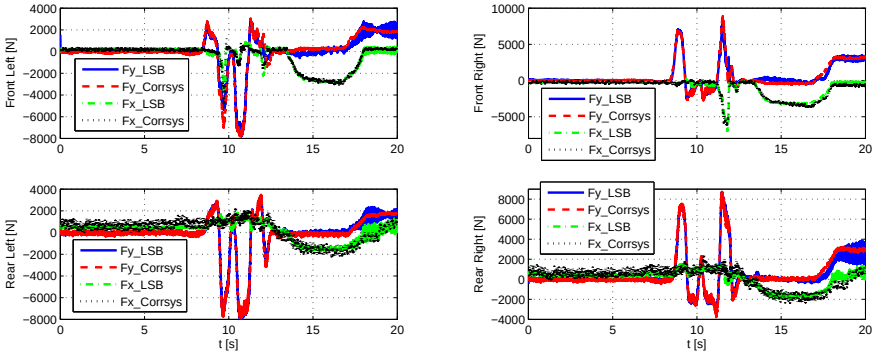

(a) Left tyre forces. (b) Right tyre forces.

Figure 2.4: LSB and Corrsys force measurements during a Lane Change maneuver at a speed of 104 km/h.

Table 2.1: Standard deviation (SD) between the LSB and Corrsys measurements during steering maneuvers

Maneuver	Force	SD	SD_{pmt}
J turn	F_x	708.48 N	8.0 %
J turn	F_y	904.41 N	9.5 %
Slalom	F_x	695.16 N	7.7 %
Slalom	F_y	678.81 N	7.1 %
Lane Change	F_x	795.57 N	9.0 %
Lane Change	F_y	752.83 N	7.9 %

SD is the standard deviation of an individual tyre force and SD_{pmt} is the standard deviation of an individual tyre force as a percentage of the maximum tyre force. Therefore from Table 2.1, it is seen that using the LSB, the tyre forces F_x and F_y has less than 10 % standard deviation as a percentage of their maximum.

2

2.2.2. BRAKING AND BRAKING WITH STEERING MANEUVERS

In this section, the LSB and Corrsys measurements during braking and braking with steering maneuvers are compared. Figure 2.5-2.6 show the LSB longitudinal, lateral and vertical tyre force measurements of the front left tyre. From the longitudinal, lateral

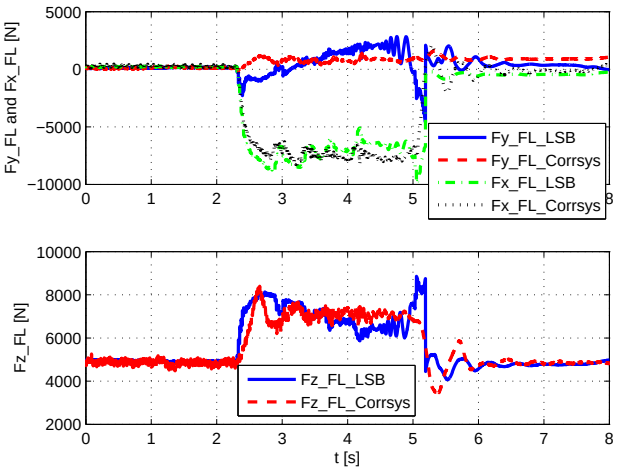

Figure 2.5: LSB and Corrsys tyre force measurements during a braking maneuver from 100 km/h without steer.

Table 2.2: Standard deviation (SD) between the LSB and Corrsys measurements during the braking maneuvers

Maneuver	Force	SD	SD_{pmt}
Braking	F_x	892.38 N	10.0 %
Braking	F_y	878.14 N	9.2 %
Braking	F_z	558.37 N	6.7 %
Braking with steering	F_x	697.25 N	7.8 %
Braking with steering	F_y	663.94 N	7.0 %
Braking with steering	F_z	532.40 N	6.3 %

and vertical tyre force measurements during the maneuvers, it is seen that the LSB and Corrsys sensor measurements are correlated both dynamically and statically. However, the correlation between the LSB and Corrsys sensor measurements is lower compared to the steering maneuvers in Section 2.2.1. Table 2.2 shows the standard deviation (SD) between the LSB and Corrsys measurements from the three maneuvers. From Table 2.2,

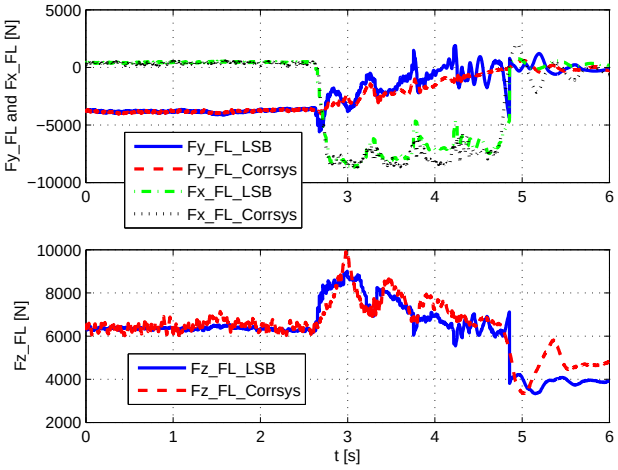

Figure 2.6: LSB and Corrsys tyre force measurements during a braking maneuver with a steering angle of 40 deg. The vehicle starts braking from 72 km/h.

it is seen that using the LSB, the tyre forces F_x, F_y and F_z has less than 10.1 % standard deviation as a percentage of their maximum.

2.3. CONCLUSIONS

The LSB technology is introduced in this chapter. It is seen that the LSB and Corrsys tyre force measurements are correlated both dynamically and statistically during steering, braking and braking with steering maneuvers. The tyre forces have less than 10.1 % standard deviation as a percentage of their maximum.

In addition to the LSB strain gauge measurements, the tyre force calculations use lateral acceleration and brake pressure measurements from the vehicle CAN bus. This approach may not be robust for all driving situations. The LSB technology needs further development before it can be robust and can measure tyre forces without the additional variables. Research is being carried out in this direction at TU Delft. Given the primary objective of this dissertation, *i.e.* to study the benefits of tyre force measurement on active safety systems for lateral vehicle dynamics, the measurements shown in this chapter are used in Chapter 5 and Chapter 6. In the next chapter, a Lateral Vehicle Dynamics Control scheme using tyre force measurements is studied.

3

TYRE UTILIZATION COEFFICIENT CONTROL

3.1. INTRODUCTION

A LATERAL vehicle dynamics control based on tyre force measurements is proposed in this chapter. Most of the lateral vehicle dynamics control schemes are based on yaw rate whereas tyre forces are the most important variables in vehicle dynamics as tyres are the only contact points between the vehicle and road. In the proposed controller, active front steering is employed to uniformly distribute the required lateral force among the front left and right tires. The force distribution is quantified through the Tyre Utilization Coefficients (TUC). TUC is an indication of how much the tyre is engaged with respect to the maximum force it can exert. It is denoted by a number in the range zero to one.

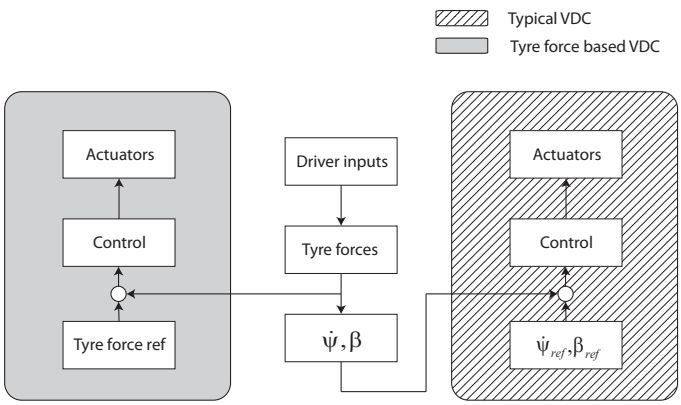

Figure 3.1: Tyre force based vs typical VDC.

Parts of this chapter have been published in Vehicle System Dynamics [55] and proceedings of the 52^{nd} IEEE Conference on Decision and Control [17].

The basic principle is to equalize the left and right TUC of the front axle using active independent front steering. Therefore, the controller is called Tyre Utilization Coefficient Control (TUCC). By doing so, saturation during cornering can be avoided or delayed, thereby improving stability. Although steer-by-wire is not yet an off-the-shelf technology, active steering is being researched actively. This warrants the study and design of VDC systems based on active steering. It should be noted that the rear axle TUCs are not controlled as it is observed that during cornering, the difference between the rear left TUC and rear right TUC is very small. The following are the main features of the proposed TUCC.

- A Tyre Utilization Coefficient Controller is designed with the objective of equalizing the front left and front right TUCs using active independent front steering.
- The nonlinearities and uncertainties of the vehicle model are considered. In order to address them, an output tracking Sliding Mode Control (SMC) is designed and validated. The final SMC is gain scheduled with respect to vehicle speed.
- An active steering system model is considered to incorporate steering actuator dynamics.
- The effect of the proposed controller on vehicle lateral acceleration is studied. As shown in Figure 3.2, on a typical dry road, lateral tyre force F_y has a peak value corresponding to a certain tyre side slip angle α. This implies that, if a driver applies more steering assuming he will get more lateral acceleration and stability is not lost in the process, he might in fact be settling for a lower lateral acceleration. With the proposed controller, a vehicle can maintain the maximum possible lateral tyre forces and therefore maintain the maximum possible lateral acceleration for higher steering angles.

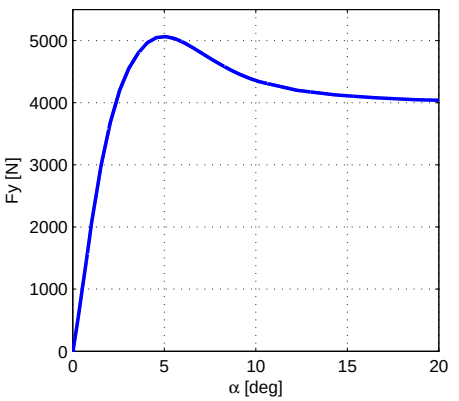

Figure 3.2: Typical lateral tyre force characteristics on a dry road.

- The TUCC is studied for its robustness against vehicle velocity, force measurement noise and road-tyre friction.

Table 3.1: CarSim vehicle model parameters

Parameter	Value
Mass	1231 kg
Yaw inertia	2031.4 kgm^2
Distance from Center of Gravity (CoG) to front axle	1.016 m
Distance from CoG to rear axle	1.562 m
Distance between left and right tyres	1.539 m

This chapter is structured as follows. Section 3.2 shows the vehicle model used to design the controller. In Section 3.3, the controller design is explained in detail. The controller is simulated in closed loop and the results are discussed in Section 3.4. Section 3.5 concludes the findings and discusses possible future work.

3.2. LATERAL VEHICLE DYNAMICS MODELING

A FOUR-WHEELED vehicle equipped with independent front steering and tyre force sensors is assumed. The longitudinal, lateral and vertical tyre force measurements of the front tyres are assumed to be available. In the following, two models of a four-wheeled vehicle are employed. The vehicle model used for simulation is a multi-body model with 15 mechanical degrees of freedom (DOF) from CarSim simulation package [18]. The CarSim model uses a nonlinear tyre model with dependency on slip, load, and camber. A standard hatchback vehicle is simulated (see the vehicle configuration *Ind_Ind: B-Class, Hatchback: No ABS* in CarSim for more details about the vehicle model). The considered vehicle has the parameters shown in Table 3.1.

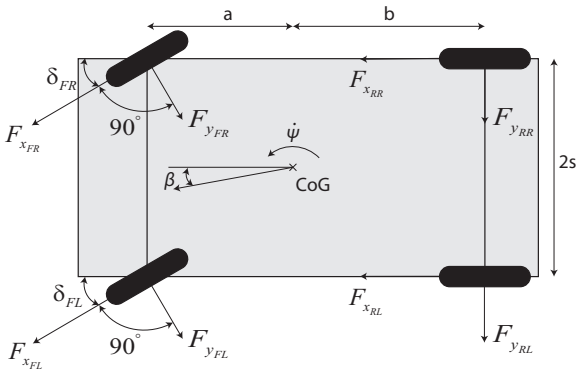

Figure 3.3: Simplified vehicle model used for the TUCC design.

For the controller design, a control oriented double track model as shown in Figure 3.3 with states yaw rate $\dot{\psi}$ and vehicle sideslip β is used. The model outputs are front left lateral tyre force $F_{y_{FL}}$ and front right lateral tyre force $F_{y_{FR}}$. The control inputs are front left road steering angle δ_{FL} and front right road steering angle δ_{FR}. The simplified state equations are shown in (3.1) and (3.2).

$$\begin{aligned}\dot{\beta} = \frac{1}{Mv}(&F_{y_{FL}} + F_{x_{FL}}\delta_{FL} + F_{y_{FR}} + F_{x_{FR}}\delta_{FR} \\ &+ F_{y_{RL}} + F_{y_{RR}}) - \frac{\beta}{Mv}(F_{x_{FL}} - F_{y_{FL}}\delta_{FL} + F_{x_{FR}} \\ &- F_{y_{FR}}\delta_{FR} + F_{x_{RL}} + F_{x_{RR}} - c_{aer}A_L\frac{\rho}{2}v^2) - \dot{\psi},\end{aligned} \tag{3.1}$$

$$\begin{aligned}J_z\ddot{\psi} = &(F_{y_{FR}} + F_{x_{FR}}\delta_{FR} + F_{y_{FL}} + F_{x_{FL}}\delta_{FL})a \\ &- (F_{y_{RL}} + F_{y_{RR}})b + (F_{x_{RR}} - F_{x_{RL}})s \\ &+ (F_{x_{FR}} - F_{y_{FR}}\delta_{FR})s - (F_{x_{FL}} - F_{y_{FL}}\delta_{FL})s.\end{aligned} \tag{3.2}$$

Here M is the vehicle mass, v is the velocity, $F_{y_{ij}}$ is the lateral tyre force of ij tyre, $F_{x_{ij}}$ is the longitudinal tyre force of ij tyre, δ_{ij} is the road steering angle, c_{aer} is the coefficient of aerodynamic drag, A_L is the front vehicle area, ρ is the air density and J_z is the moment of inertia around yaw axis. a, b and s are vehicle dimensions as shown in Figure 3.3. It is assumed that the steering angles are small so that $\cos\delta_{ij} \approx 1$ and $\sin\delta_{ij} \approx \delta_{ij}$. The output equations are shown in (3.3) and (3.4).

$$F_{y_{FL}} = C_{y_{FL}}\left(\delta_{FL} - \left(\beta + \frac{\dot{\psi}a}{v}\right)\right), \tag{3.3}$$

$$F_{y_{FR}} = C_{y_{FR}}\left(\delta_{FR} - \left(\beta + \frac{\dot{\psi}a}{v}\right)\right). \tag{3.4}$$

Here $C_{y_{ij}}$ is the cornering stiffness of the ij tyre. They are calculated from the linear region of the CarSim tyre model. Further the state and output equations in (3.1) to (3.4) are linearized with $v = 80$ km/h and no steering wheel angle as shown in (3.5) and (3.6). The model parameters for linearization are obtained from the CarSim vehicle model and a CarSim simulation performed at $v = 80$ km/h while driving straight. The linearization vehicle speed is chosen as 80 km/h as the controller is first studied with $v = 80$ km/h and it is the recommended Electronic Stability Control test speed [28].

The linearized model inevitably introduces some approximations and uncertainties. In order to account for them, it is assumed that the model uncertainties and nonlinearities lie in the image of input matrix B_i and feedthrough matrix D_i as shown in (3.5) and (3.6). This assumption, which is required for the SMC design, is called matching condition [19].

$$\dot{\tilde{x}} = A_i\tilde{x} + B_iu + B_ie_x(t), \tag{3.5}$$

$$y = C_i\tilde{x} + D_iu + D_ie_y(t). \tag{3.6}$$

Here $\tilde{x} = \{\beta, \dot{\psi}\}$, $u = \{\delta_{FL}, \delta_{FR}\}$ and $y = \{F_{y_{FL}}, F_{y_{FR}}\}$. A_i, B_i, C_i and D_i are linearized system matrices. $e_x(t)$ and $e_y(t)$ are vectors that lump all the model uncertainties and nonlinearities in the state and output equations respectively.

Since the objective is lateral tyre forces tracking, the system state vector is augmented with the integral of the lateral force tracking errors,

$$x_{a_{FL}} = \int \left(F_{y_{FL}}^{ref} - F_{y_{FL}}\right) dt, \tag{3.7}$$

$$x_{a_{FR}} = \int \left(F_{y_{FR}}^{ref} - F_{y_{FR}}\right) dt, \tag{3.8}$$

$$\dot{x} = \begin{bmatrix} A_i & 0 \\ -C_i & 0 \end{bmatrix} x + \begin{bmatrix} B_i \\ -D_i \end{bmatrix} u + \begin{bmatrix} B_i & 0 \\ 0 & -D_i \end{bmatrix} e + \begin{bmatrix} 0 \\ I \end{bmatrix} r. \tag{3.9}$$

Here $x = \{\beta, \dot{\psi}, x_{a_{FL}}, x_{a_{FR}}\}$, $e = \{e_x(t), e_y(t)\}$ and r is the reference lateral tyre force vector $\{F_{y_{FL}}^{ref}, F_{y_{FR}}^{ref}\}$. Using $A = \begin{bmatrix} A_i & 0 \\ -C_i & 0 \end{bmatrix}$, $B_1 = \begin{bmatrix} B_i \\ -D_i \end{bmatrix}$, $B_e = \begin{bmatrix} B_i & 0 \\ 0 & -D_i \end{bmatrix}$ and $B_2 = \begin{bmatrix} 0 \\ I \end{bmatrix}$ gives,

$$\dot{x} = Ax + B_1 u + B_e e + B_2 r. \tag{3.10}$$

3.2.1. MODEL VALIDATION

In this section, the Linear Time-Invariant (LTI) model defined by the State Space matrices $\{A_i, B_i, C_i, D_i\}$ in (3.5-3.6) is compared with the 15 DoF multi-body model from CarSim simulation package. A band limited white noise with sampling time 0.01 s is applied to the front left and front right steering. Sampling time 0.01 s is chosen as 50 Hz is assumed to be well above typical lateral vehicle dynamics bandwidth.

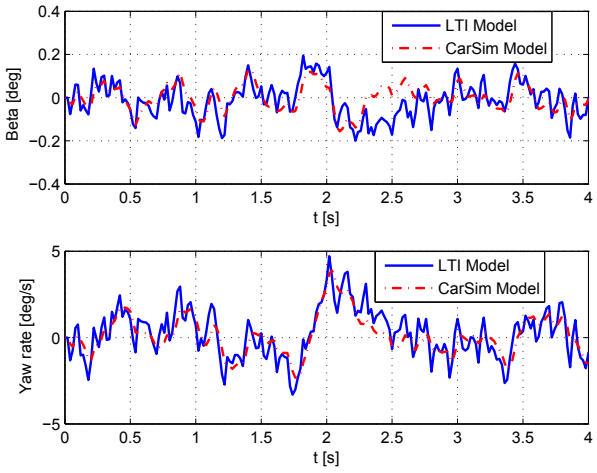

Figure 3.4: States from the model validation simulation.

The vehicle states $\{\beta, \dot{\psi}\}$ from the simulation are shown in Figure 3.4. It can be observed from the plots that the LTI model is able to capture the dynamics of CarSim multi-

body model. The error between the CarSim and LTI model is due to the model approximations and uncertainties represented by the $B_i e_x$ term in (3.5).

3.2.2. STEERING ACTUATOR CONTROL

The vehicle is assumed to have an active steering system for the front wheels [20, 21]. The overall Steering Actuator Control (SAC), accounting for the dynamics of the actuator and bandwidth of the steering control system, is assumed to have a closed loop bandwidth of 10 Hz [21, 22]. Figure 3.5 shows the complementary sensitivity function of the SAC.

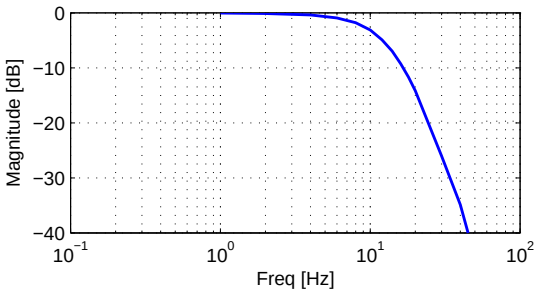

Figure 3.5: Complimentary sensitivity function of the active steering system.

Two of such SACs, SAC Left (SACL) and SAC Right (SACR), are used, one for the front left wheel and the other for the front right wheel. The SACs are considered to be a part of the vehicle as the lateral dynamics controller applies control input to the SACs. In the next section, the lateral dynamics controller is discussed.

3.3. LATERAL DYNAMICS CONTROL

In this section, the lateral dynamics control structure and its design is explained. The control structure is shown in Figure 3.6.

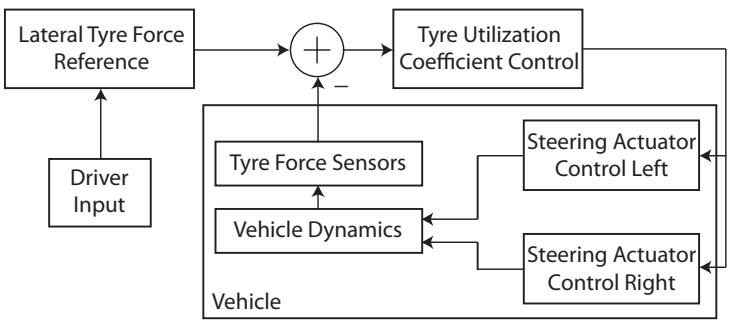

Figure 3.6: Control scheme of the proposed TUCC.

The controller, named Tyre Utilization Coefficient Control (TUCC), generates the desired road steering angles for the front left and front right tyres and are applied to the

Steering Actuator Control Left and Right (SACL and SACR). TUCC is a nonlinear control based on Sliding Mode and is designed considering the vehicle model uncertainties and nonlinearities.

3.3.1. TYRE UTILIZATION COEFFICIENT CONTROL

The TUCC is designed with the objective of keeping the vehicle stable in the lateral direction; this is achieved by forcing the lateral tyre forces to track a computed reference value. The reference lateral tyre forces are generated such that both the front left and front right tyres have equal TUC.

TYRE UTILIZATION COEFFICIENT

TUC k is defined in (3.11) and is shown graphically using the friction ellipse in Figure 3.7. It is an indication of how much the tyre is engaged with respect to the maximum force it can exert.

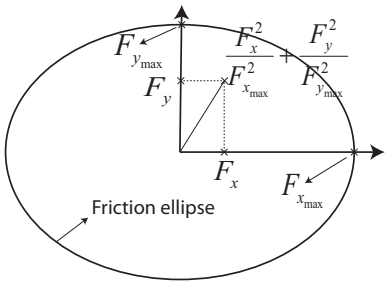

Figure 3.7: Definition of tyre utilization coefficient k using friction ellipse.

$$k = \frac{F_x^2}{F_{x_{max}}^2} + \frac{F_y^2}{F_{y_{max}}^2}, \text{ where } 0 <= k <= 1. \tag{3.11}$$

Here F_x is the longitudinal tyre force, F_y is the lateral tyre force, $F_{x_{max}}$ is the maximum possible longitudinal tyre force and $F_{y_{max}}$ is the maximum possible lateral tyre force. F_x and F_y are highly nonlinear functions of slip ratio, side slip angle, camber and vertical load. $F_{x_{max}}$ and $F_{y_{max}}$ depend on many factors; among them are peak road-tyre friction and vertical forces. The vertical force measurement is available from the force sensors. There are several works published on peak road-tyre friction estimation. As this chapter focuses on lateral dynamics control, the peak road-tyre friction is assumed to be available using one of the estimation methods from literature [23–26] or the estimator from Chapter 5 of this dissertation.

TUCs are zero when the vehicle is still on a horizontal surface or when the tyres are freely rolling. They are one when the tyres are exerting the maximum possible force in longitudinal, lateral or an intermediate direction. In different driving conditions, the vehicle tyres might employ different TUCs. For instance, during a steady state cornering, because of lateral acceleration, if the vehicle Center of Gravity (CoG) is above the roll

center, lateral load transfer will load the outer tyres more than the inner tyres. This can cause unequal TUCs between the outer and inner tyres because of the nonlinear characteristics of tyre dynamics, steering system, and suspension camber.

To understand this better, the behavior of the TUCs is studied for various lateral accelerations during steady state cornering. Figure 3.8 shows the TUCs of the front left tyre k_{FL} and the front right tyre k_{FR} for various lateral accelerations a_y. The tyre side slip angles of the front left tyre α_{FL} and the front right tyre α_{FR} are also shown. In this set of simulations, the left tyre is the inner tyre and the radius of curvature is 100 m.

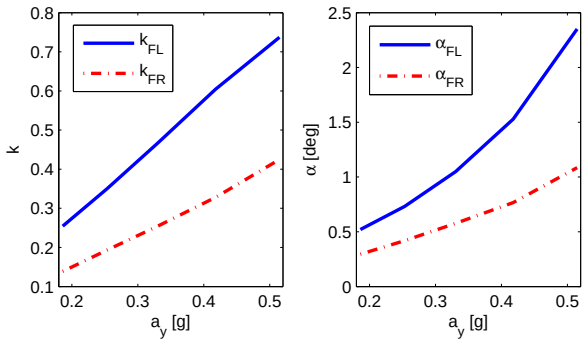

Figure 3.8: TUC study during steady state cornering maneuvers.

From Figure 3.8, it is observed that the inner TUC, k_{FL}, is always higher than the outer TUC, k_{FR}. This is caused by the Ackermann steering geometry and compliances of the steering and suspension systems. As a consequence, the inner wheel reaches higher tyre side slip (see Figure 3.8). This means that the natural lateral tyre forces do not yield equal TUCs. Hence all tyres would not have equal reserve, and this might lead to saturation of TUC of one of the tyres when another tyre is under employed. This might cause an average skilled driver to loose control. For example, if the driver applies brake when the inner tyre is saturated and the outer tyre is not, the inner tyre would reach the unstable region of tyre dynamics, and this might make the vehicle unstable. Whereas with equal TUCs, both tyres can stay in the stable region of tyre dynamics until a higher plannar acceleration value. If the vehicle can be controlled so that equal right and left TUCs are obtained, the saturation of the inner TUC can be avoided or delayed, thereby assisting the driver in keeping the vehicle stable. The rear TUCs k_{RL} and k_{RR} also have the same behavior; however the difference is much less than the front tyres.

Another interesting driving situation to study TUCs is a constant speed cornering where an average skilled driver applies steering higher than a certain threshold. On a typical dry road, the lateral tyre force has a peak value corresponding to a certain tyre side slip angle. Its effect is shown in Figure 3.9 where the steering wheel angle is increased till 300 deg at a constant vehicle speed of 80 km/h. It can be observed that the lateral acceleration reaches its peak around 135 deg steering wheel angle and then the lateral acceleration decreases. This means that the driver is settling for an undesired lower lateral acceleration value. In terms of TUCs, it means that, instead of the front tyre TUCs being one, they might be lower than one as shown in the top plot of Figure 3.9.

Thereby the lateral acceleration reduces as the steering wheel value is increased from 135 deg, which is undesirable.

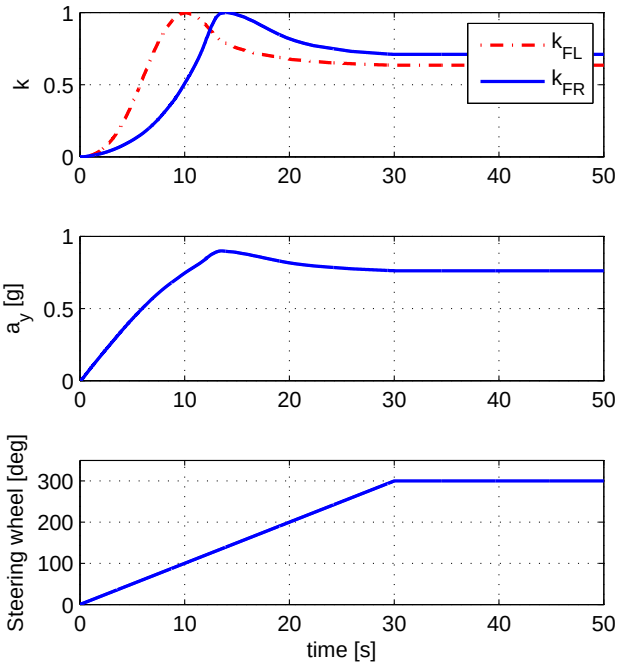

Figure 3.9: Effect of driver steering wheel on lateral acceleration on a dry road.

With the proposed controller, a vehicle can maintain the maximum possible lateral tyre forces and therefore maintain the maximum possible lateral acceleration for higher steering angles.

UNFEASIBILITY OF EQUAL TYRE UTILIZATION COEFFICIENT OF ALL FOUR TYRES

If all four tyres were to have equal TUC, there should be equal distribution among the front and rear axles. This implies the front axle utilization coefficient $k_F \approx \frac{F_{y_F}}{F_{z_F}}$ should be equal to rear axle utilization coefficient $k_R \approx \frac{F_{y_R}}{F_{z_R}}$. Here F_{y_F} is the sum of lateral tyre forces of the front axle tyres, F_{z_F} is the sum of normal tyre forces of the front axle tyres, F_{y_R} is the sum of lateral tyre forces of the rear axle tyres and F_{z_R} is the sum of normal tyre forces of the rear axle tyres. Here the TUC is approximated as $k \approx \frac{F_y}{F_z}$ assuming $F_x << F_y$ and $F_{y_{max}} = F_z$. The vertical tyre force F_z is assumed to be equal to the vertical force acting on the suspension.

Assuming there is no longitudinal load transfer, the vehicle weight is distributed among the front and rear axle based on the vehicle dimensions a and b as shown in (3.12) and (3.13).

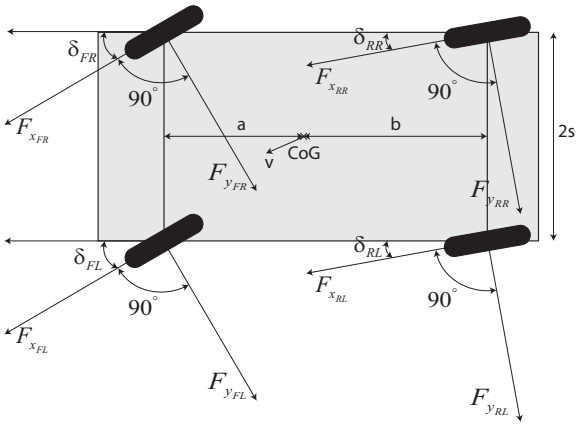

Figure 3.10: Two-track vehicle model

$$F_{z_F} = \frac{b}{a+b}Mg \tag{3.12}$$

$$F_{z_R} = \frac{a}{a+b}Mg \tag{3.13}$$

Here g is the gravity. It is assumed that $a \neq b$ which is the case for most commercial cars. For a steady state cornering, planar moment equilibrium around the vehicle CoG is necessary. Considering the two-track vehicle model in Figure 3.10, planar moment equilibrium around the vehicle CoG can be written as follows,

$$\begin{aligned}
&(F_{y_{FR}}\cos(\delta_{FR}) + F_{x_{FR}}\sin(\delta_{FR}))a - (F_{y_{FR}}\sin(\delta_{FR}) - F_{x_{FR}}\cos(\delta_{FR}))s \\
&+ (F_{y_{FL}}\cos(\delta_{FL}) + F_{x_{FL}}\sin(\delta_{FL}))a + (F_{y_{FL}}\sin(\delta_{FL}) - F_{x_{FL}}\cos(\delta_{FL}))s \\
&= (F_{y_{RR}}\cos(\delta_{RR}) + F_{x_{RR}}\sin(\delta_{RR}))b + (F_{y_{RR}}\sin(\delta_{RR}) - F_{x_{RR}}\cos(\delta_{RR}))s \\
&+ (F_{y_{RL}}\cos(\delta_{RL}) + F_{x_{RL}}\sin(\delta_{RL}))b - (F_{y_{RL}}\sin(\delta_{RL}) - F_{x_{RL}}\cos(\delta_{RL}))s.
\end{aligned} \tag{3.14}$$

Assuming steering angles are close to zero for the chosen steady state cornering, $\sin(\delta_{ij})$ and $\cos(\delta_{ij})$ can be approximated as δ_{ij} and 1. This gives,

$$\begin{aligned}
&(F_{y_{FR}} + F_{x_{FR}}\delta_{FR})a - (F_{y_{FR}}\delta_{FR} - F_{x_{FR}})s + (F_{y_{FL}} + F_{x_{FL}}\delta_{FL})a + (F_{y_{FL}}\delta_{FL} - F_{x_{FL}})s \\
&= (F_{y_{RR}} + F_{x_{RR}}\delta_{RR})b + (F_{y_{RR}}\delta_{RR} - F_{x_{RR}})s + (F_{y_{RL}} + F_{x_{RL}}\delta_{RL})b - (F_{y_{RL}}\delta_{RL} - F_{x_{RL}})s.
\end{aligned} \tag{3.15}$$

Dividing both sides by F_{z_F} and using $F_{z_F} = F_{z_R}\frac{b}{a}$ from (3.12) and (3.13) gives,

$$\frac{F_{y_F}}{F_{z_F}} = \frac{F_{y_R}}{F_{z_R}} + k_\Delta, \text{ or} \tag{3.16}$$

$$k_F = k_R + k_\Delta, \text{ where} \tag{3.17}$$

$$k_\Delta = [(F_{x_{RR}}\delta_{RR} + F_{x_{RL}}\delta_{RL})b + (F_{y_{RR}}\delta_{RR} - F_{y_{RL}}\delta_{RL})s - (F_{x_{RR}} - F_{x_{RL}})s \\ - (F_{x_{FR}}\delta_{FR} + F_{x_{FL}}\delta_{FL})a + (F_{y_{FR}}\delta_{FR} - F_{y_{FL}}\delta_{FL})s - (F_{x_{FR}} - F_{x_{FL}})s]\frac{1}{F_{z_F}a}. \tag{3.18}$$

Since k_Δ is a non-zero quantity, it means that employing equal TUC among front and rear axle is not feasible if planar moment equilibrium is to be maintained. Therefore employing equal TUC from all four tyres is not feasible.

However, it is observed that the left and right tyres of the rear axle have almost equal TUCs during cornering simulations. As stated early, left and right tyres of the front axle can have equal TUCs, although they differ from the rear axle TUCs, and it can avoid or delay saturation of the inner TUC during a cornering event, thereby assisting the driver in keeping the vehicle stable. In the next section, this is further studied with the help of a closed loop controller.

TUCC DESIGN

The TUCC structure is shown in Figure 3.6. The schematic has two main components: a controller tuned to track a reference and a lateral tyre force reference generator. The *Lateral Tyre Force Reference* generator computes the reference according to two objectives. The first objective is to guarantee that the front right and left TUCs are equal; the second objective is to force a desired dynamics on the vehicle. As a result of the desired dynamics defined by the second objective, the vehicle can maintain the maximum possible lateral acceleration for higher steering angles. The first objective is given in (3.19).

$$k_{FL} = k_{FR} = k_F^{req}, \tag{3.19}$$

$$k_{ij} = \frac{F_{x_{ij}}^2}{F_{x_{ijmax}}^2} + \frac{F_{y_{ij}}^2}{F_{y_{ijmax}}^2}. \tag{3.20}$$

Here k_F^{req} is the required TUC of the front axle tyres. Further the lateral tyre force reference values considering a desired vehicle dynamics are calculated using the reference generator in Figure 3.6.

The reference generator receives the driver's steering input δ, vehicle velocity v, and tyre force measurements $\{F_{x_{ij}}, F_{y_{ij}}, F_{z_{ij}}\}$ as inputs. The desired dynamics is expressed through the understeering gradient according to:

$$R_{req} = \frac{1}{\delta}\left(a + b + \frac{v^2\eta}{g}\right), \tag{3.21}$$

$$a_y^{req} = \frac{v^2}{R_{req}} \text{with limits } \{-\mu_y g, \mu_y g\}, \tag{3.22}$$

$$k_F^{req} = \frac{|a_y^{req}|}{\mu_y g} + \frac{F_{x_{Fq}}^2}{F_{x_{Fqmax}}^2} \text{with limits } \{0, 1\}. \tag{3.23}$$

Here R_{req} is the Radius of Curvature (RoC) of the curve the vehicle is trying to negotiate, η is the desired understeer coefficient, and a_y^{req} is the lateral acceleration required

in order to negotiate the curve with RoC R_{req}. The value of η is chosen as 0.0171 rad/g, the understeer coefficient of the linearized CarSim vehicle model. a_y^{req} has saturation limits based on the considered road friction μ_y and gravity g. $\frac{F_{x_{Fq}}^2}{F_{x_{Fqmax}}^2}$ in (3.23) is defined below.

$$\frac{F_{x_{Fq}}^2}{F_{x_{Fqmax}}^2} = \begin{cases} \frac{F_{x_{FL}}^2}{F_{x_{FLmax}}^2}, & \text{if } \frac{F_{x_{FL}}^2}{F_{x_{FLmax}}^2} \geq \frac{F_{x_{FR}}^2}{F_{x_{FRmax}}^2}, \\ \frac{F_{x_{FR}}^2}{F_{x_{FRmax}}^2}, & \text{otherwise.} \end{cases} \tag{3.24}$$

The second controller objective is given in (3.23) and as a result of this objective, when the driver applies higher steering angle such that $\left|\frac{v^2}{R_{req}}\right| > \mu_y g$, k_F^{req} will be 1. This would cause the vehicle to maintain the maximum possible lateral acceleration which depends on the longitudinal tyre forces. Finally the lateral tyre force reference values are calculated depending on the longitudinal tyre forces[1],

$$F_{y_{FL}}^{ref} = \sqrt{\left(k_F^{req} - \frac{F_{x_{FL}}^2}{F_{x_{FLmax}}^2}\right)} F_{y_{FLmax}} \text{sign}(F_{y_{FL}}), \tag{3.25}$$

$$F_{y_{FR}}^{ref} = \sqrt{\left(k_F^{req} - \frac{F_{x_{FR}}^2}{F_{x_{FRmax}}^2}\right)} F_{y_{FRmax}} \text{sign}(F_{y_{FR}}). \tag{3.26}$$

The maximum possible tyre forces $F_{x_{ijmax}}$ and $F_{y_{ijmax}}$ are calculated based on the vertical tyre force $F_{z_{ij}}$ and the peak road-tyre friction. Here sign$(F_{y_{ij}})$ is 1 if $F_{y_{ij}} >= 0$ and -1 otherwise. $F_{y_{FL}}^{ref}$ and $F_{y_{FR}}^{ref}$ are calculated in (3.25) and (3.26) such that the TUCC objectives $k_{FL} = k_{FR} = k_F^{req}$ in (3.19) and $k_F^{req} = \frac{\left|a_y^{req}\right|}{\mu_y g} + \frac{F_{x_{Fq}}^2}{F_{x_{Fqmax}}^2}$ with limits $\{0,1\}$ in (3.23) are met.

Based on the lateral force references in (3.25) and (3.26), and the vehicle model in (3.10), the TUCC is designed. Considering sensor noise, vehicle model nonlinearities and vehicle model uncertainties, Sliding Mode Control (SMC) is chosen in virtue of its robustness characteristic (see [19, 27] for more details on SMC).

Controller: The SMC is defined in (3.27)-(3.29). As seen in (3.27), the control has two parts, a continuous and a discontinuous one. u_{eq} is the continuous part and is the equivalent control assuming the lumped vector e in (3.10) to be zero. u_N is the discontinuous part that compensates the uncertainties and nonlinearities.

[1]The extreme case is represented by a vehicle that is already accelerating at the limit of the longitudinal force ($F_x = F_{x_{max}}$). If a steering input that translates into a desired k_F^{req}, according to (3.23), is given in this condition, the lateral force reference generation in (3.25)-(3.26) would yield 0 and the vehicle would not steer. This could be arguable as the vehicle would not be able to steer and avoid an obstacle; but note that this is a limitation of the actuation (we are assuming to only have automatic control of steering) and not of the control algorithm. If braking actuator is also available, an ABS strategy considering lateral tyre force, as proposed in [16] may be employed.

$$u = u_{eq} + u_N \text{ where,} \tag{3.27}$$
$$u_{eq} = -(C_s B_1)^{-1} C_s (Ax + B_2 r), \tag{3.28}$$
$$u_N = -\frac{B_1^T C_s^T C_s x}{\|B_1^T C_s^T C_s x\|_2}\gamma. \tag{3.29}$$

Here $\gamma = \rho + \alpha$ where $\rho > \|(B_i^T B_i + D_i^T D_i)^{-1}\begin{bmatrix} B_i^T B_i & D_i^T D_i \end{bmatrix} e\|_2$ (B_i and D_i are the input and feedthrough matrices from (3.5) and (3.6)) and α is a positive number.

Proposition: Given the controller (3.27)-(3.29) and the model defined in (3.10), the sliding surface in (3.31) is attractive for the closed loop system.

$$S = \begin{bmatrix} 0 & 0 & 1 & 0 \\ 0 & 0 & 0 & 1 \end{bmatrix} x = 0 \tag{3.30}$$
$$= C_s x = 0. \tag{3.31}$$

Physical interpretation of the above equation is that when the vehicle states x satisfy (3.31), the lateral tyre forces $\{F_{y_{FL}}, F_{y_{FR}}\}$ track their reference $\{F_{y_{FL}}^{ref}, F_{y_{FR}}^{ref}\}$.

Sketch of Proof: The following proof is an adaptation of the results found in [19] to the specific features of the system at hand. To design the controller and study the closed loop system, the following candidate Lyapunov function V is considered,

$$V = \frac{1}{2} S^T S. \tag{3.32}$$

If the sliding surface is attractive for the system, then the front lateral forces will track their reference values. For the sliding surface to be attractive,

$$\dot{S} = 0 \text{ i.e.,} \tag{3.33}$$
$$C_s \dot{x} = 0. \tag{3.34}$$

u_{eq} and u_N are generated separately. First, the equivalent control u_{eq} is computed assuming $e = 0$ and $u = u_{eq}$. Then substituting $\dot{x}$ from (3.10) in (3.34) gives,

$$C_s \left(Ax + B_1 u_{eq} + B_2 r\right) = 0. \tag{3.35}$$

After manipulation:

$$u_{eq} = -(C_s B_1)^{-1} C_s (Ax + B_2 r). \tag{3.36}$$

$C_s B_1 = -D_i$ and $-D_i$ is invertible as D_i is diagonal with tyre cornering stiffness as diagonal elements. Therefore u_{eq} can be calculated with (3.36).

Now $\dot{V}$ can be written as,

$$\dot{V} = S^T \frac{\partial S}{\partial x}\dot{x} \tag{3.37}$$

$$= S^T C_s (Ax + B_1 u + B_e e + B_2 r). \tag{3.38}$$

Substituting $u = u_{eq} + u_N$, with u_{eq} from (3.36) and u_N from (3.29), in (3.38), yields the following $\dot{V}$ after manipulation.

$$\dot{V} = -\|B_1^T C_s^T C_s x\|_2(\rho + \alpha) + (C_s x)^T C_s B_e e. \tag{3.39}$$

Now $B_e = \begin{bmatrix} B_i & 0 \\ 0 & -D_i \end{bmatrix}$ is written as,

$$B_e = \begin{bmatrix} B_i & 0 \\ 0 & -D_i \end{bmatrix} = \begin{bmatrix} B_i \\ -D_i \end{bmatrix} X. \tag{3.40}$$

Solving the above matrix equation for X gives,

$$X = (B_i^T B_i + D_i^T D_i)^{-1} \begin{bmatrix} B_i^T B_i & D_i^T D_i \end{bmatrix}. \tag{3.41}$$

Now using (3.40) in (3.39) gives,

$$\begin{aligned} \dot{V} &= -\|B_1^T C_s^T C_s x\|_2(\rho + \alpha) + (C_s x)^T C_s \begin{bmatrix} B_i \\ -D_i \end{bmatrix} Xe \\ &= -\|B_1^T C_s^T C_s x\|_2(\rho + \alpha) + (C_s x)^T C_s B_1 Xe \\ &= -\|B_1^T C_s^T C_s x\|_2(\rho + \alpha) \\ &\quad + (C_s x)^T C_s B_1 (B_i^T B_i + D_i^T D_i)^{-1} \begin{bmatrix} B_i^T B_i & D_i^T D_i \end{bmatrix} e. \end{aligned} \tag{3.42}$$

Since $\|(B_i^T B_i + D_i^T D_i)^{-1} \begin{bmatrix} B_i^T B_i & D_i^T D_i \end{bmatrix} e\|_2 < \rho$, the above equation implies that $\dot{V} \leq -\|B_1^T C_s^T C_s x\|_2 \alpha$. As $\alpha > 0$, this proves the negative definiteness of the candidate Lyapunov function V. Therefore the sliding surface is attractive for the closed loop system.

Chattering: In order to avoid chattering associated with the SMC, the control input is made continuous if the 2-norm of the sliding surface lies inside a boundary layer of 2ϵ thickness. This is shown in (3.43).

$$u = \begin{cases} u_{eq} - \frac{B_1 C_s^T C_s x}{\|B_1 C_s^T C_s x\|_2}(\rho + \alpha), & \text{if } \|S\|_2 \geq \epsilon, \\ u_{eq} + p(x), & \text{otherwise.} \end{cases} \tag{3.43}$$

Here $p(x)$ is the following function,

$$p(x) = -\frac{B_1 C_s^T C_s x}{\|B_1 C_s^T C_s x\|_2}(\rho + \alpha)\frac{\|S\|_2}{\epsilon}. \tag{3.44}$$

The control input in (3.43) attracts the vehicle states to the boundary layer. If the vehicle is within the boundary layer, then it provides a continuous control input that approximates the otherwise discontinuous control input so that chattering is avoided.

TUCC TUNING

The TUCC has three tuning parameters, ϵ, α and ρ. As seen in (3.44), the sum of α and ρ is used to calculate the control input. Therefore tuning one of them is enough. Hence α is set to a positive value of 0.006 and ρ is tuned. It should be noted that α can be another positive value which yields a positive value of ρ while tuning. The value of ϵ determines how much chattering is observed in the control input u. For tuning ϵ, a steady state cornering with radius of curvature 152.4 m and $v = 80$ km/h is simulated with the TUCC ON. The value of ϵ, by influencing the transition from the continuous operation mode to the effective sliding mode, affects the stability. If ϵ is too small, the transition between the two operating modes causes sustained oscillations as seen in Figure 3.11. It should be noted that for non-zero ϵ values, once the vehicle states are inside the boundary layer, until the vehicle states go outside the boundary layer, the control input is a continuous approximation of the discontinuous control as shown in (3.43) and (3.44).

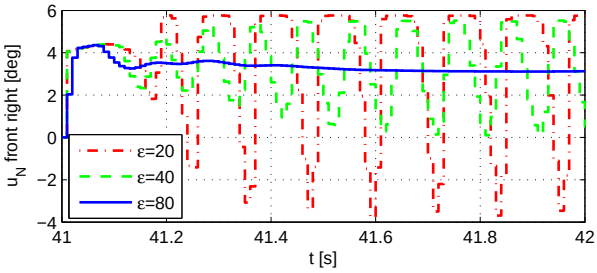

Figure 3.11: Effect of different values of ϵ on u_N.

The value of ρ is tuned using a Sine with Dwell (SWD) maneuver. In a SWD maneuver, the vehicle goes at a constant speed of 80 km/h and the driver steering wheel input is a SWD signal. The top plot in Figure 3.14 shows the SWD steering profile. The SWD maneuver has a frequency of 0.7 Hz without the 0.5 s pause during the second peak. The SWD maneuver is chosen as it is known to excite the vehicle's nonlinearities.

The value of ρ is first set to its lower limit calculated with the help of (3.10) and (3.40) during a SWD maneuver with amplitude 150 deg. Further it is increased. For higher values, higher overshoots are observed in the yaw rate and lateral acceleration once the SWD cycle is over. ρ is increased till 0.104 where the overshoot is less than 10 %. Finally the tuned value of 0.104 is multiplied by the road-tyre friction μ so that the steering actuation is scaled depending on the friction.

GAIN SCHEDULING TO IMPROVE ROBUSTNESS TO VEHICLE SPEED

The TUCC has been derived for the 80 km/h case. Therefore when the vehicle speed is varied, the upper bound of lumped vector norm $\|(B_i^T B_i + D_i^T D_i)^{-1} \begin{bmatrix} B_i^T B_i & D_i^T D_i \end{bmatrix} e\|_2$ i.e. ρ might be different. As a consequence if simulations are run at different speeds with the same TUCC, there may be a loss of performance. This can be avoided by gain scheduling with the vehicle speed. This way the value of ρ will be more accurate. Therefore a speed dependent gain scheduling is developed so that the TUCC is robust to vehicle speed. The changes in the TUCC are the vehicle model used for SMC design and the

SMC parameter ρ. The vehicle model is linearized at different speeds so that the model's speed dependency is considered. ρ is tuned in closed loop with the TUCCs designed at different vehicle speeds.

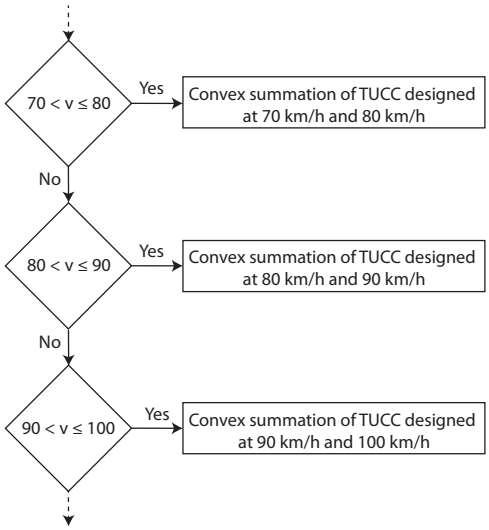

Figure 3.12: Speed dependent gain scheduling.

As shown in Figure 3.12, gain scheduling uses convex summation of control inputs calculated at two different vehicle speeds. The following equations explain the convex summation used.

$$u_{convex} = G_{v_1} u_{v_1} + G_{v_2} u_{v_2} \text{ where,} \tag{3.45}$$
$$G_{v_1} = \frac{v - v_1}{10}, \tag{3.46}$$
$$G_{v_2} = 1 - G_{v_1}, \tag{3.47}$$
$$v_2 - v_1 = 10, \tag{3.48}$$
$$v_1 < v \leq v_2. \tag{3.49}$$

Here u_{convex} is the control input calculated using convex summation, G_{v_1} and G_{v_2} are non-negative real numbers, u_{v_1} and u_{v_1} are the TUCC control inputs calculated at vehicle speeds v_1 and v_2 respectively, and v is the vehicle speed. The convex summation is done using different control inputs and not using convex summation of system matrices as the latter will require real-time controller design which is computationally expensive. Outside the speed range $(v_1, v_2]$, gain scheduling continues in the same way.

3.4. RESULTS

BOTH the TUCC as well as SACs are implemented in Simulink environment and the TUCC is co-simulated with CarSim, a multi-body vehicle simulator. Several simulation experiments are performed to study the closed loop performance. First the vehicle

is simulated for a ramp steering input. Here the objective is to study whether the TUCC is able to meet its objective in (3.19). Next, lateral stability is studied with a Sine with Dwell (SWD) maneuver. Then vehicle lateral acceleration is studied for higher steering wheel angles. Finally the controller is tested for its robustness to vehicle speed, force measurement noise and road-tyre friction.

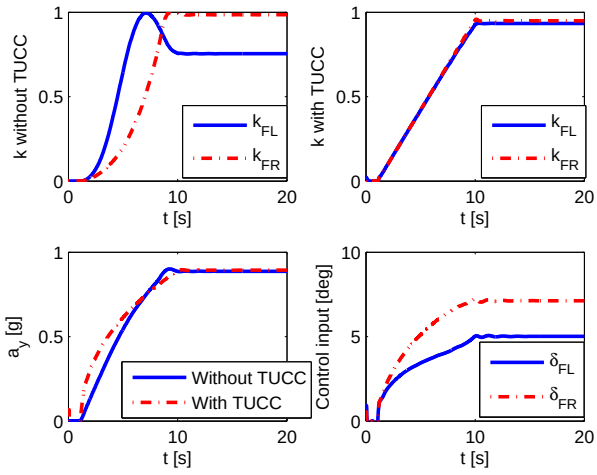

Figure 3.13: Simulation results for a ramp input with and without TUCC.

First the ramp steering input case is discussed. In this simulation experiment, the vehicle goes at a constant speed of 80 km/h and the steering wheel input from the driver is increased from 0 to 150 deg in 0 to 10 s. After $t = 10$ s, the steering wheel input is kept constant at 150 deg. In this simulation, the right tyre is the inner tyre.

The vehicle is simulated for this driver input with and without the TUCC. Further it is studied whether the TUCC objective in (3.19) is met. From Figure 3.13, the following observations can be made.

- Without TUCC, the TUCs of the front tyres are not equal whereas with TUCC, the tyres are equally utilized i.e. $k_{FL} = k_{FR}$.
- With TUCC, the lateral acceleration a_y has less overshoot when the ramp reaches its maximum value at $t = 10$ s.
- It should be noted that there is not much improvement in the closed loop lateral acceleration because the steering wheel angle (150 deg) is not considerably higher than the 135 deg threshold shown in Figure 3.9. Such a case where the steering wheel angle is considerably higher than the 135 deg threshold is discussed in Section 3.4.3.

Now that the controller is found to be able to meet its objective, in a quasi-static test, its dynamical properties are further studied.

3.4.1. LATERAL DYNAMICS STABILITY

The top plot in Figure 3.14 shows the applied SWD steering input to study lateral dynamics stability. The SWD maneuver is known to excite the vehicle's nonlinearities as the tyre forces could reach their nonlinear operating region depending on the vehicle speed. Whether the vehicle is stable or unstable is defined using the stability criteria (SC) in (3.50) and (3.51) [28].

$$SC_1 = \frac{\dot{\psi}_{t_0+1.00}}{\dot{\psi}_{Peak}} \times 100 \leq 35\%, \tag{3.50}$$

$$SC_2 = \frac{\dot{\psi}_{t_0+1.75}}{\dot{\psi}_{Peak}} \times 100 \leq 20\%. \tag{3.51}$$

Here, SC_1 means that, after 1.0 s of the SWD steering cycle, the yaw rate of the vehicle has to be less than or equal to 35% of the first local peak yaw rate produced by the steering reversal. SC_2 means that, after 1.75 s of the SWD steering cycle, the yaw rate of the vehicle has to be less than or equal to 20% of the first local peak yaw rate produced by the steering reversal.

In order to compare the proposed controller, a PI based VDC is used. The PI based VDC controls the vehicle yaw rate using steering actuator and it employs a typical yaw rate reference model [5]. Steering actuator is chosen for the PI based VDC because the TUCC uses steering actuator and this way, the controllers performances can be compared for equal control input costs. Therefore the PI based VDC is tuned such that the quadratic control input cost is equal to that of the TUCC for the chosen SWD maneuver.

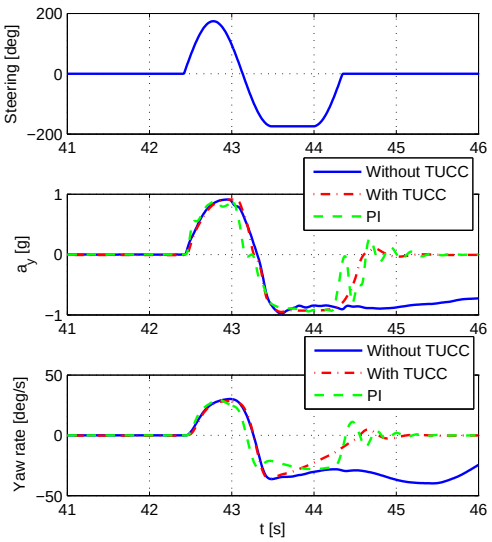

Figure 3.14: Simulation results for SWD maneuver with and without TUCC.

Table 3.2: SC_1 and SC_2 for SWD maneuver with and without the TUCC

$TUCCstatus$	SC_1	SC_2	$SC_1 \leq 35\%$	$SC_2 \leq 20\%$
OFF	109.52	66.21	No	No
ON	−0.86	0.47	Yes	Yes

In Figure 3.14, the lateral acceleration and yaw rate during the SWD maneuver are also shown. The following observations can be made from these plots.

- Without TUCC, the yaw rate is not coming back to zero once the SWD cycle is over. This implies that the vehicle is spinning out of control. Whereas with TUCC, the yaw rate comes back to zero once the SWD cycle is over.

- SC_1 and SC_2 are calculated from the yaw rate plots and are given in Table 3.2. It is clear that without TUCC, both the stability criteria in (3.50) and (3.51) are not met whereas with TUCC, they are met.

- The TUCC is able to maintain lateral acceleration a_y as defined in (3.22), especially once the SWD cycle is over i.e. it is able to bring a_y to zero. Whereas without the TUCC, a_y does not come back to zero and this means the vehicle is oversteering, a behavior the driver is not desiring with his steering input.

- The PI based VDC is able to stabilize the vehicle. However the yaw rate has an overshoot of the order 11 deg/s once the SWD is over. Whereas for the same quadratic control input cost i.e. for the same control effort, the TUCC stabilizes the vehicle without such high overshoot in the yaw rate.

These considerations show that the TUCC is able to keep the vehicle stable for the applied SWD steering input whereas without the TUCC, the vehicle is not stable.

In the top left and right plots of Figure 3.15, the TUCs are shown for the SWD maneuver. The following observations can be made from the TUC plots.

- With control, the front TUCs are closer to being equal when compared with the case without control, especially during the second half cycle of the SWD.

- Without control, the TUCs are not brought close to zero after the SWD cycle and this corresponds to the vehicle spinning out of control. Whereas with control, the TUCs are brought close to zero once the SWD cycle is over, which means the vehicle is not spinning out of control, hence it is stable.

In conclusion, application of the SWD maneuver has shown that using the TUCC with the objective of keeping the front left and right TUC equal can keep the vehicle stable in situations where the vehicle would have lost stability. In the bottom left and right plots of Figure 3.15, break up of the Sliding Mode control inputs generated by the TUCC, u_{eq} and u_N, are shown. In Figure 3.16, the control inputs generated by both controllers are shown.

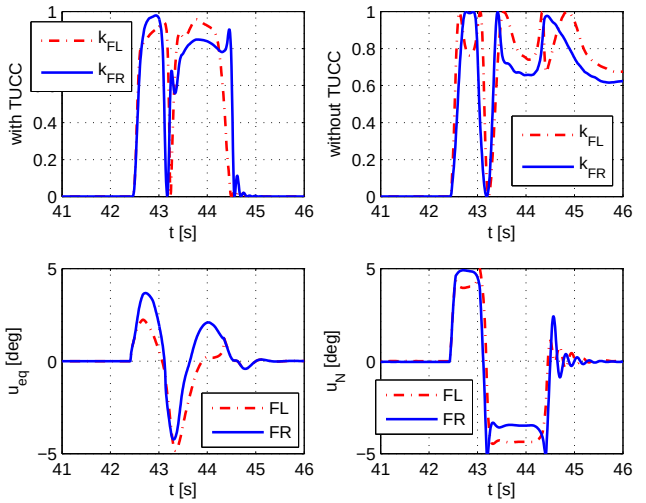

Figure 3.15: TUCs and control inputs $\{u_{eq}, u_N\}$ during the SWD maneuver.

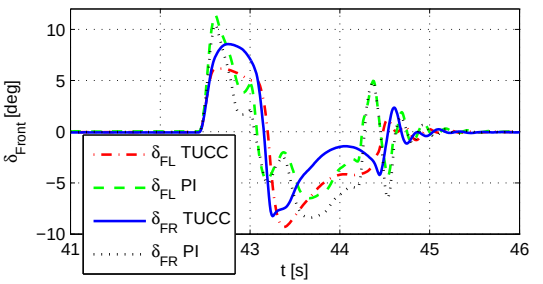

Figure 3.16: Control inputs generated by the TUCC and PI based VDC.

3.4.2. ROBUSTNESS TO SWD AMPLITUDE

For SWD amplitudes higher than the one in Figure 3.14, it is observed that the vehicle states, vehicle sideslip and yaw rate, and the outputs, front left and right lateral tyre forces, are almost equal to the results shown in Section 3.4.1. This is because the force references in (3.25) and (3.26) have limits as they are calculated based on the bounded lateral acceleration reference in (3.22).

3.4.3. MAINTAINING THE MAXIMUM POSSIBLE LATERAL ACCELERATION FOR HIGHER STEERING ANGLES

In this section, the vehicle lateral acceleration is studied for increasing steering wheel angle at a constant speed of 80 km/h. The steering wheel angle profile is shown in bottom right plot of Figure 3.17.

Further, the vehicle lateral acceleration is studied with and without the TUCC. From

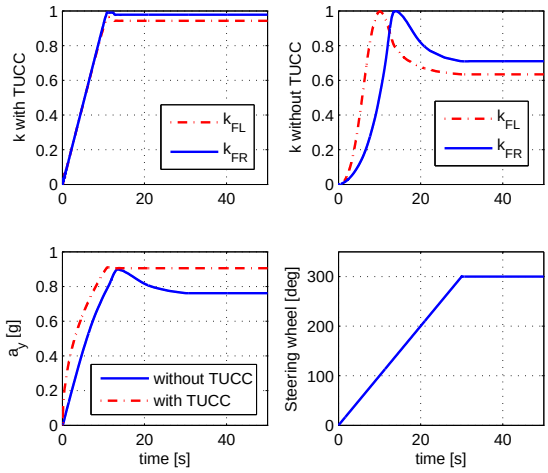

Figure 3.17: Effect of the TUCC on lateral acceleration for higher steering wheel angles.

Figure 3.17, it can be observed that without TUCC, the lateral acceleration reduces as the steering wheel angle is increased to more than 135 deg. Whereas with TUCC, when the steering wheel angle is increased to more than 135 deg, the lateral acceleration is maintained very close to its maximum possible value. Without TUCC, it can be observed that the TUCs reduce for steering wheel angles higher than 135 deg whereas with TUCC, the TUCs are maintained very close to 1, hence the lateral acceleration is maintained close to its maximum possible value. Such a situation can happen when an average skilled driver applies steering higher than a certain threshold assuming he will get more lateral acceleration. It must be noted that this benefit is applicable only on road conditions that facilitates a peak followed by negative slope in lateral tyre force characteristics.

3.4.4. ROBUSTNESS TO VEHICLE SPEED

In this section, the speed dependent gain scheduled controller is compared against the nonscheduled controller. As shown in Figure 3.18(a), with the initial TUCC, i.e. the one designed with the model linearized at 80 km/h, as the vehicle speed is increased from 80 to 100 km/h, the vehicle is not following its lateral acceleration reference and the stability criteria in (3.50) is not met. But with the gain scheduled controller, the vehicle is no more unstable whereas the open loop case is unstable. The speed dependent gain scheduling increases the controller robustness.

Figure 3.18(b) shows the case when the vehicle speed is increased to 120 km/h. With the gain scheduled controller, the vehicle is observed to be stable whereas in the open loop case the vehicle is spinning out of control. However the closed loop performances are not as good as compared to slower vehicle speeds and this is a limitation of the TUCC. It might be resulting from the unmodelled dynamics.

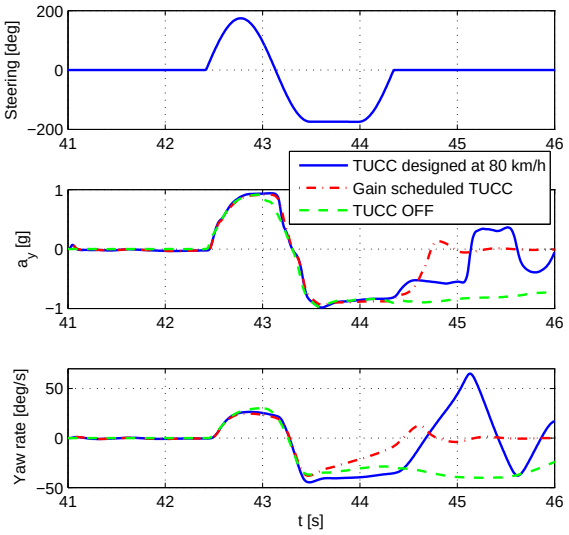

(a) At vehicle speed 100 km/h.

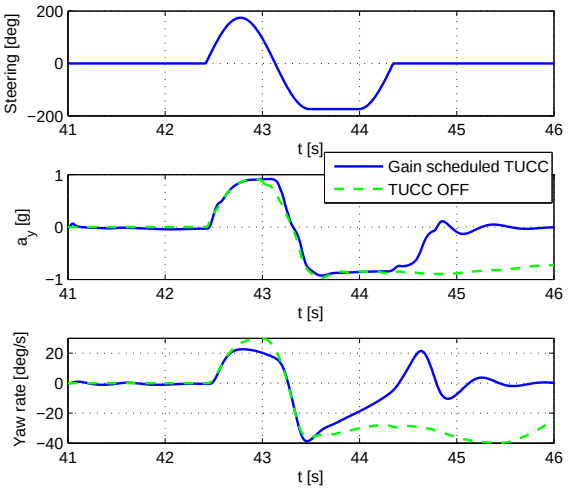

(b) At vehicle speed 120 km/h.

Figure 3.18: Simulation results for SWD maneuver with speed dependent gain scheduled controller.

3.4.5. ROBUSTNESS TO MEASUREMENT NOISE

In this section, simulation experiments are performed to study the closed loop robustness to measurement noise of the force sensors. The tyre force measurements from Car-

Sim is polluted with a uniform distributed noise in the range $[-500\,\text{N}, 500\,\text{N}]$. This is approximately 10 % of the force range. Figure 3.19 shows a sample longitudinal force measurement from our test vehicle. It is clear from the sample measurement that the peak to peak noise is less than the considered range $[-500\,\text{N}, 500\,\text{N}]$ (See Section 6.2.1 for more details on the sensor noise). Yaw rate measurement is also polluted with a uniform distributed noise in the range $[-2.5\,\text{deg/s}, 2.5\,\text{deg/s}]$ which is approximately 10 % of the yaw rate seen during the SWD simulation.

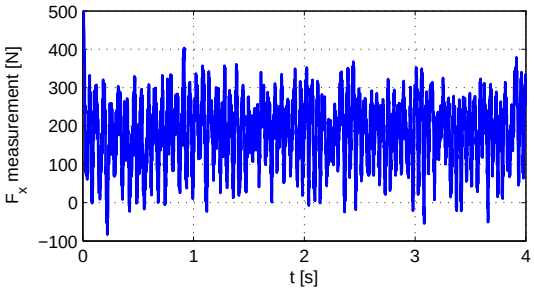

Figure 3.19: A sample longitudinal force measurement from the test vehicle fitted with the tyre force sensors.

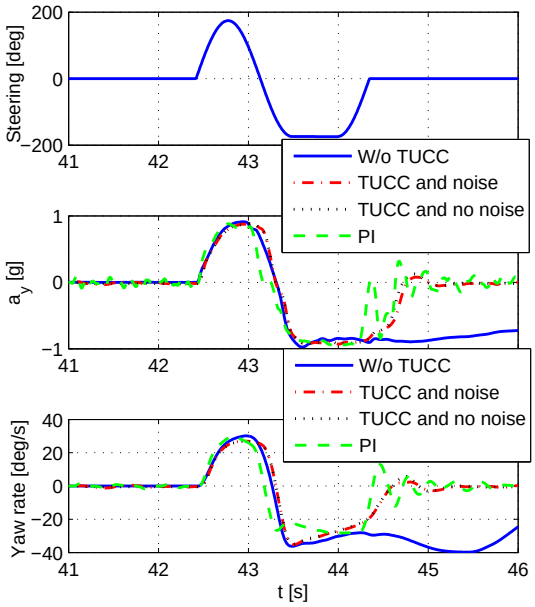

Figure 3.20: Steering wheel angle, lateral acceleration and yaw rate during SWD maneuver with force measurement noise.

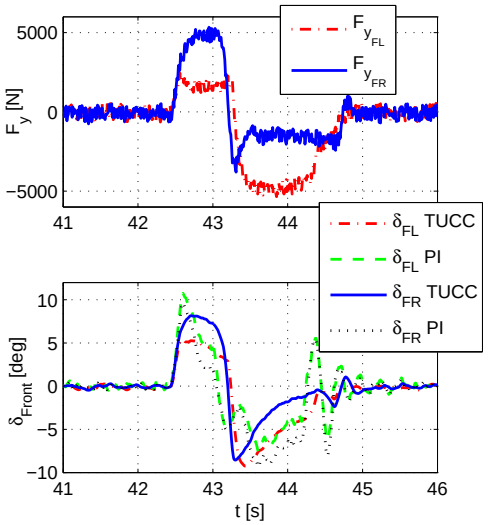

Figure 3.21: Lateral tyre forces and control input during SWD maneuver with force measurement noise.

Figure 3.20 shows the lateral acceleration and yaw rate from this study. The simulations are done at a vehicle speed of 80 km/h. Both TUCC and PI based VDC have the same tuning settings as in Section 3.4.1. It is clear from these plots that the TUCC is able to keep the vehicle stable when compared with the uncontrolled case and there is not much difference with respect to the noiseless case. It is also observed that the PI based VDC is able to stabilize the vehicle in the presence of measurement noise.

In Figure 3.21, the lateral tyre forces of the front tyres and the control inputs generated by the controllers are plotted. It can be observed from the lateral force plots that although the noise level is quite prominent, the control inputs shown in the bottom plot are able to keep the vehicle stable.

3.4.6. ROBUSTNESS TO ROAD-TYRE FRICTION

In this section, simulation experiments are performed to study the closed loop robustness to different peak road-tyre friction. The simulations are done at 80 km/h using SWD steering input and the results are shown in Figure 3.22. In these simulations, both TUCC and PI based VDC have the same tuning settings as in Section 3.4.1. Figure 3.22(a) shows the simulation results with peak road-tyre friction 0.6. The following observations can be made.

- Without TUCC, the vehicle yaw rate and lateral acceleration do not return to zero once the SWD cycle is over. Instead there is a very high overshoot. With TUCC, they return to zero.
- With the PI based VDC, the yaw rate returns to zero, however there is a considerable lag i.e. the yaw rate returns to zero approximately 1 s after the SWD ends.

Therefore the TUCC performance is better than the PI based VDC.

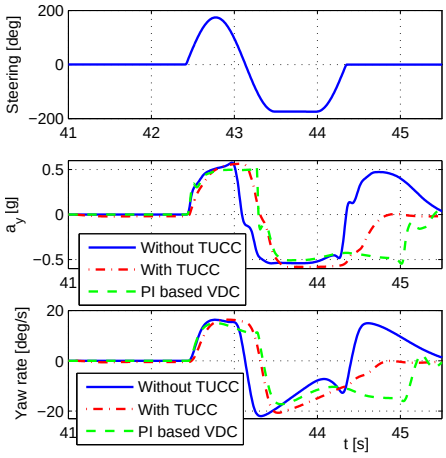

(a) With peak road-tyre friction 0.6.

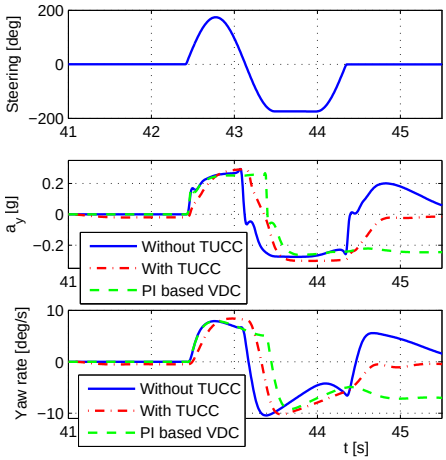

(b) With peak road-tyre friction 0.3.

Figure 3.22: Simulation results for SWD maneuver with different peak road-tyre friction values.

Figure 3.22(b) shows the simulation results with peak road-tyre friction 0.3. The following observations can be made.

- Without TUCC, the vehicle yaw rate and lateral acceleration do not return to zero once the SWD cycle is over. This implies that the vehicle is spinning undesirably. With TUCC, the vehicle is stable.

- The PI based VDC is not able to stabilize the vehicle.

Therefore it is seen that the TUCC is robust to road-tyre friction. The main reason for the robustness is that the TUCC controls the Tyre Utilization Coefficients which depend on the tyre forces and road-tyre friction, and the tuning parameter ρ depends on the friction.

3.5. CONCLUSIONS

A NEW method for lateral vehicle dynamics control using tyre force measurements and active front steering is proposed in this chapter. First, a simulation study exemplifies the fact that during cornering the TUCs are not evenly employed. This can get one of the front tyres to hit saturation before the others, thereby possibly causing discomfort for an average driver or even an unstable situation. Next, the Tyre Utilization Coefficient Control is proposed to address this issue with the objective of keeping the front left and front right TUCs equal i.e. $k_{FL} = k_{FR}$. As a consequence of the proposed TUCC, the vehicle is able to maintain the maximum possible lateral acceleration when a driver applies higher steering angles. The TUCC is designed using SMC method. The proposed controller is tested in several conditions ranging from quasi-steady state cornering to a more dynamically demanding Sine with Dwell maneuver. During the ramp steering cornering, the TUCC is observed to be able to achieve the control objective $k_{FL} = k_{FR}$. During the SWD maneuver, it is observed that the vehicle is stable with the TUCC whereas the car goes unstable without the TUCC.

Secondly, another simulation study exemplifies that when an average driver applies steering higher than a certain threshold, assuming he will get more lateral acceleration, he might in fact be settling for a lesser lateral acceleration. Whereas with the TUCC, lateral acceleration is maintained very close to its maximum in such driving situations, thereby assisting the driver.

The TUCC is also found to be robust for different SWD amplitudes. In order to make the TUCC robust for different vehicle speeds, a speed dependent gain scheduling is used. The closed loop system is further tested in the presence of measurement noise and is found to be robust. Finally, the controller is studied for various peak road-tyre friction values and is found to be robust.

This chapter has demonstrated tyre force measurement based TUCC in simulation environment. In Chapter 5 and 6, road-tyre friction and vehicle sideslip estimators using tyre force measurements are studied as they are needed to implement the proposed TUCC. A limitation of the TUCC is that the closed loop performance seems to degrade as vehicle speed increases. This should be further studied.

4

YAW RATE CONTROL

4.1. INTRODUCTION

ELECTRONIC stability control (ESC) in commercial cars typically controls vehicle yaw rate using braking actuators as controlling vehicle yaw rate improves vehicle safety. The yaw rate is typically controlled as it is a controllable lateral vehicle dynamics state when the vehicle is modelled with braking or steering actuators, and it can be measured with sufficient accuracy. Braking actuators are typically used as they are already present in today's vehicles and they are cost effective. In this chapter, how tyre force measurements can benefit the yaw rate control problem using braking actuators is studied. A novel computationally inexpensive yaw rate controller using tyre force measurements is studied in this direction. Most of the current yaw rate controllers use a tyre model that introduces vehicle modeling error because of the tyre model nonlinearities and uncertainties. This may degrade the controller performance. On the other hand, modeling the vehicle with tyre force measurements improves the vehicle model accuracy and therefore improves the controller performance. The proposed yaw rate controller uses a nonlinear yaw rate model and feedback linearization based control design. A stability analysis is also provided for the closed loop vehicle.

The yaw rate control problem is studied without linearizing the yaw rate dynamics. As a result, the control design and control gain do not directly depend upon the vehicle speed and vehicle sideslip. This is achieved by combining tyre force measurement [14, 60] and feedback linearization based control. The proposed controller uses braking actuators and is computationally inexpensive due to its simplicity.

This chapter is structured as follows. Section 4.2 shows the yaw rate dynamics and defines the controller. In Section 4.3, the closed loop stability is studied. The proposed controller is simulated in closed loop and the results are discussed in Section 4.4. Section 4.5 concludes the findings and discusses further research direction.

Parts of this chapter have been published in proceedings of the 14^{th} European Control Conference [58].

4.2. YAW RATE DYNAMICS AND CONTROLLER

In this section, the yaw rate dynamics and controller are defined. The following equation represents the yaw rate dynamics.

$$J_z\ddot{\psi} = (F_{y_{FR}} + F_{y_{FL}})a - (F_{y_{RL}} + F_{y_{RR}})b + uc \tag{4.1}$$

Here J_z is the rotational moment of inertia around yaw axis, $\ddot{\psi}$ is the yaw acceleration, $F_{y_{ij}}$ is the lateral tyre force of ij tyre and u is the control input using braking actuators. a, b and c are vehicle dimensions as shown in Figure 4.1. The control input u is the difference between the longitudinal forces of the right and left tyres, $u = (F_{x_{FR}} + F_{x_{RR}}) - (F_{x_{FL}} + F_{x_{RL}})$. It's desired value is shown in the controller Section 4.2.1 and it is realized using the brake torque allocation in Section 4.2.2.

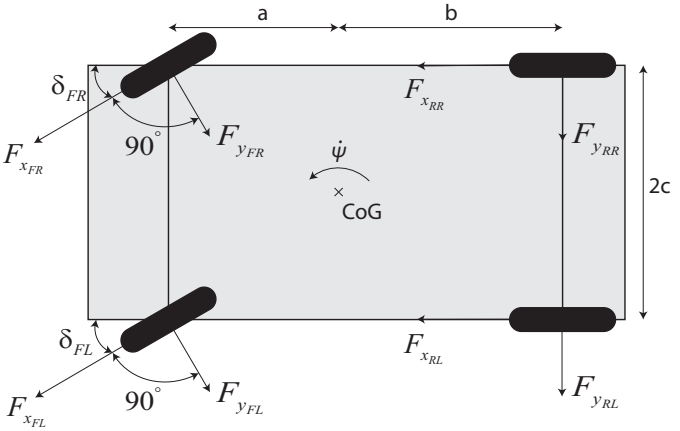

Figure 4.1: Simplified vehicle model used for controller design.

4.2.1. CONTROLLER

The proposed control structure is shown in Figure 4.2. The Yaw Rate Reference block generates the desired steady state yaw rate depending on the driver inputs steering angle and vehicle velocity. It is defined by (4.2) and (4.3) [36].

$$\dot{\psi}_{ref} = \frac{(V/L)\delta}{1 + \frac{\eta}{gL}V^2} \tag{4.2}$$

$$\max(|\dot{\psi}_{ref}|) = \frac{\mu g}{V} \tag{4.3}$$

Here $\dot{\psi}_{ref}$ is the yaw rate reference, V is the vehicle velocity, $L = a + b$, $\delta = (\delta_{FL} + \delta_{FR})/2$, η is the vehicle understeer coefficient, g is earth's gravity and μ is the road-tyre friction. The value of η is chosen as 0.0171 rad/g, the understeer coefficient of the linearized CarSim vehicle model. In this chapter, $\max(|\dot{\psi}_{ref}|)$ in (4.3) is calculated with $\mu = 1$.

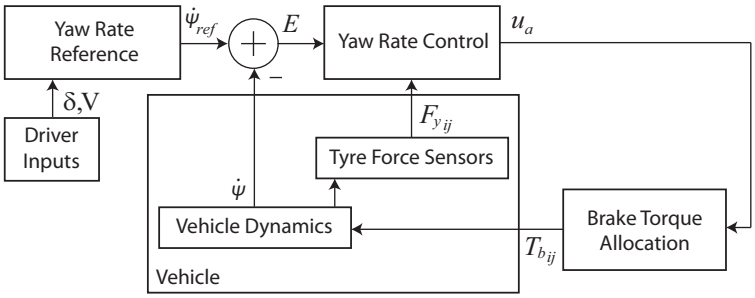

Figure 4.2: Control scheme of the proposed yaw rate controller.

The Yaw Rate Control block contains the proposed Feedback Linearization [38] based controller. In Feedback Linearization, a nonlinear system is linearized using feedback control. The control input has typically two parts, the first part cancels the nonlinearities of the system and the second part improves the closed loop robustness by placing the eigenvalues. This approach improves robustness and allows placing of the closed loop eigenvalue. However, cancelling nonlinearities may not be possible in a nonlinear system depending on the state equation structure. For example, with the vehicle yaw rate model using a nonlinear tyre model such as Magic formula, it is difficult to design a control input that cancels the nonlinearities and provide robust stability, whereas with the vehicle yaw rate model using tyre force measurements (as shown in (4.1)), Feedback Linearization is possible. The proposed Feedback Linearization based control is defined in (4.4).

$$u = \frac{1}{c}\left(J_z\ddot{\psi}_{ref} - (F_{y_{FR}} + F_{y_{FL}})a + (F_{y_{RL}} + F_{y_{RR}})b\right) + \frac{J_z}{c}\left(\dot{\psi}_{ref} - \dot{\psi}\right)\gamma \tag{4.4}$$

Here $\ddot{\psi}_{ref}$ is the derivative of yaw rate reference and γ is a positive calibration parameter. The control input u in (4.4) is realized using the Brake Torque Allocation block described in Section 4.2.2. It uses low level brake torque allocation at each tyres. It must be noted that in (4.4), the first term with denominator c cancels the nonlinearities and the second term with denominator c improves closed loop robustness by placing the eigenvalue. If tyre force measurements were not available, the cancellation of the nonlinearities is challenging as a nonlinear tyre model based approach would heavily suffer from tyre model uncertainties.

The controller is on or off depending on the yaw rate error as shown in Figure 4.3. To avoid chattering, there is a linear transition phase when the yaw rate error magnitude is between 2 and 3 deg/s. This is shown mathematically in (4.5). Here u_a is the allocated control input.

$$u_a = \begin{cases} 0 & \text{if } |\dot{\psi}_{ref} - \dot{\psi}| < 2 \\ u\left(|\dot{\psi}_{ref} - \dot{\psi}| - 2\right) & \text{if } 2 < |\dot{\psi}_{ref} - \dot{\psi}| < 3 \\ u & \text{otherwise} \end{cases} \tag{4.5}$$

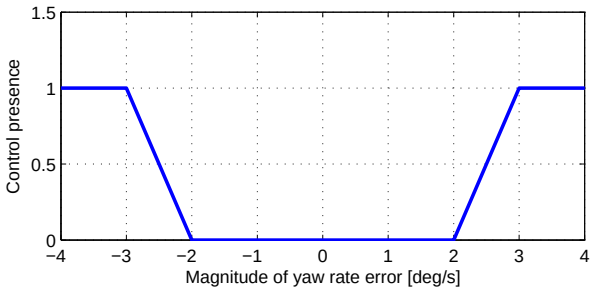

Figure 4.3: Control presence as a function of yaw rate error magnitude.

The dead zone in Figure 4.3 when the yaw rate error magnitude is less than 2 deg/s is used to turn the controller off in unnecessary situations. Otherwise, the controller will be on as soon as there is a small yaw rate error that does not cause any safety issue, and since braking actuators are used, this will reduce the fuel efficiency and increase tyre wear.

4.2.2. BRAKE TORQUE ALLOCATION

In the Brake Torque Allocation block in Figure 4.2, the desired brake torques for each tyres are determined as shown below.

$$T_{d_{FL}} = \begin{cases} r\,u_a \frac{b}{L} & \text{if } u_a > 0 \\ 0 & \text{otherwise} \end{cases} \tag{4.6}$$

$$T_{d_{FR}} = \begin{cases} 0 & \text{if } u_a > 0 \\ -r\,u_a \frac{b}{L} & \text{otherwise} \end{cases} \tag{4.7}$$

$$T_{d_{RL}} = \begin{cases} r\,u_a \frac{a}{L} & \text{if } u_a > 0 \\ 0 & \text{otherwise} \end{cases} \tag{4.8}$$

$$T_{d_{RR}} = \begin{cases} 0 & \text{if } u_a > 0 \\ -r\,u_a \frac{a}{L} & \text{otherwise} \end{cases} \tag{4.9}$$

Here $T_{d_{ij}}$ is the desired brake torque of the ij tyre and r is the effective tyre radius. Instead of two, all four tyres are used for the control input allocation as it creates more differential brake force.

In order to realize the desired brake torques, a first order brake actuator dynamics is considered. The brake torque depends on the hydraulic pressure of the wheel cylinder. The pressure is controlled by solenoid valves through the combination of pressure build-up, hold and reduce states. The pressure in the brake actuator including the solenoid valves can be approximated by a first order transfer function in (4.10) [40].

$$P_{b_{ij}} = \frac{P_{d_{ij}}}{1+\tau s} e^{-st_d} \tag{4.10}$$

$$T_{b_{ij}} = 2A_c P_{b_{ij}} \mu_{br} r_{br} \tag{4.11}$$

Here $P_{d_{ij}}$ is the pressure demand through the solenoid, $P_{b_{ij}}$ is the brake cylinder pressure, s is the Laplace variable and t_d is the hydraulic transport delay. The brake torque $T_{b_{ij}}$ is a function of the brake cylinder pressure $P_{b_{ij}}$ as shown in (4.11). Here A_c is the brake piston area, μ_{br} is the brake pad friction coefficient and r_{br} is the brake disc radius. Therefore, to realize the desired brake torque $T_{d_{ij}}$, the following brake pressure demand is applied to the actuator.

$$P_{d_{ij}} = \frac{T_{d_{ij}}}{2A_c \mu_{br} r_{br}} \tag{4.12}$$

Instead of a cascade control approach where the desired control input in (4.5) is distributed using longitudinal force controllers, the brake pressure approach is chosen as it is effective and computationally inexpensive. In situations where the wheels might lock, a force-based Antilock Brake System (ABS), which considers the lateral force demand from the driver, could be incorporated [16]. However in this work, ABS is not used to allocate the control input.

4.3. CONTROLLER STABILITY

THE controller stability is studied in this section using closed loop stability analysis. The yaw rate dynamics in (4.1) is rewritten as follows using the control input u in (4.4).

$$\begin{aligned} J_z\ddot{\psi} =& (F_{y_{FR}} + F_{y_{FL}})a - (F_{y_{RL}} + F_{y_{RR}})b \\ &+ \left(\frac{1}{c}\left(J_z\ddot{\psi}_{ref} - (F_{y_{FR}} + F_{y_{FL}})a + (F_{y_{RL}} + F_{y_{RR}})b\right) + \frac{J_z}{c}\left(\dot{\psi}_{ref} - \dot{\psi}\right)\gamma\right)c. \end{aligned} \tag{4.13}$$

The above equation shows the closed loop yaw rate dynamics. Now to study the yaw rate error dynamics in closed loop, the yaw rate error E is defined as follows.

$$E = \dot{\psi}_{ref} - \dot{\psi} \tag{4.14}$$

Here the yaw rate $\dot{\psi}$ obeys the closed loop dynamics defined in (4.13). If the closed loop yaw rate error dynamics $\dot{E}$ is stable, the proposed controller is stabilizing. This is further studied with the following Lyapunov function.

$$V_L(t) = \frac{1}{2}E^2 \tag{4.15}$$

For the closed loop error dynamics to be stable, the following inequality should be true [38, 39].

$$\dot{V}_L(t) \leq -\alpha(|E|) \tag{4.16}$$

Here $\alpha(|E|)$ is a *class K* function i.e. for the domain $|E| \in [0, R]$ it is defined, $\alpha(|E|)$ is strictly increasing and $\alpha(0) = 0$ [39]. Now (4.16) is rewritten as follows.

$$\dot{V}_L(t) = \frac{\partial V_L}{\partial E}\dot{E} \leq -\alpha(|E|) \tag{4.17}$$

Using (4.15) in (4.17) gives,

$$\dot{V}_L(t) = E\dot{E} \leq -\alpha(|E|). \tag{4.18}$$

Using (4.14) in (4.18) gives,

$$\dot{V}_L(t) = \left(\dot{\psi}_{ref} - \dot{\psi}\right)\left(\ddot{\psi}_{ref} - \ddot{\psi}\right) \leq -\alpha(|E|) \text{ i.e.,} \tag{4.19}$$

Now using the closed loop yaw rate dynamics from (4.13) in (4.19) gives,

$$\begin{aligned}\dot{V}_L(t) &= \left(\dot{\psi}_{ref} - \dot{\psi}\right)\ddot{\psi}_{ref} \\ &- \frac{\dot{\psi}_{ref} - \dot{\psi}}{J_z}\left[(F_{y_{FR}} + F_{y_{FL}})a - (F_{y_{RL}} + F_{y_{RR}})b\right] \\ &- \frac{\dot{\psi}_{ref} - \dot{\psi}}{J_z}\left(\frac{1}{c}\left(J_z\ddot{\psi}_{ref} - (F_{y_{FR}} + F_{y_{FL}})a + (F_{y_{RL}} + F_{y_{RR}})b\right) + \frac{J_z}{s}\left(\dot{\psi}_{ref} - \dot{\psi}\right)\gamma\right)c.\end{aligned} \tag{4.20}$$

This is rewritten as,

$$\dot{V}_L(t) = -\left(\dot{\psi}_{ref} - \dot{\psi}\right)\left(\dot{\psi}_{ref} - \dot{\psi}\right)\gamma. \tag{4.21}$$

Considering the following *class K* function $\alpha(|E|)$ with $0 < \kappa < 1$,

$$\alpha(|E|) = \kappa\left(\dot{\psi}_{ref} - \dot{\psi}\right)\left(\dot{\psi}_{ref} - \dot{\psi}\right)\gamma, \tag{4.22}$$

$$\dot{V}_L(t) = -\left(\dot{\psi}_{ref} - \dot{\psi}\right)\left(\dot{\psi}_{ref} - \dot{\psi}\right)\gamma \leq -\alpha(|E|). \tag{4.23}$$

As γ is a positive calibration parameter, the yaw rate error dynamics is therefore stable with the proposed control in (4.4).

The closed loop stability can also be studied using the yaw rate error dynamics $\dot{E}$. Using (4.14), the yaw rate error dynamics can be written as follows.

$$\dot{E} \quad = \quad \ddot{\psi}_{ref} - \ddot{\psi}. \tag{4.24}$$

Using (4.13) in (4.24) and simplifying gives the feedback linearized error dynamics,

$$\dot{E} = -(\dot{\psi}_{ref} - \dot{\psi})\gamma, \tag{4.25}$$
$$= -\gamma E. \tag{4.26}$$

Here $\gamma > 0$ Hz as explained in Section 4.2.1. Therefore the closed loop yaw rate error dynamics has a negative eigenvalue $-\gamma$. This also proves stability of the closed loop yaw rate error dynamics.

4.3.1. CONTROLLER TUNING

The controller defined in (4.4) has a calibration parameter γ and it is tuned during simulation. A Sine with Dwell (SWD) steering input, shown in Figure 4.9, is applied to the closed loop vehicle for different values of γ. The vehicle is initialized at a speed of 80 kmph and Figure 4.4 shows the vehicle yaw rate for different values of γ.

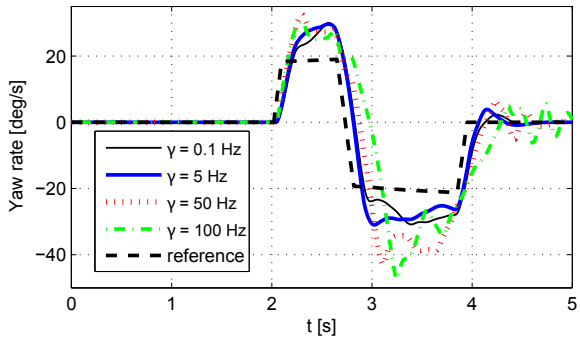

Figure 4.4: Vehicle yaw rate during the SWD maneuver at 80 kmph for different values of γ.

As explained in Section 4.3, $-\gamma$ is the eigenvalue of the closed loop yaw rate error dynamics. Therefore non-positive value of γ is avoided to achieve closed loop stability. It is observed that for $\gamma = 100$ Hz, the yaw rate error is higher than the other cases and there are oscillations once the steering input is back to zero (see Figure 4.4 and Figure 4.9) after $t = 4$ s. The oscillations might be due to the unmodeled dynamics in designing the controller, for example the braking actuator and vehicle vertical dynamics. As γ is reduced to 50 Hz, the yaw rate error and oscillations are reduced. At $\gamma = 5$ Hz, the oscillations after $t = 4$ is minimal and further reduction of γ does not improve the performance significantly. In addition, further reduction reduces the controller robustness.

As seen in Figure 4.4, $\gamma = 0.1$ Hz gives slightly less overshoot after $t = 4$ s compared to the case with $\gamma = 5$ Hz. Still, $\gamma = 5$ Hz is chosen as it is observed that for SWD maneuvers with different vehicle speeds, $\gamma = 5$ Hz gives better controller robustness than for the case with $\gamma = 0.1$ Hz. Because the closer γ is to zero, the closer yaw rate eigenvalue is to the imaginary axis of the complex plane. As shown in Figure 4.5, at a vehicle speed of 115 kmph, $\gamma = 0.1$ Hz does not stabilize the vehicle, whereas the case with $\gamma = 5$ Hz stabilizes because it has better robustness. Therefore $\gamma = 5$ Hz is chosen.

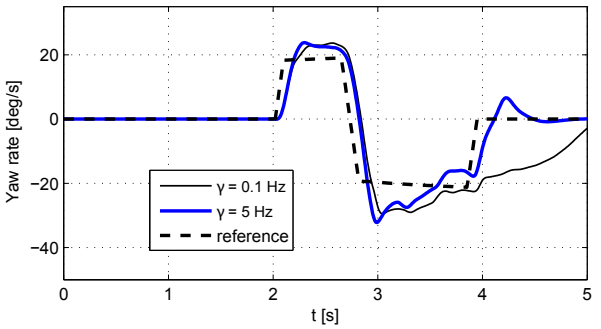

Figure 4.5: Vehicle yaw rate during the SWD maneuver at 115 kmph for different values of γ.

4.4. SIMULATION RESULTS

THE proposed controller is implemented in Simulink environment. The vehicle dynamics is simulated using CarSim multi-body vehicle simulator with 15 Degrees of Freedom [18]. The CarSim model uses a nonlinear tyre model with dependency on slip, load, and camber. In the controller implementation, a second order low pass filter (LPF) with 30 Hz bandwidth is used to filter the yaw rate reference derivative $\ddot{\psi}_{ref}$ in (4.4). The LPF is used to filter the noise in $\ddot{\psi}_{ref}$ which otherwise affects the controller performance.

The closed loop vehicle is studied with split-μ and Sine with Dwell (SWD) maneuvers. In a split-μ cornering, one side of the vehicle has lower friction than the other side. This might happen during snowy or rainy situations. It might also happen when tyres on one side are outside the road. Such unequal frictions on the left and right might cause undesired yaw rate.

SWD maneuvers are known to excite the vehicle's nonlinearities as the tyre forces could reach their nonlinear operating region depending on the vehicle speed [28].

4.4.1. SPLIT-μ CORNERING

In the considered split-μ cornering, the vehicle negotiates a maneuver with a constant steering wheel angle of 70 deg and an initial speed of 60 kmph. The engine throttle is kept zero and the vehicle experiences the split-μ profile shown in Figure 4.6.

From the simulation results shown in Figure 4.7, the following observations can be made.

- In the open loop, the vehicle yaw rate deviates from its reference when the split-μ begins at $t = 2$ s and the vehicle is not able to regain its initial yaw rate even after the split-μ ends at $t = 4$ s. With time, the vehicle gains very high yaw rate which might cause an accident. In the closed loop, the vehicle yaw rate tracks its reference value throughout the maneuver.

- In the open loop, after the split-μ i.e. when $t > 4$ s, the lateral acceleration reaches much higher values compared to before the split-μ i.e. when $t < 2$ s. This is undesired as the steering wheel angle hasn't changed. In the closed loop, the lateral acceleration doesn't gain such undesired high values.

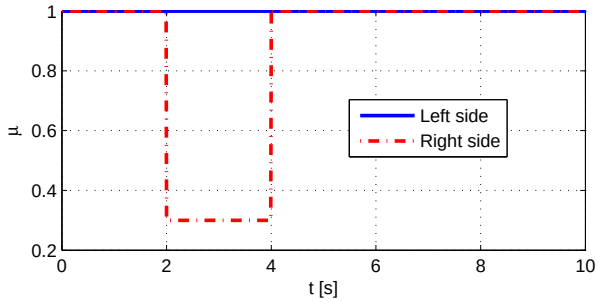

Figure 4.6: Split-μ friction profile.

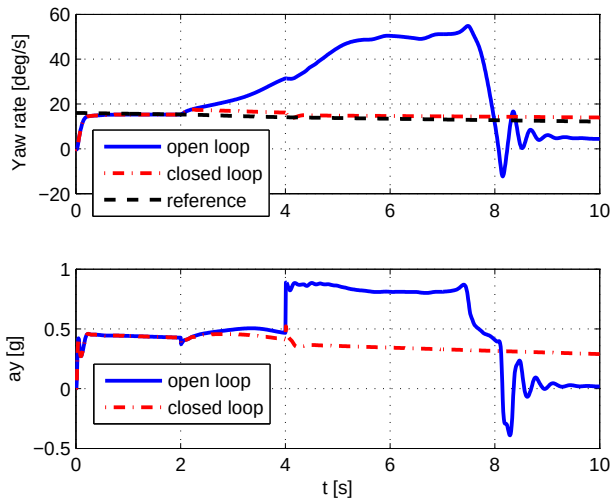

Figure 4.7: Vehicle yaw rate and lateral acceleration a_y during the split-μ cornering maneuver.

Therefore it is seen that the controller improves lateral vehicle safety during the split-μ cornering considered. It must be noted that the vehicle oversteers during the split-μ as the vehicle is cornering towards the left side and the split-μ act on the right tyres as shown in Figure 4.6.

The brake pressure applied by the controller is shown in Figure 4.8. In this simulation, the wheels do not lock. In situations where the wheels might lock, a force-based ABS that considers the lateral force demand could be used [16]. Next the closed loop vehicle is studied during SWD maneuvers.

4.4.2. SINE WITH DWELL

The steering wheel profile of the applied SWD cycle is shown in Figure 4.9. It has a peak to peak amplitude of 175 deg and the vehicle has an initial speed of 80 kmph. The vehicle

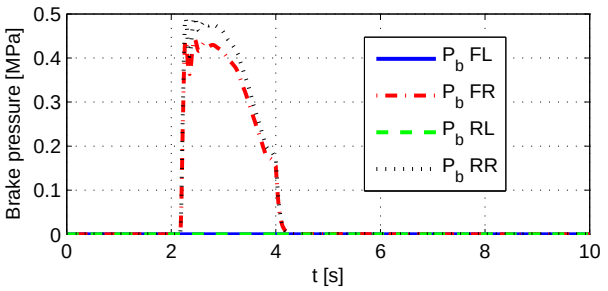

Figure 4.8: Brake pressure applied by the controller during the split-μ cornering maneuver.

4

stability is studied based on the vehicle yaw rate response, especially during and after the second half of the SWD cycle.

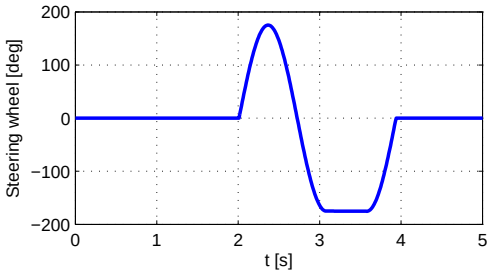

Figure 4.9: Steering wheel profile of the applied SWD cycle.

In order to compare the proposed controller, a PI based yaw rate controller is used. The PI controller also uses braking actuators to control the vehicle yaw rate. This way, the controller performances can be compared for equal control input costs. Therefore the PI based yaw rate controller is tuned such that the quadratic control input cost is equal to that of the proposed yaw rate control for the chosen SWD maneuver. It must be noted that the controllers may also be compared the other way around, i.e. for equal quadratic state error cost, compare the control input costs. Here we study the first case, i.e. with equal control input costs. From the simulation results shown in Figure 4.10, the following observations can be made.

- In the open loop, the vehicle yaw rate doesn't return to zero after the SWD cycle is over. This indicates that the vehicle is spinning out of control. With the proposed controller, the vehicle yaw rate tracks its reference and therefore it comes back to zero after the SWD cycle is over.
- In the open loop, when $t > 4$ s, the vehicle lateral acceleration retains almost the same value as compared to the second half of the SWD cycle. This is undesired as the steering wheel angle is zero when $t > 4$ s (see Figure 4.9). With the proposed controller, in addition to attaining same lateral acceleration as open loop, it comes back to zero after the SWD cycle is over.

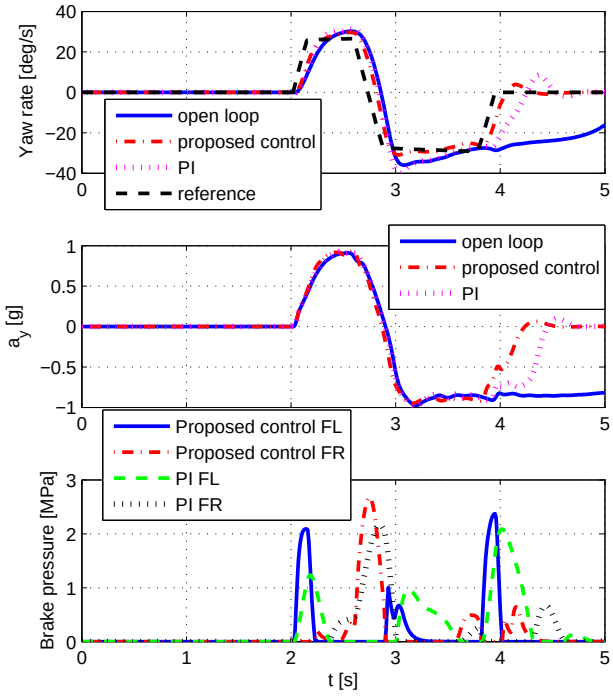

Figure 4.10: Vehicle yaw rate, lateral acceleration a_y and brake inputs during the SWD maneuver at 80 kmph.

- The PI based yaw rate controller is able to stabilize the vehicle. However, the yaw rate has an overshoot of the order 8 deg/s once the SWD is over. Whereas for the same quadratic control input cost i.e. for the same control effort, the proposed yaw rate controller stabilizes the vehicle for a lower yaw rate overshoot of the order 4 deg/s. In addition, the acceleration profile of the PI based yaw rate controller has a delay of the order 0.5 s in converging to zero once the steering input is zero after $t = 4$ s, whereas with the proposed controller, the acceleration converges to zero faster.

Therefore it is seen that the proposed controller is able to keep the vehicle stable during the SWD maneuver considered and it performs better than the PI controller with the same control effort. The front axle brake pressures generated by both the controllers are shown in the bottom plot of Figure 4.10.

4.4.3. ROBUSTNESS TO VEHICLE SPEED

Now to study the effect of different vehicle speeds, the vehicle is simulated with the same SWD cycle but for different vehicle speeds. From the results shown in Figure 4.11, the following observations can be made.

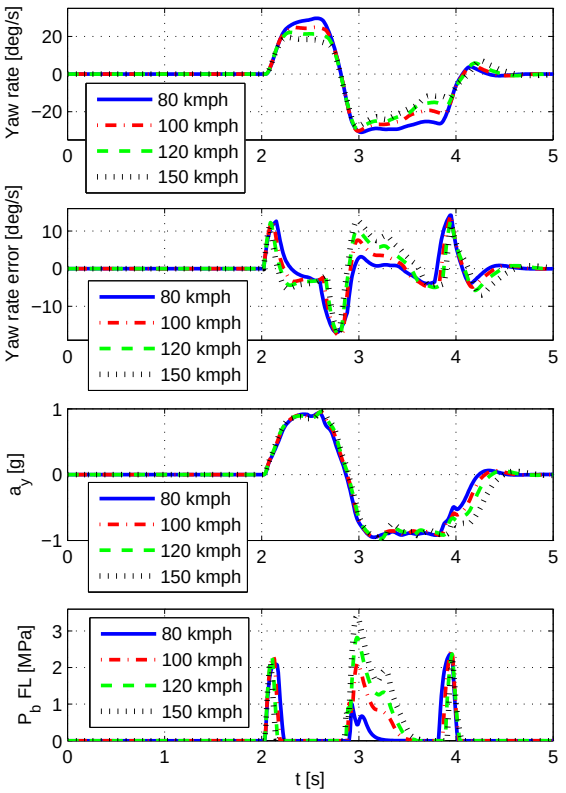

Figure 4.11: Vehicle yaw rate, yaw rate error, lateral acceleration a_y and front left brake input during the SWD maneuver at different speeds.

- Although the yaw rate error increases with increasing vehicle speed (around $t = 3$ s), the controller maintains stable yaw rate behavior. This is because the controller design and controller gain do not depend on the vehicle speed. On the other hand, the PI based yaw rate controller is not robust to different vehicle speeds as shown in Figure 4.12. It needs to be retuned or gain scheduled depending on the speed.

- In the results shown in Figure 4.11, the magnitude of yaw rate decreases as the vehicle speed increases. This is because the maximum yaw rate reference $\dot{\psi}_{max}$ is inversely proportional to the vehicle speed as seen in (4.3). This comes from the vehicle kinematic relationship $a_y = \dot{v}_y + v_x\dot{\psi}$ i.e. for a given maximum lateral acceleration $a_{y_{max}}$ allowed by the road-tyre friction, maximum yaw rate $\dot{\psi}_{max}$ and longitudinal vehicle velocity v_x are inversely proportional to each other [36].

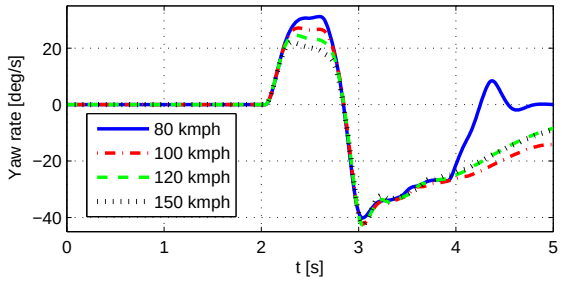

Figure 4.12: Closed loop vehicle yaw rate with the PI based yaw rate controller during the SWD maneuver at different vehicle speeds.

- The lateral acceleration profiles in Figure 4.11 follow the steering profile in Figure 4.9. In addition, the maximum lateral acceleration does not decrease for higher vehicle speeds. However the settling time of a_y after the SWD cycle ends increases as the vehicle speed increases.
- As the vehicle speed increases, the brake pressure applied by the controller increases in the second half of the SWD cycle.

Therefore it is seen that the proposed controller is robust to the vehicle speed range considered. In addition, the controller gain does not depend on the vehicle speed. This removes the need for vehicle speed based gain scheduled controller, which is usually required with the PI based yaw rate control and other lateral dynamics control designs where the vehicle model matrices are functions of vehicle speed, for example the control design in [32] and the control design in Chapter 3. This makes the proposed controller easier to implement and tune on a vehicle.

4.4.4. ROBUSTNESS TO MEASUREMENT NOISE

As the controller uses vehicle speed, yaw rate and force measurements to compute the yaw rate reference and control input, its robustness to measurement noise is studied next. In order to consider noise in the vehicle speed, yaw rate and force measurements, they are corrupted with uniformly distributed random signal with peak to peak amplitude 10 km/h, 5 deg/s and 500 N respectively (See Section 6.2.1 for more details on the force sensor noise). These levels of noise realistically represent the noise affecting the sensor employed in a test vehicle [55–57].

The steering wheel profile of the applied SWD cycle is the same as Figure 4.9 and the vehicle has an initial speed of 80 kmph. From the simulation results shown in Figure 4.13, it is observed that the proposed yaw rate controller is robust to measurement noise in the considered maneuver, whereas the open loop case is unstable.

4.5. CONCLUSIONS

IN this chapter, how tyre force measurements can benefit the yaw rate control problem using braking actuators is studied. A novel computationally inexpensive feedback lin-

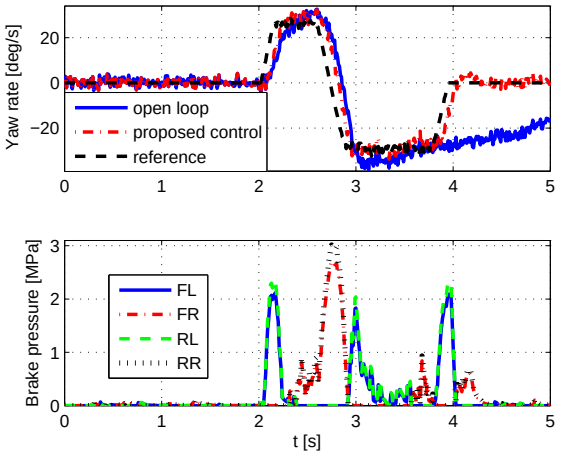

Figure 4.13: Yaw rate and brake inputs during the SWD maneuver at 80 kmph with measurement noise.

earization based yaw rate controller using tyre force measurements is studied in this direction. The proposed yaw rate controller does not employ a tyre model unlike most of the yaw rate controllers in the literature. It uses tyre force measurements and a non-linear yaw rate model. As a result, the control design and control gain do not directly depend upon the vehicle speed and vehicle sideslip. Overall, with the availability of tyre force measurements, the proposed yaw rate control offers a robust and computationally inexpensive alternative in cars with braking actuators.

The proposed controller is studied in split-μ and SWD simulations using Simulink and CarSim environment. During both simulations, it is observed that the vehicle is stable in closed loop, whereas the vehicle becomes unstable in open loop. The controller is also found to be robust to vehicle speed and to measurement noise in vehicle speed, yaw rate and force measurements. However as the vehicle speed increases, the lateral acceleration has higher settling time.

The road-tyre friction can be used to estimate the physical limits of the vehicle. In this chapter, the yaw rate reference limit defined in (4.3) is calculated with a road-tyre friction value of 1. This can limit the controller robustness to different friction values because the controller performance can degrade if it does not know the physical limits of the vehicle. A road-tyre friction estimator can possibly address this issue. This is studied in the next chapter.

5

FRICTION ESTIMATION DURING COMBINED TYRE SLIP

5.1. INTRODUCTION

ROAD-TYRE friction is an important variable for the TUCC proposed in Chapter 3 and the yaw rate controller proposed in Chapter 4. It is also important for other active safety systems such as Anti-lock Braking System (ABS), Traction Control System (TCS) and Adaptive Cruise Control (ACC). It is defined as the maximum force the tyre can exert, normalized by the vertical load. Availability of road-tyre friction helps in estimating the physical limits of the vehicle, and therefore, may improve the active safety systems.

In this chapter, a road-tyre friction estimator considering combined tyre slip situations is designed, simulated and validated. The friction estimator design is motivated by its importance in yaw rate control as accurate friction estimation can improve the controller performance. The proposed estimator is therefore designed and integrated with a yaw rate controller and studied in closed loop. The estimator uses tyre force measurements and does not rely on parameterized tyre model. The tyre force measurements benefit the estimator mainly because of the uncertainties and nonlinearities of the tyre force characteristics which depend on factors like temperature, vertical load, road friction, etc. The proposed estimator uses tyre slip and tyre force representations where the longitudinal and lateral tyre slips and forces are combined into a single tyre slip and tyre force values. This representation makes the method effective during pure longitudinal dynamics, pure lateral dynamics and the combined case. In addition, individual tyre-road friction estimation is possible with the proposed estimator and a computationally inexpensive algorithm, suitable for real-time implementation, is used to estimate the friction. The estimator is studied in a simulator environment during braking, cornering and the combined case. Further, the estimator is simulated in closed loop with a yaw rate controller to study whether the estimator improves vehicle safety. Finally the estimator

Parts of this chapter have been published in Mechatronics [59].

is validated using test data from several maneuvers performed on a BMW test vehicle instrumented with Load Sensing Bearing (LSB) technology.

Road-tyre friction estimators can be categorized depending on the level of required tyre dynamics excitation. In the first category, the estimator tries to extract some information about the tyre characteristics during low levels of tyre dynamics excitation and this information is extrapolated to estimate the road-tyre friction [23, 45, 46]. The second category estimates the friction when the peak tyre force is crossed. The proposed method belongs to the second category. The advantage of the first category is that it does not require the car to drive beyond the peak tyre force and the disadvantage is that the estimate is guessed based on the tyre model. The friction estimation is a form of extrapolation that heavily depends on the tyre model used. The advantage of the second type is a precise knowledge of the peak friction, but the car needs to drive beyond the peak. This means that when the tyres are far from their saturation limit, the friction estimate may not be current. Therefore, it is crucial to make sure that the lateral dynamics control is robust to this condition. For this reason, the proposed road-tyre friction estimator is designed and integrated with the yaw rate controller in Chapter 4 with the objective of improving the controller performance.

The proposed road-tyre friction estimator uses tyre force measurements. As road-tyre friction is reflected highly on tyre forces and there are not many studies present in the literature, this approach deserves attention. In Chapter 3, 4 and 6, lateral vehicle dynamics control and vehicle sideslip estimation are studied based on tyre force measurements. This chapter studies tyre force based friction estimation as it is important to implement and test the lateral vehicle dynamics control proposed in Chapter 3 and to improve the performance of the yaw rate controller proposed in Chapter 4. The following are the main contributions of this chapter.

- A road-tyre friction estimator is proposed considering combined slip situations. Therefore the estimator is effective during longitudinal, lateral and combined slip situations. As the estimator is applied to individual tyres, it is possible to estimate road-tyre friction of each of the tyres.

- The proposed estimator uses tyre force measurements. Therefore the estimator is robust to changes in the tyre model due to tyre wear, temperature and other factors such as vertical load, camber and toe angles.

- The estimator is also validated using test data from several maneuvers performed on a BMW test vehicle instrumented with LSB technology.

This chapter is structured as follows. In Section 5.2, the yaw rate control problem is introduced and the importance of road-tyre friction estimation in yaw rate control is discussed. Section 5.3 introduces the idea to use combined tyre slip and combined tyre force for friction estimation. The tyre slip estimation is also explained here. In Section 5.4, the friction estimation algorithm is described in detail. The proposed estimator is studied using a simulator environment as well as test data in Section 5.5. Section 5.6 concludes the findings and discusses future work directions.

5.2. YAW RATE CONTROL AND FRICTION ESTIMATION

THE importance of road-tyre friction estimation for yaw rate control is discussed in this section. Typically, a yaw rate controller corrects vehicle yaw rate error by applying feedback control using steering or braking actuators [36, 43]. The yaw rate error is calculated as the difference between the measured vehicle yaw rate and its reference from a yaw rate reference model. The yaw rate controller considered in this chapter uses braking actuators and tyre force measurements, and is proposed in Chapter 4. As described in Chapter 4, the controller receives the yaw rate reference from the following reference model [36, 43, 58].

$$\dot{\psi}_{ref} = \frac{(V/L)\delta}{1+\frac{\eta}{gL}V^2}, \tag{5.1}$$

$$\max(|\dot{\psi}_{ref}|) = \frac{\mu g}{V}. \tag{5.2}$$

Here $\dot{\psi}_{ref}$ is the yaw rate reference, V is the vehicle speed, L is the distance between the front and rear axles, δ is the steering angle, η is the desired understeer coefficient, g is earth's gravity and μ is the road-tyre friction. In order to understand the effect of an incorrect friction estimate, consider the following simplified lateral vehicle dynamics.

$$m\left(u_{CoG}\dot{\psi}+\dot{v}_{CoG}\right) = F_{yF}+F_{yR}, \text{ i.e.,} \tag{5.3}$$

$$mu_{CoG}\left(\dot{\psi}+\dot{\beta}\right) = F_{yF}+F_{yR}. \tag{5.4}$$

Assuming $u_{CoG} \approx V$ gives,

$$mV\left(\dot{\psi}+\dot{\beta}\right) = F_{yF}+F_{yR}. \tag{5.5}$$

Here m is the vehicle mass, u_{CoG} is the longitudinal velocity at the vehicle center of gravity (CoG), $\dot{\psi}$ is the vehicle yaw rate, v_{CoG} is the lateral velocity at the vehicle CoG, F_{yF} is the front axle lateral force, F_{yR} is the rear axle lateral force and β is the vehicle sideslip. When the vehicle is at its physical limits of lateral acceleration, (5.5) is rewritten as follows.

$$mV\left(\dot{\psi}+\dot{\beta}\right) = m\mu g, \text{ i.e.,} \tag{5.6}$$

$$\left(\dot{\psi}+\dot{\beta}\right) = \frac{\mu g}{V}. \tag{5.7}$$

Equation (5.7) represents the approximate lateral vehicle dynamics when the vehicle is at its physical limits of lateral acceleration. Now comparing the dynamics in (5.7) with the yaw rate reference maximum in (5.2), it is understood that the yaw rate reference maximum in (5.2) is a special case of the dynamics in (5.7) with $\dot{\beta} = 0$. Now, if the road-tyre friction estimate is not available, the product μg in (5.2) might be inaccurate, resulting in incorrect saturation limits of the yaw rate reference model. This could lead

to a very high reference yaw rate. According to (5.7), very high vehicle yaw rate $\dot{\psi}$ can cause non-zero vehicle sideslip derivative $\dot{\beta}$, which in turn could make the vehicle unstable [36] as vehicle sideslip β may reach high values. This issue is not restricted to the controller in Chapter 4, all yaw rate based controllers have to deal with the fact that the reference generation depends on the friction. The availability of friction estimate can prevent this from happening, thereby improving the yaw rate controller performance. This is further studied in Section 5.5 with the friction estimator proposed in Section 5.4 and the yaw rate controller proposed in Chapter 4.

5.3. COMBINED TYRE SLIP AND COMBINED TYRE FORCE

THIS section introduces combined tyre slip and combined tyre force as they are used in Section 5.4 to design the friction estimator. Typically the tyre sideslip is mentioned in degrees, whereas the longitudinal slip as a ratio in the range $[0,1]$. This representation makes it difficult in quantifying the combined tyre slip situations using a single slip value. If an alternative tyre sideslip representation from the literature [65] is used, where the sideslip is also a number in the range $[0,1]$, the combined slip situations can be quantified using a single value. Consider the following definitions.

$$\lambda_x = \frac{u_t - wr}{V_t}, \tag{5.8}$$

$$\lambda_y = \frac{v_t}{V_t}, \text{and} \tag{5.9}$$

$$\lambda = \sqrt{\lambda_x^2 + \lambda_y^2}. \tag{5.10}$$

Here λ_x and λ_y are the longitudinal and lateral tyre slips, u_t and v_t are the longitudinal and lateral tyre velocities, w is the angular tyre velocity, r is the effective tyre radius, $V_t = \sqrt{u_t^2 + v_t^2}$ is the tyre speed and λ is the combined tyre slip. Then the combined tyre slip λ is a number in the range $[0,1]$ and it can quantify the combined tyre slip situations. λ is estimated based on equations (5.8)-(5.10). In (5.8), the longitudinal velocity measurement u_t or its estimate is assumed to be available. It can be estimated using a weigthed average of the four wheel measurements, as usually done in ABS systems [63].

The lateral tyre slip λ_y in (5.9) is rewritten as follows.

$$\lambda_y = \frac{v_t}{V_t} = \frac{u_t\delta - \left(v_{CoG} + a\dot{\psi}\right)\left(1 - \frac{\delta^2}{2}\right)}{V_t}. \tag{5.11}$$

Here a is the distance between the CoG and the front axle, and δ is the steering angle. The CoG lateral velocity v_{CoG} is estimated using the vehicle sideslip estimator proposed in Chapter 6. The vehicle sideslip β is defined as the angle between the vehicle longitudinal axis and the vehicle velocity vector. It is defined mathematically by $\beta \approx \frac{v_{CoG}}{u_{CoG}}$. The vehicle sideslip estimator uses tyre force measurements and is a Kalman filter based on the vehicle kinematic model. To see more details about the vehicle sideslip estimator, please see Chapter 6.

Using equations (5.8), (5.10) and (5.11), the combined tyre slip λ is estimated. The combined tyre force F_N is defined as follows.

$$F_N(\lambda,\mu) = \frac{\sqrt{F_x^2 + F_y^2}}{F_z}. \tag{5.12}$$

Here F_x, F_y and F_z are the longitudinal, lateral and vertical tyre forces and μ is the road-tyre friction to be estimated. Figure 5.1 shows the combined tyre slip λ versus combined tyre force F_N characteristics during different driving situations using a CarSim multi-body vehicle model with 15 DOF and a nonlinear tyre model. The nonlinear tyre model consists of tables relating the longitudinal and lateral forces (measured in a laboratory or test vehicle) to the tyre states in terms of slip, load, camber and toe angles and road friction [66].

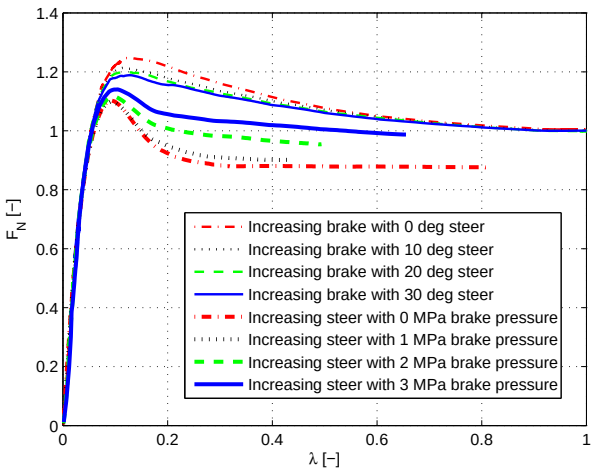

Figure 5.1: Combined tyre slip λ versus combined tyre force F_N characteristics during different driving situations.

From Figure 5.1, it can be observed that by using the definition of the combined slip and force, the multidimensional nature of the tyre can be collapsed onto a single dimension. This simplifies the road friction estimation problem. It is also worth noting that depending on the driving condition, the maximum force and position of the peak vary slightly. This is a consequence of the elliptical nature of the tyre friction envelope. This variability is small enough to be neglected in the design of the method. It will be later shown that this variability does not limit the applicability of the methods. The combined tyre slip and combined tyre force are used to estimate the road-tyre friction. The benefit of the combined tyre slip based approach is that it considers realistic driving situations, which might involve longitudinal as well as lateral dynamics.

5.4. ROAD-TYRE FRICTION ESTIMATOR

THE road-tyre friction estimator is explained in this section. The estimator algorithm is based on a feature of the combined tyre slip versus combined tyre force characteristics. In the characteristics shown in Figure 5.1, for every case, there is a peak combined force after which the combined force decreases with further increment in the combined slip. The main idea of the proposed estimator is to capture the combined tyre force whenever the tyre passes through the peak. The estimator detects a change of sign of the derivative of the combined tyre force with respect to the combined slip. This is obtained through the intermediate step of finding the time derivative of the combined slip and force as shown in Figure 5.2.

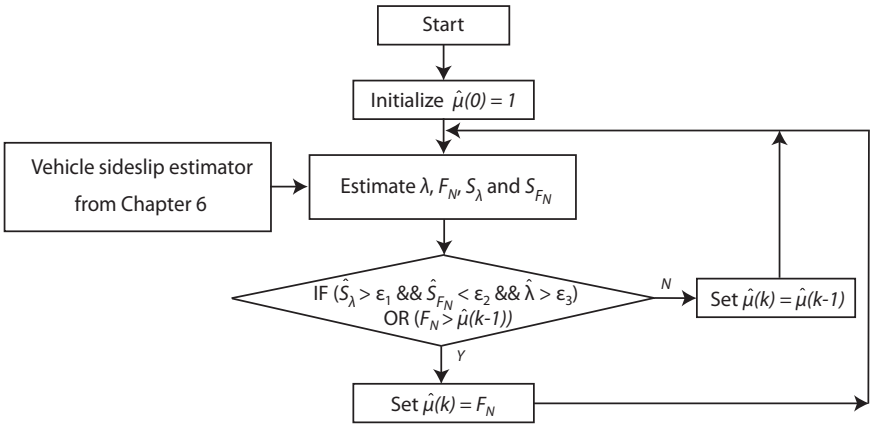

Figure 5.2: The road-tyre friction estimation algorithm.

The estimation algorithm is shown in Figure 5.2. Here $\hat{S}_\lambda$ is the time derivative estimate of the combined slip, $\hat{S}_{F_N}$ is the time derivative estimate of the combined tyre force, ϵ_1 is a positive number, ϵ_2 is a number close to zero and ϵ_3 is a positive number. ϵ_1, ϵ_2 and ϵ_3 are tuned during the implementation depending on the noise levels in $\hat{S}_\lambda$, $\hat{S}_{F_N}$ and $\hat{\lambda}$. The time derivative estimates $\hat{S}_\lambda$ and $\hat{S}_{F_N}$ are calculated as shown in Section 5.4.1 using the Recursive Least Square (RLS) algorithm [64].

The friction estimation algorithm initializes with $\hat{\mu}(0) = 1$ when it is turned on for the first time. Next, the algorithm estimates λ, F_N, S_λ and S_{F_N}. This block receives the vehicle sideslip estimate $\hat{\beta}$ from the estimator proposed in Chapter 6. Then the friction estimate $\hat{\mu}$ is updated to the present normalized combined force F_N if any of the following conditions is true.

- If $\hat{S}_\lambda$ is greater than the positive number ϵ_1, $\hat{S}_{F_N}$ is less than the small value ϵ_2 and $\hat{\lambda}$ is greater than the positive number ϵ_3. From Figure 5.1, it is understood that this condition is true when the normalized combined tyre force is close to its maximum.
- If the friction estimate from the previous sample time $\hat{\mu}(k-1)$ is less than the present combined tyre force F_N.

If none of the above conditions is true, the friction estimate retains its previous value, i.e. $\hat{\mu}(k) = \hat{\mu}(k-1)$.

As combined slip situations are considered, the estimator is effective during longitudinal as well as lateral dynamics. It is also robust to factors such as temperature, tyre wear and tyre pressure as the estimator does not use parameterized mathematical tyre models such as Magic formula, Burckhardt model or Dugoff model. In addition, the estimator is computationally inexpensive and it is implemented on individual tyres. Therefore, road-tyre friction of each tyre can be estimated.

5.4.1. ESTIMATION OF S_{F_N} AND S_λ

The time derivatives of the combined tyre force and slip, S_{F_N} and S_λ, are estimated using the RLS algorithm [64] with sampling time 0.01 s or a sampling frenquency of 100 Hz, higher than the approximate lateral vehicle dynamics bandwidth of 10 Hz. The RLS algorithm estimates the parameter vector θ in the following linear system model.

$$y(k) = \phi^T(k)\theta + e(k) \tag{5.13}$$

Here $y(k) \in R^{1\times 1}$ and $\phi(k) \in R^{n\times 1}$ are the measured variables, $\theta \in R^{n\times 1}$ is the parameter vector to be estimated and $e(k) \in R^{1\times 1}$ represents the modeling error and noise in the system. Figure 5.3 shows the block diagram of the RLS algorithm.

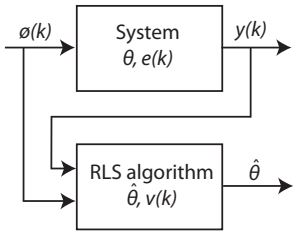

Figure 5.3: Block diagram of the RLS algorithm.

The RLS algorithm estimates $\hat{\theta}$ by minimizing the sum of squares of the error $v(k) = y(k) - \phi^T(k)\hat{\theta}$ recursively. Because of its recursive nature, it is computationally cheaper than solving the Least Square solution in every sample instant. The RLS algorithm is initialized with the following Least Square solution from the first N samples.

$$P_{init} = [\Phi^T\Phi]^{-1}, \tag{5.14}$$

$$\hat{\theta}_{init} = P_{init}\Phi^T Y. \tag{5.15}$$

Here $\Phi \in R^{N\times n}$ is $[\phi(1)\ \phi(2)\ ...\ \phi(N)]^T$ and $Y \in R^{N\times 1}$ is $[y(1)\ y(2)\ ...\ y(N)]^T$. Then the RLS update of the estimate $\hat{\theta}$ is obtained using the following equations.

$$P(k) = \frac{1}{f}\left(P(k-1) - \frac{P(k-1)\phi(k)\phi^T(k)P(k-1)}{f + \phi^T(k)P(k-1)\phi(k)}\right), \tag{5.16}$$

$$\hat{\theta}(k) = \hat{\theta}(k-1) + P(k)\phi(k)\left(y(k) - \phi^T(k)\hat{\theta}(k-1)\right). \tag{5.17}$$

Here P is the covariance of the estimate and f is the forgetting factor to reduce the effect of old data on the estimate. The forgetting factor also affects the estimator response time. Lower forgetting factor results in lower estimator response time, however it might result in higher estimate noise. Higher estimate noise in $\hat{S}_{F_N}$ and $\hat{S}_\lambda$ can result in false peak friction detection. Therefore there is a trade-off while selecting the forgetting factor.

The RLS algorithm for $\hat{S}_{F_N}$ is discussed next. The time derivative of the combined tyre force, S_{F_N}, is estimated by finding the slope of F_N with respect to time k using the RLS algorithm. The RLS algorithm is initiated with the Least Square solution of the first 25 samples using (5.14) and (5.15) with $\phi(k) = k$ and $y(k) = F_N(k)$. Then the RLS updates in (5.16) and (5.17) are performed in every sample instant to obtain the estimate $\hat{\theta}(k) = \hat{S}_{F_N}(k)$.

The same RLS algorithm with $\phi(k) = k$ and $y(k) = \lambda(k)$ is used to estimate the time derivative of the combined tyre slip S_λ.

5.4.2. ESTIMATOR TUNING

As shown in the estimator and RLS algorithms in Figure 5.2 and Section 5.4.1, there are four parameters in the algorithm, ϵ_1, ϵ_2, ϵ_3 and f. They are tuned in simulation. Figure 5.4 shows the effect of different values of ϵ_1 and ϵ_2 during combined slip maneuver simulations with 40 deg steer. The vehicle is initialized with a speed of 150 km/h and brake pressure is applied from $t = 1$.

As seen in Figure 5.4, for $\epsilon_1 = 0.13$, the estimator is able to capture the peak friction. As explained in Section 5.4, if $\hat{S}_\lambda$ is greater than the positive number ϵ_1, $\hat{S}_{F_N}$ is less than the small value ϵ_2 and $\hat{\lambda}$ is greater than the positive number ϵ_3, the friction estimate $\hat{\mu}$ is updated to the present normalized combined force F_N. Therefore ϵ_1 is used to make sure that the combined slip is increasing when the friction estimate is updated. Ideally, this means ϵ_1 can be 0 but then the noise in $\hat{S}_\lambda$ might cause the estimator to update when the real value of S_λ is negative (or the combined slip is decreasing) but its estimate $\hat{S}_\lambda$ is greater than $\epsilon_1 = 0$ due to the considered noise level. To avoid this, ϵ_1 should be a positive number. It is observed that for $\epsilon_1 > 0.13$, the estimator is not able to capture the peak friction, see the case with $\epsilon_1 = 0.20$ for example. As ϵ_1 is decreased from 0.13 to 0.10 and 0.05, the delay in capturing the peak is also reduced. However, for $\epsilon_1 < 0.05$, there is no further reduction. In addition, further reduction of ϵ_1 might cause the estimator to capture incorrect friction due to the noise in the RLS estimate $\hat{S}_\lambda$ as discussed before. Therefore, ϵ_1 is chosen as 0.05. The parameter ϵ_2 is initialized with 0.50 and is decreased until $\epsilon_2 = 0.02$ where the estimator no more captures non-peak combined force values as the peak friction. If ϵ_2 is further reduced, there is delay in the estimation as seen in the case with $\epsilon_2 = -0.10$. Similary ϵ_3 and f are tuned to 0.05 and 0.7 respectively.

Ideally ϵ_1, ϵ_2 and ϵ_3 can be assigned zero. However, they are tuned to non-zero values as described above to increase the estimator robustness to noise in the RLS estimates $\hat{S}_\lambda$ and $\hat{S}_{F_N}$, and λ, caused by the sensor noise. Otherwise, the estimator might capture incorrect values of F_N as the peak friction as shown in Figure 5.5. Higher sensor noise requires higher values for ϵ_1 and ϵ_3, and this can result in higher peak friction detection time.

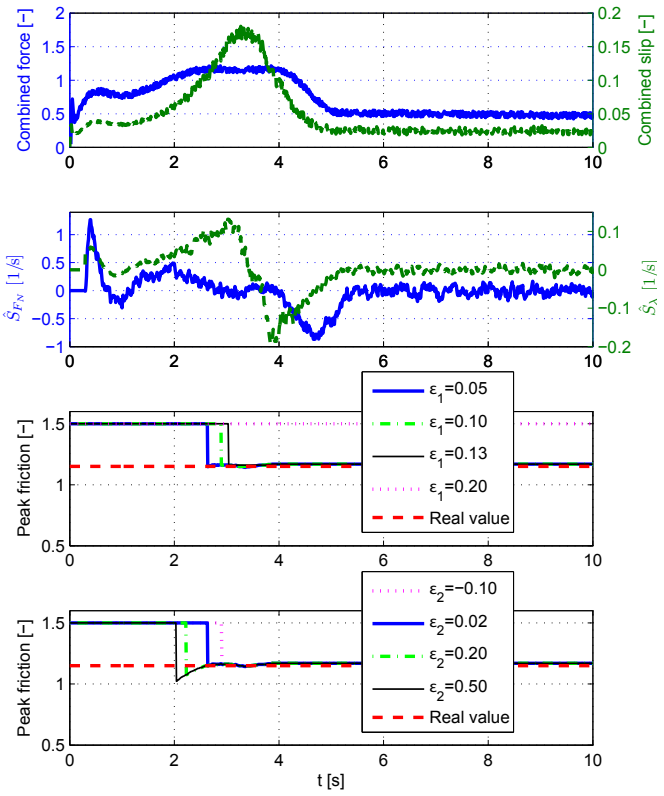

Figure 5.4: Effect of different values of ϵ_1 and ϵ_2 during combined slip maneuver simulations with 40 deg steer.

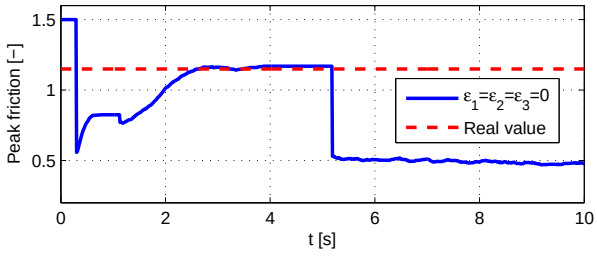

Figure 5.5: Effect of $\{\epsilon_1, \epsilon_2, \epsilon_3\} = \{0, 0, 0\}$ during combined slip maneuver simulations with 40 deg steer.

5.5. RESULTS

The road-tyre friction estimator is designed and studied using simulation as well as experimental data. In the simulation study, the estimator is studied using Simulink and

CarSim simulation package. The CarSim package provides a multi-body vehicle simulator with 15 DOF and a nonlinear tyre model [18]. The vehicle sideslip estimator from Chapter 6, which is used by the proposed friction estimator, is also implemented in Simulink. The multi-body vehicle model from the CarSim package is used as the vehicle model. The estimator is also validated using experimental data from a test vehicle. It should be noted that the simulation studies as well as experimental data based studies are done for the front left tyre of the vehicle. The same estimator can be applied to any of the vehicle tyres.

The simulation study is further divided into two categories, open loop and closed loop. In the open loop case, the estimator is studied without the yaw rate controller discussed in Section 5.2. The estimator is simulated in longitudinal, lateral and combined slip maneuvers. In order to consider noise in longitudinal velocity and force measurements, they are corrupted with uniformly distributed random signal with peak to peak amplitude 10 km/h and 500 N respectively (See Section 6.2.1 for more details on the force sensor noise). These levels of noise realistically represent the noise affecting the sensor employed in the experimental setup [55–57]. The objective here is to study whether the road-tyre friction can be estimated real-time during different driving situations. A μ jump scenario is also considered to better assess the dynamic (or transient) properties of the estimator.

In the closed loop case, the estimator is simulated with the yaw rate controller on and the vehicle is pushed outside its stability limits to study whether the friction estimator improves the controller performance.

Finally, the estimator is valided with test data from various maneuvers performed on a BMW test vehicle equipped with LSB technology.

5.5.1. OPEN LOOP TESTS

In this section, the estimator is studied without the yaw rate controller discussed in Section 5.2. First, a steering maneuver is considered. In this simulation, the vehicle has a constant speed of 80 km/h and steering is applied from $t = 1$ s as shown in Figure 5.6. The simulation results are also shown in Figure 5.6. The estimator is initialized with a friction estimate of 1.5. From the results, it is observed that the tyre force reaches its maximum around $t = 3$ s and the estimator is able to recognize and capture this. Therefore, the estimator updates the friction estimate and it is accurate compared to the real friction value. It should be noted that the update just after $t = 4$ s is caused by the noise in the RLS estimate $\hat{S}_{F_N}$. This can be avoided if the estimator is tuned only for this maneuver. However, this is the best setting for the tuned parameters considering all the situations studied in this chapter. In addition, the error caused by this update is acceptable as it does not affect the yaw rate controller as would be seen in the closed loop studies.

The next case studied is a braking maneuver while driving straight. In this simulation, the vehicle is initialized with a speed of 150 km/h and braking is applied from $t = 1$ s as shown in Figure 5.7. From the results shown in Figure 5.7, it is observed that the estimator is able to recognize and capture the road-tyre friction accurately. It should be noted that there is a slight difference in the friction values in longitudinal and lateral directions because of the tyre characteristics being elliptical.

So far, pure braking and steering maneuvers are discussed. Next, a combined slip

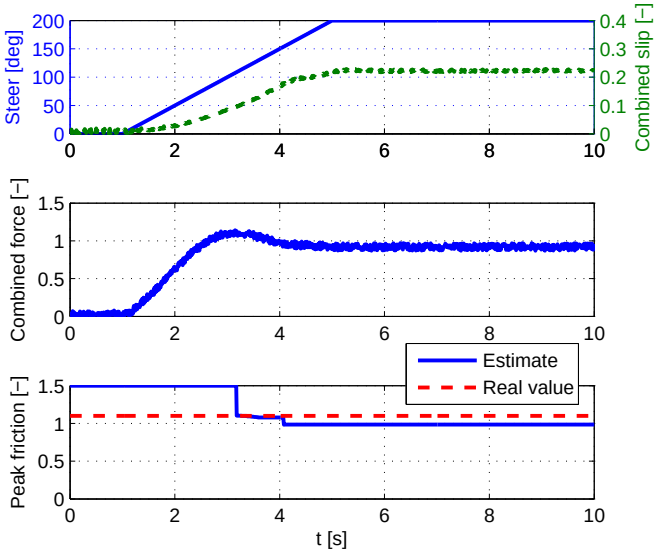

Figure 5.6: Simulation study during a steering maneuver at 80 km/h.

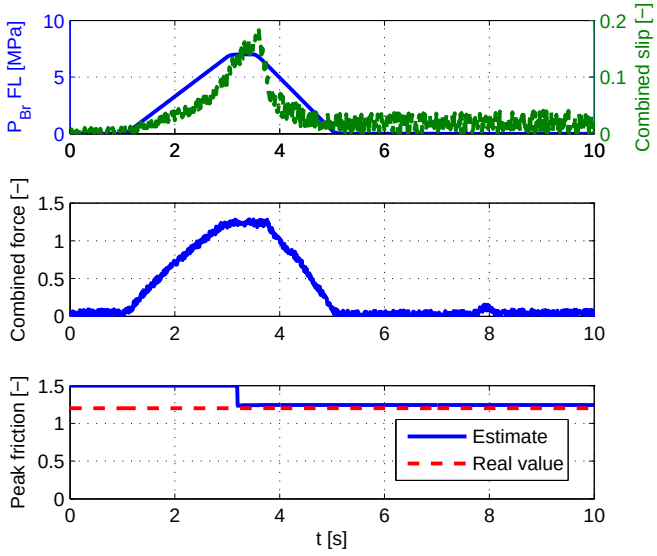

Figure 5.7: Simulation study during a braking maneuver from 150 km/h. Steering angle is zero.

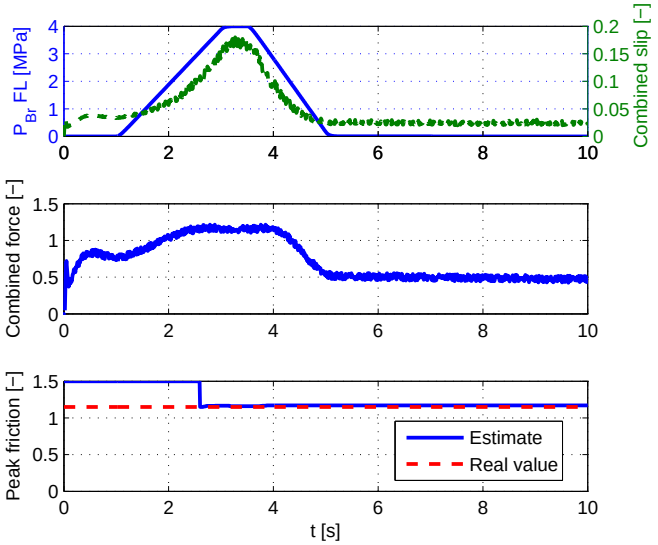

Figure 5.8: Simulation results during a combined slip maneuver with 40 deg steer.

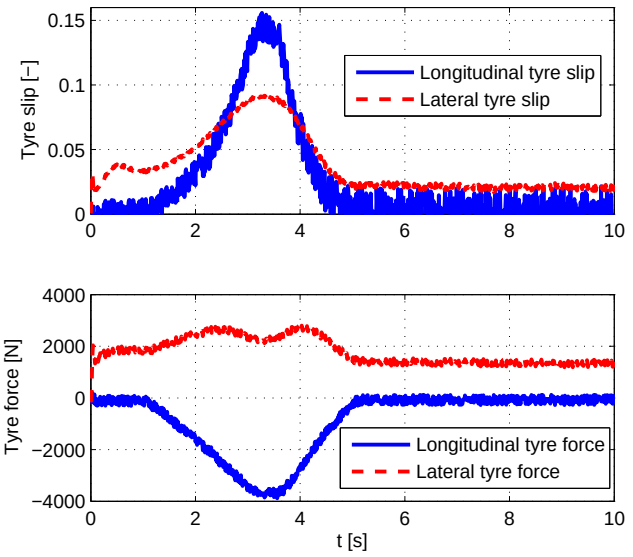

Figure 5.9: Tyre slips and forces during a combined slip maneuver with 40 deg steer.

situation is considered where the vehicle experiences braking as well as steering. The vehicle is initialized with a speed of 150 km/h and a constant steering angle of 40 deg is

applied throughout the simulation. In addition, brake pressure is applied from $t = 1$ s as shown in Figure 5.8. From the results shown in Figure 5.8, it is observed that the friction estimator is effective in the combined slip situation. Figure 5.9 shows the longitudinal and lateral tyre slips and tyre forces during the combined slip maneuver.

The next simulation studies a scenario where the friction changes during a steering maneuver. The road-tyre friction undergoes a μ jump where it changes from 1 to 0.7 at $t = 7$ s. From the results shown in Figure 5.10, it is seen that the estimator is able to capture the change in friction within 0.25 s. This is an important information for active safety systems, especially if a similar μ jump happens during a critical maneuver.

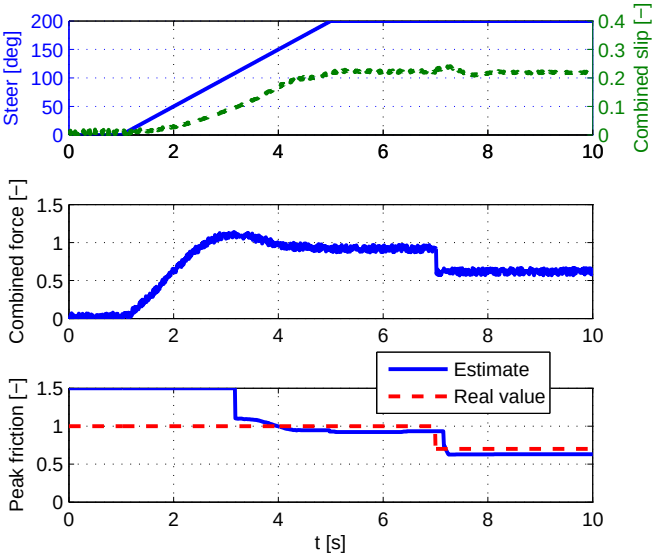

Figure 5.10: Simulation study during a steering maneuver with μ jump at $t = 7$ s.

5.5.2. CLOSED LOOP TESTS

In this section, the estimator is studied with the yaw rate controller from Chapter 4 to study how the friction estimator affects the controller performance, as described in Section 5.2. The block diagram of the closed loop tests is shown in Figure 5.11. Although the proposed friction estimator offers an accurate friction estimate, the car needs to drive beyond the peak. This means that when the tyres are far from their saturation limit, the friction estimate may not be current. Therefore, it is crucial to make sure that the yaw rate controller is robust to this condition.

The yaw rate controller from Chapter 4 is implemented in Simulink to study the friction estimator in closed loop. The vehicle is simulated with a Sine with Dwell (SWD) maneuver. The applied SWD steering profile is shown in the top plot of Figure 5.12 and the vehicle is initialized with a speed of 80 km/h on a surface with $\mu = 1$. The first simu-

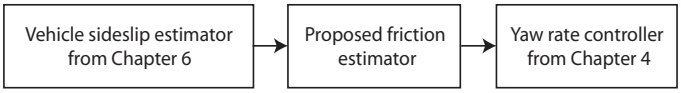

Figure 5.11: The block diagram of the closed loop tests.

lation study is to demonstrate that the yaw rate controller is able to stabilize the vehicle for a SWD maneuver which makes the vehicle unstable in open loop. The closed loop case with the proposed friction estimator is compared with the closed loop case without friction estimation. In the closed loop case without friction estimation, the yaw rate reference model in (5.1-5.2) is calculated with the default friction value $\mu = 1$. The simulation results are shown in Figure 5.12.

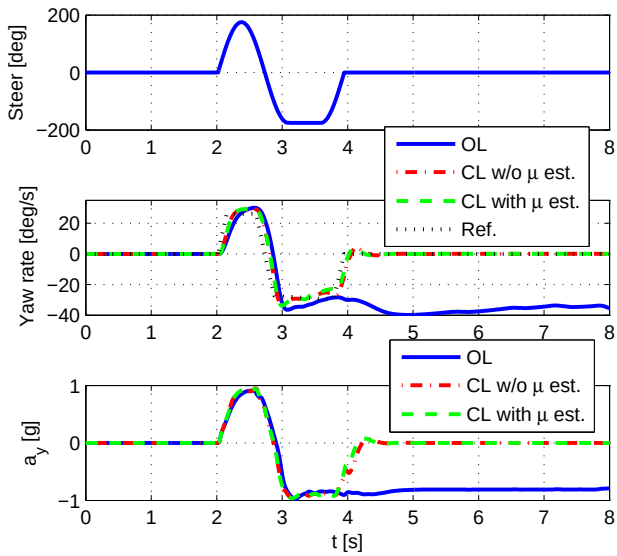

Figure 5.12: Simulation results during a SWD maneuver with $\mu = 1$. Here OL and CL mean Open and Closed Loop.

In the open loop case, the vehicle is unstable as seen in the yaw rate and lateral acceleration plots. In the closed loop cases, the vehicle is stable with and without friction estimation and there are no major differences in the the yaw rates and lateral accelerations. This is because the road-tyre friction is $\mu = 1$ for this simulation and for the case without friction estimation, the default friction value of the yaw rate reference model in (5.2) is 1. This is expected as the objective of this simulation study is to demonstrate that the yaw rate controller is able to stabilize the vehicle for a SWD maneuver which makes the vehicle unstable in open loop. Figure 5.13 shows the control input generated by the controller with friction estimation.

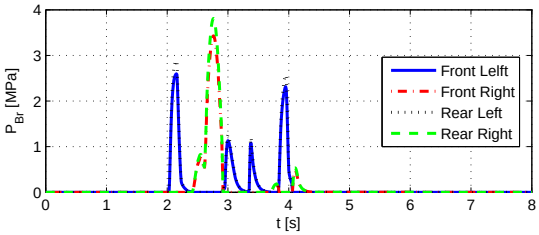

Figure 5.13: Control input generated by the controller with μ estimation during a SWD maneuver with $\mu = 1$.

Next, the vehicle is simulated with an initial friction value of 0.7 and the friction changes to 0.3 and 0.2 during the SWD maneuver as shown in the bottom plot of Figure 5.14. The steering profile is shown in the top plot of Figure 5.14. The vehicle is initialized with a speed of 80 km/h. In the closed loop case without friction estimation, the yaw

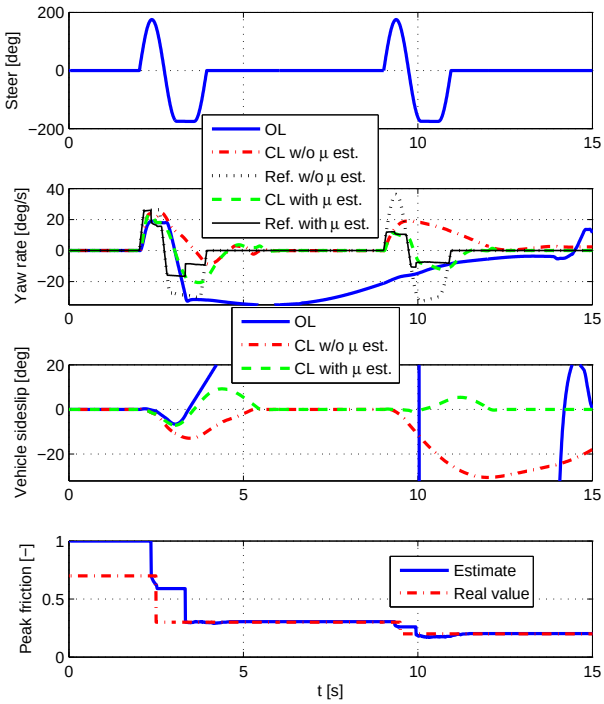

Figure 5.14: Simulation results during a SWD maneuver with μ jump from 0.7 to 0.3 and 0.3 to 0.2.

rate reference limits in (5.2) is calculated with $\mu = 1$. In the closed loop case with friction estimation, the estimator is initiated with $\mu = 1$ as shown in the bottom plot of Figure

5.14. From the results shown in Figure 5.14, the following observations can be made.

- The open loop case (OL) results in unstable yaw rate and vehicle sideslip behavior.
- The yaw rate behavior in the closed loop case (CL) without friction estimation is undesirable during both the SWD cycles as the yaw rate does not follow its reference. In the closed loop case with friction estimation, the vehicle yaw rate follows its reference much better during both the SWD cycles. The friction estimator is able to improve the controller performance as it provides a better yaw rate reference as explained in Section 5.2 and shown in the second plot of Figure 5.14.
- The vehicle sideslip behavior in the closed loop case without friction estimation is unstable during the second SWD cycle as the vehicle sideslip does not return to zero after the SWD cycle. This is caused by the incorrect saturation limits of the yaw rate reference model in (5.2). In the closed loop case with friction estimation, the vehicle sideslip returns to zero after both the SWD cycles. The friction estimator assists in maintaining a stable vehicle behavior because it provides a better yaw rate reference model as explained in Section 5.2 and this prevents the vehicle sideslip from attaining higher values.
- The friction estimation is accurate compared to the real value. Although the estimation algorithm detects the peak road-tyre friction once the vehicle reaches the nonlinear region of the tyre characteristics, the estimator is able to improve the yaw rate controller performance. Therefore, the proposed road-tyre friction estimator is valuable to active safety systems such as yaw rate control.
- The wrong initialization and the delay due to the fact that the tyre needs to be excited in order to update the estimate does not negatively affect the controller.

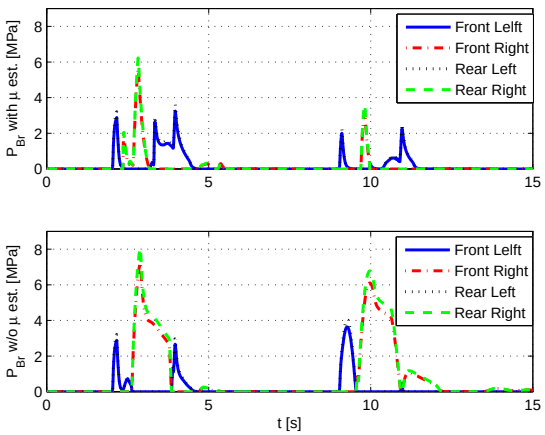

Figure 5.15: Control inputs during a SWD maneuver with μ jump from 0.7 to 0.3 and 0.3 to 0.2.

Figure 5.15 shows the control inputs generated by the controller with and without friction estimation. It is observed that with friction estimation, the control input is smaller in magnitude compared to the case without friction estimation. This implies that the friction estimator is able to reduce the actuator usage of the yaw rate controller.

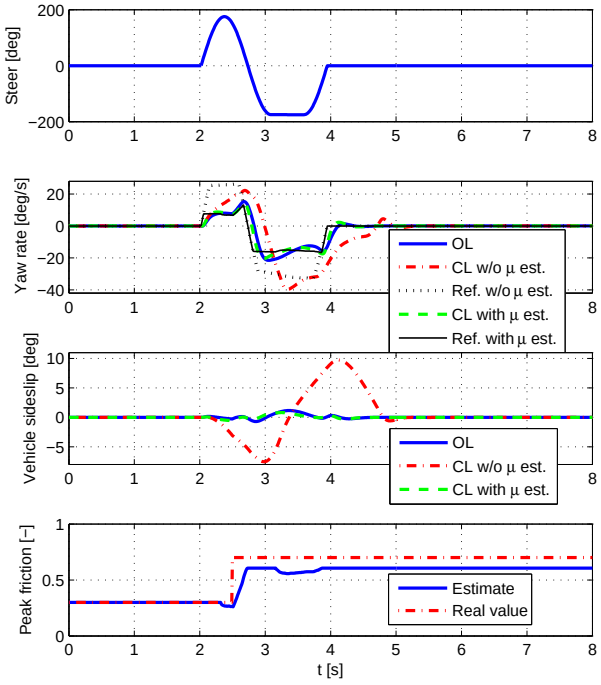

Figure 5.16: Simulation results during a SWD maneuver with μ jump from 0.3 to 0.7.

In the previous simulation study, the road friction changes from a higher to lower value. In the next simulation, the road friction changes from a lower to higher value. The steering and friction profiles are shown in the top and bottom plots of Figure 5.16. In the closed loop case without friction estimation, the yaw rate reference limits in (5.2) is calculated with $\mu = 1$. The vehicle is initialized with a speed of 80 km/h. From the results shown in Figure 5.16, the following observations can be made.

- The open loop case (OL) results in stable yaw rate and vehicle sideslip behavior because the low to high friction change does not push the vehicle outside its stability region.
- The yaw rate behavior in the closed loop case (CL) without friction estimation is undesirable as the yaw rate does not follow its reference and the response is worse than the open loop case. In the closed loop case with friction estimation, the yaw

rate follows its reference well. The friction estimator is able to improve the controller performance as it provides a better yaw rate reference model as explained in Section 5.2.

- The vehicle sideslip behavior in the closed loop case without friction estimation is undesirable as the vehicle sideslip reaches high values compared to the other two cases. This is caused by the incorrect saturation limits of the yaw rate reference model in (5.2). In the closed loop case with friction estimation, the vehicle sideslip is much smaller. The friction estimator assists in maintaining a desirable vehicle behavior as it provides a better yaw rate reference model as explained in Section 5.2 and this prevents the vehicle sideslip from reaching higher values.
- The friction estimator is able to detect the increase in friction but it is not as accurate (12.86 % error) as the previous simulation studies. This is because the vehicle does not reach the peak tyre characteristics. This is a disadvantage of the proposed estimator. However, the vehicle is not undergoing a dangerous maneuver as the open loop case is stable. In case there is a similar change in friction during a maneuver where the open loop case is unstable, the estimator accuracy would be better as the vehicle would reach the peak tyre characteristics.

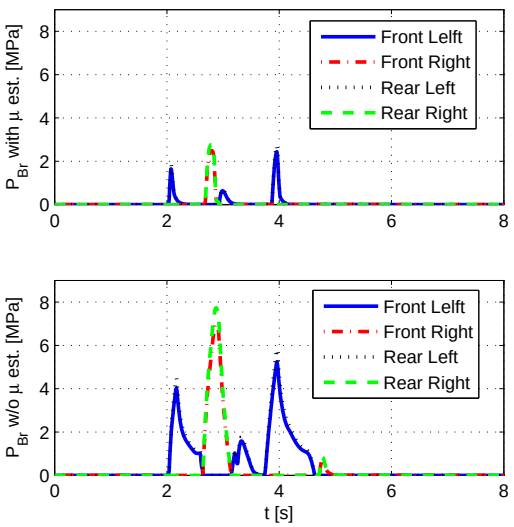

Figure 5.17: Control inputs during a SWD maneuver with μ jump from 0.3 to 0.7.

Figure 5.17 shows the control inputs generated by the two controller configurations. It is observed that with friction estimation, the control input is smaller in magnitude and duration compared to the case without friction estimation. The quadratic control input cost without friction estimation is found to be 41.5, whereas with friction estimation, it is 2.9. This implies that the friction estimator is able to reduce the actuator usage of the yaw rate controller considerably.

5.5.3. VALIDATION WITH EXPERIMENTAL DATA

In this section, the proposed road-tyre friction estimator is validated using the experimental data acquired with the test vehicle. The test vehicle configuration is described in Chapter 2. The test data is collected from ATP proving ground in Papenburg, Germany and the road surface is dry asphalt[1]. Figure 5.18 shows the block diagram of the validation studies.

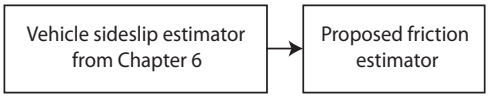

Figure 5.18: The block diagram of the validation studies with experimental data.

The friction estimator is studied using the test data shown in Chapter 2. The estimator is first studied in the presence of lateral dynamics during the Slalom steering maneuver at 60 km/h. The applied steering wheel profile is shown in the top plot of Figure 5.19(a). The combined slip estimate, combined force and the road-tyre friction estimate are also shown in Figure 5.19(a). From the results shown, the following observations can be made.

- The estimated friction is around 1.25. This is an accurate road-tyre friction estimate as the maximum combined force in the middle plot is around 1.25. It is noted that the noise in the force measurements is reflected in the combined force and that the noise levels are quite high when the steering angle is positive. Still the estimator is effective.

- The combined slip value shown in the top plot is estimated as discussed in Section 5.3. The proposed friction estimator uses the vehicle sideslip estimator from Chapter 6 as shown in the friction estimator algorithm in Figure 5.2 and Figure 5.18.

- The friction estimation algorithm captures the maximum combined force values and does not capture incorrect combined force values during lateral dynamics. This is why the estimator does not capture incorrect peak during the first and second cycles of the combined force. Because the tyre is not yet at its limit as supported by the lower combined slip values during the first and second cycles compared to the third cycle.

Next, the friction estimator is studied in the presence of longitudinal dynamics during the braking maneuver from 100 km/h. The steering angle is kept at zero and the applied brake pressure is shown in the top plot of Figure 5.19(b). From the results shown in Figure 5.19(b), the following observations can be made.

- The estimated friction is around 1.1. This is an accurate peak road-tyre friction estimate as the maximum combined force in the middle plot is around 1.1. It is

[1] The test data has been collected by SKF and TNO in 2005.

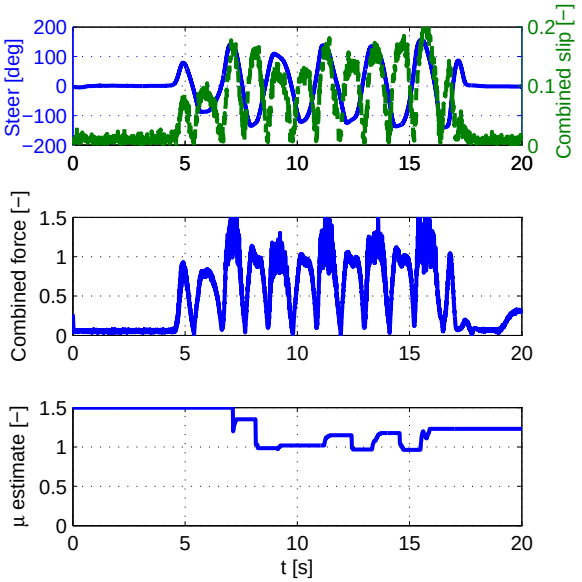

(a) Slalom maneuver at 60 km/h without braking.

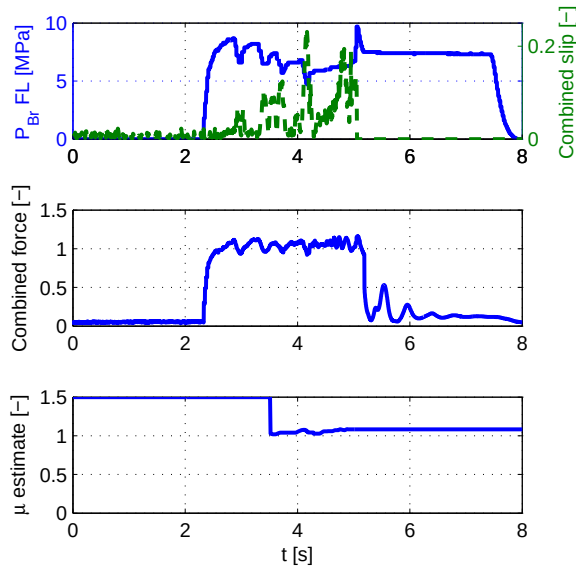

(b) Braking maneuver from 100 km/h without steer.

Figure 5.19: Friction estimation using test data during pure longitudinal or lateral dynamics.

noted that this is lower than the estimate during the Slalom maneuver studied before. This is unusual as longitudinal road-tyre friction is typically higher than the lateral road-tyre friction. This may be because of the high noise level in the combined force in Figure 5.19(a) when the steering angle is positive, which is a result of the force sensor noise.

- The friction estimation algorithm captures the maximum combined force values and does not capture incorrect combined force values during longitudinal dynamics.

So far, pure braking and pure steering maneuvers are studied. Next, the combined slip situation is considered where braking and steering are present. During critical driving situations where active safety systems such as yaw rate controller are active, there is a good probability that the tyres experience combined tyre slip. Therefore, this is an important scenario to study as friction estimation can improve the performance of yaw rate controller as shown in Section 5.5.2.

The vehicle is initialized with a speed of 72 km/h and a constant steering angle of 40 deg is applied throughout the maneuver. This means the tyres experience combined tyre slip. The brake pressure profile and estimation results are shown in Figure 5.20(a). The longitudinal and lateral tyre slips and forces are shown in Figure 5.20(b). From the results shown in Figure 5.20, the following observations can be made.

- The estimated friction is around 1.1. This is an accurate road-tyre friction estimate as the maximum combined force in the middle plot is around 1.1.

- The combined force is approximately 0.5 in the first two seconds of the maneuver. This is because of the constant 40 deg steering angle. The brake pressure is applied from $t = 2.6$ s. Therefore, from $t = 2.6$ s, it is a combined tyre slip situation and the estimator is found to be effective.

- The friction estimation algorithm captures the maximum combined force values and does not capture incorrect combined force values even in the presence of combined tyre slip situations. This demonstrates the robustness of the proposed estimator and its application to use in combination with active safety systems.

- It must be noted that although the combined force reaches its peak before $t = 3$ s, the estimator captures the peak around $t = 3.3$ s because the combined slip signal to noise ratio was lower before $t = 3$ s compared to $t = 3.3$ s. Due to the low combined slip signal to noise ratio, it is difficult to reliability estimate whether the tyre is at its peak before $t = 3$ s. The estimator captures the peak friction when the neccessary conditions described in the algorithm are met so that the estimate is reliable, and this happens around $t = 3.3$ s.

From the validation studies during the longitudinal, lateral and combined slip maneuvers, it is seen that the proposed road-tyre friction estimator is accurate as well as robust.

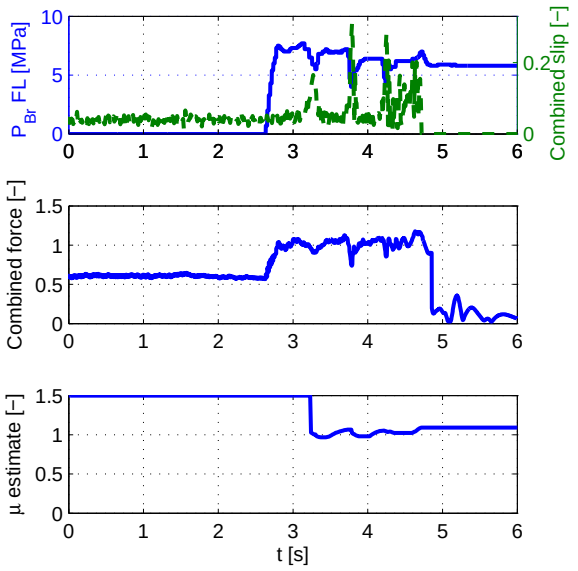

(a) Brake pressure, combined slip, combined force and friction estimate.

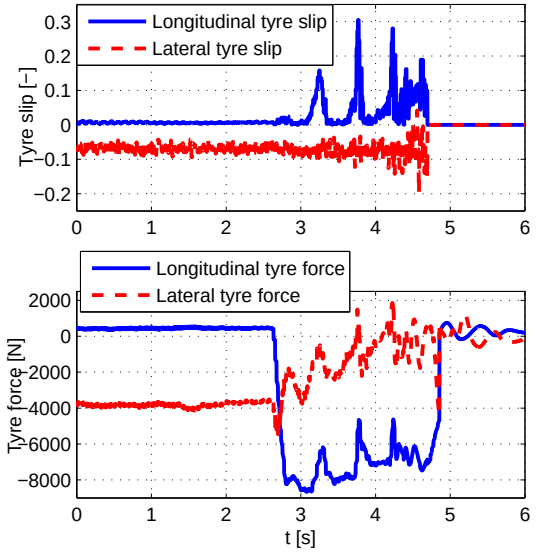

(b) Tyre slip estimates and tyre force measurements.

Figure 5.20: Friction estimation using test data during a braking maneuver with a steering angle of 40 deg. The vehicle starts braking from 72 km/h.

5.6. CONCLUSIONS

A TYRE force measurement based road-tyre friction estimator is proposed in this chapter. The proposed estimator employs a tyre slip and tyre force representations where the longitudinal and lateral tyre slips and forces are combined into a single tyre slip and tyre force values. Therefore, the estimator is effective in the presence of longitudinal dynamics, lateral dynamics and both. The estimator is studied in a simulator environment and is also validated with test data from a BMW 5 Series E60 model test vehicle equipped with Load Sensing Bearings. The main benefits of the proposed estimator are; it is effective during combined tyre slip situations, it is robust as no parameterized tyre model is used, it can be employed to individual tyres and it is computationally inexpensive.

The simulation studies are done using Simulink and CarSim simulation package. From the open loop simulation studies with steering, braking, braking with steering and μ jump maneuvers, the proposed estimator is found to be accurate. The estimator is also studied in closed with the yaw rate controller from Chapter 4 and it is seen that the friction estimator is able to improve the yaw rate controller performance and it reduces the brake actuator usage.

The road-tyre friction estimator is also validated with experimental data from a test vehicle during Slalom, braking and braking with steering maneuvers. The results show good accuracy in the friction estimation and shows robustness against the noise levels in the test data. Future works should study the proposed estimator with the test vehicle on μ jump situations and in closed loop with the yaw rate controller.

6

VEHICLE SIDESLIP ESTIMATION

6.1. INTRODUCTION

IN this chapter, a Kalman based vehicle sideslip estimator is designed, simulated and validated. The proposed sideslip estimator is used by the friction estimator studied in Chapter 5 and is needed to implement the TUCC proposed in Chapter 3. It is defined as the angle between the vehicle longitudinal axis and the vehicle velocity vector. It is denoted by the alphabet β and is shown in Figure 6.1. If the vehicle is driving on a straight-line parallel to the vehicle longitudinal axis, β is 0 deg, and if the vehicle is driving on a straight-line parallel to the vehicle lateral axis, β is 90 deg. The proposed vehicle sideslip estimator uses Load Sensing Bearing (LSB) which can provide tyre force measurements and therefore does not rely on tyre force model. The tyre force measurements benefit the estimator mainly because of the uncertainties and nonlinearities of the tyre force characteristics which depend on factors like temperature, vertical load, road friction, etc. In addition, the proposed estimator does not get affected by the vehicle roll and pitch dynamics. The vehicle sideslip estimator is studied in a simulator environment first. The sideslip estimates are accurate with less than 0.1 deg Root Mean Square Error on dry road. Further, the proposed estimator is validated using several maneuvers performed on a BMW test vehicle instrumented with LSB technology confirming the simulation results.

In addition to its application in the friction estimator in Chapter 5 and the TUCC in Chapter 3, vehicle sideslip is one of the variables controlled by vehicle safety systems like ESP [41, 67, 68]. The vehicle sideslip affects the vehicle yaw moment sensitivity to steering angle [36, 69, 70]. This characteristic makes the vehicle yaw moment less sensitive to steering at higher vehicle sideslips. For a certain range of vehicle sideslip and its time derivative, the vehicle motion is stable whereas outside this range i.e. outside this stability area, the vehicle yaw dynamics is unstable. In addition, as the steering angle increases, the stability area shrinks [71]. This is undesirable for an average driver. There-

Parts of this chapter have been accepted for publication in Control Engineering Practice [57] and published in proceedings of the 23^{rd} Mediterranean Conference on Control & Automation [56].

fore it might be important to estimate and control the vehicle sideslip for better vehicle safety.

The sideslip estimator proposed in this chapter uses tyre force measurements. This chapter studies vehicle sideslip estimation as it is important to implement and test the Tyre Utilization Coefficient Control proposed in Chapter 3 and the Road-Tyre Friction Estimator proposed in Chapter 5. The main contributions of this work are:

1. A force measurement based Kalman Filter is proposed to estimate vehicle sideslip. The proposed vehicle sideslip estimator uses a Kalman filter based on a kinematic model relating vehicle velocities and forces in the longitudinal and lateral directions, and yaw rate. The estimator performance is studied using Root Mean Square Error analysis.

2. The estimator is validated using experimental data from a test vehicle.

3. A heuristic method to overcome the estimate drift, caused by the unobservability when the vehicle yaw rate is close to zero, is also proposed. It is further studied with the help of simulation as well as experimental results.

4. The estimator is studied for robustness against measurement noise and different road frictions.

This chapter is structured as follows. In Section 6.2, the kinematic model is discussed. The Kalman filter design is presented in Section 6.3 and the estimator used to compare the proposed estimator is introduced in Section 6.4. Section 6.5 shows the validation of the proposed method in simulation environment using CarSim and also using real-life experimental data from the test vehicle. Finally, Section 6.6 concludes the chapter.

6.2. KINEMATIC MODEL

THE model used to design the vehicle sideslip estimator is explained in this section. The planar kinematic model of the vehicle is given in (6.1).

$$\begin{bmatrix} \dot{v}_x \\ \dot{v}_y \end{bmatrix} = \begin{bmatrix} 0 & \dot{\psi} \\ -\dot{\psi} & 0 \end{bmatrix} \begin{bmatrix} v_x \\ v_y \end{bmatrix} + \begin{bmatrix} a_x \\ a_y \end{bmatrix}. \tag{6.1}$$

Here $\dot{\psi}$ is the planar yaw rate, v_x and v_y are the vehicle longitudinal and lateral velocities, and a_x and a_y are the planar longitudinal and lateral accelerations. If the sensors are placed at the vehicle CoG to measure the yaw rate and accelerations, because of the vehicle pitch and roll angle, the measurements get corrupted [65]. Therefore, equation (6.1) would become:

$$\begin{bmatrix} \dot{v}_x \\ \dot{v}_y \end{bmatrix} = \begin{bmatrix} 0 & \dot{\psi}_m \cos\theta \cos\phi \\ -\dot{\psi}_m \cos\theta \cos\phi & 0 \end{bmatrix} \begin{bmatrix} v_x \\ v_y \end{bmatrix} + \begin{bmatrix} (a_{x,m} + g\sin\theta)/\cos\theta \\ (a_{y,m} - g\cos\theta\sin\phi)/\cos\phi \end{bmatrix}. \tag{6.2}$$

Here $\dot{\psi}_m$ is the measured yaw rate, $a_{x,m}$ and $a_{y,m}$ are the measured accelerations, θ is the pitch angle, ϕ is the roll angle and g is the gravity. The correction terms are

added in (6.2) to translate the measured yaw rate $\dot{\psi}_m$ to the planar yaw rate $\dot{\psi}$, and the measured accelerations $a_{x,m}$ and $a_{y,m}$ to the planar accelerations a_x and a_y. In (6.2), as accelerations are the system input, the effect of acceleration measurement error on the velocities is higher than the effect of yaw rate measurement error. Therefore, in this work, only the acceleration measurement error is addressed.

If the accelerometer measurements are not compensated for the roll and pitch angle, the vehicle sideslip estimator based on this model could become corrupt. Now if tyre force measurements are instead used to calculate the planar accelerations in (6.1), the roll and pitch dynamics do not affect the estimation model as the tyre force measurements represent the forces acting at the tyre-road contacts. In this work, such an approach is taken. This approach might also be robust to road bank angle and grading as the tyre force sensor measures the effective tyre-road forces acting upon the vehicle. However, it is not studied in this chapter. The differential equations in (6.3) represent the model used to design the sideslip estimator proposed in this chapter.

$$\begin{bmatrix} \dot{v}_x \\ \dot{v}_y \end{bmatrix} = \begin{bmatrix} 0 & \dot{\psi} \\ -\dot{\psi} & 0 \end{bmatrix} \begin{bmatrix} v_x \\ v_y \end{bmatrix} + \begin{bmatrix} \frac{1}{m} & 0 \\ 0 & \frac{1}{m} \end{bmatrix} \begin{bmatrix} F_x \\ F_y \end{bmatrix}. \tag{6.3}$$

Here m is the vehicle mass, and F_x and F_y are the vehicle planar longitudinal and lateral forces. The planar longitudinal and lateral forces F_x and F_y are given by (6.4) and (6.5).

$$\begin{aligned} F_x = {} & F_{x_{FL}} - F_{y_{FL}}\delta_{FL} + F_{x_{FR}} - F_{y_{FR}}\delta_{FR} + F_{x_{RL}} \\ & - F_{y_{RL}}\delta_{RL} + F_{x_{RR}} - F_{y_{RR}}\delta_{RR} - C_{aer}A_L\frac{\rho}{2}v_x^2, \end{aligned} \tag{6.4}$$

$$\begin{aligned} F_y = {} & F_{y_{FL}} + F_{x_{FL}}\delta_{FL} + F_{y_{FR}} + F_{x_{FR}}\delta_{FR} \\ & + F_{y_{RL}} + F_{x_{RL}}\delta_{RL} + F_{y_{RR}} + F_{x_{RR}}\delta_{RR}. \end{aligned} \tag{6.5}$$

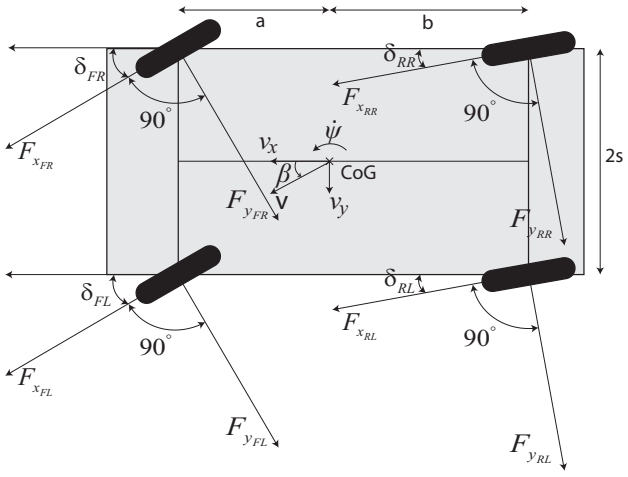

Figure 6.1: Two-track vehicle model.

Here $F_{x_{ij}}$ and $F_{y_{ij}}$ are the longitudinal and lateral forces of ij tyre, C_{aer} is the coefficient of aerodynamic drag, A_L is the front vehicle area, ρ is the air density and δ_{ij} is the road steering angle of ij tyre. In (6.4) and (6.5), small angle approximations $\sin\delta \approx \delta$ and $\cos\delta \approx 1$ are used.

As shown in (6.6) and (6.7), the model in (6.3) is now written in terms of state space variables.

$$\dot{x} = A(t)x + B(t)u + w, \tag{6.6}$$
$$y = Cx + v. \tag{6.7}$$

Here $A(t) = \begin{bmatrix} 0 & \dot{\psi} \\ -\dot{\psi} & 0 \end{bmatrix}$, $x = \begin{bmatrix} v_x \\ v_y \end{bmatrix}$, $B(t) = \begin{bmatrix} \frac{1}{m} & 0 \\ 0 & \frac{1}{m} \end{bmatrix}$, $u = \begin{bmatrix} F_x \\ F_y \end{bmatrix}$, w is the process noise, $y = v_x$, $C = \begin{bmatrix} 1 & 0 \end{bmatrix}$ and v is the measurement noise. The longitudinal velocity v_x measurement or estimate is assumed to be available. It can be estimated using a weigthed average of the four wheel measurements, as usually done in ABS systems [63]. The yaw rate $\dot{\psi}$ and tyre forces are measured, and the lateral velocity v_y is the state to be estimated.

The vehicle sideslip β is shown graphically in Fig. 6.1 as the angle between the vehicle longitudinal axis and the vehicle velocity vector. It is defined mathematically by (6.8):

$$\beta \approx \frac{v_y}{v_x}. \tag{6.8}$$

To get an estimate of the vehicle sideslip β, the lateral velocity v_y state in (6.6) should be estimated. This is further discussed in Section 6.3.

6.2.1. SENSOR NOISE MODEL

The vehicle planar forces F_x and F_y depend on the tyre forces as shown in (6.4-6.5). However, the measurement of these forces is non-trivial. The current LSB techonology is affected by measurements noise. The noise has a characteristic feature as shown in Figure 6.2. The noise is mainly focused around two frequencies. This noise can be taken into account by introducing a sensor noise model. The frequency spectrum of a sample force measurement, taken from the test vehicle shown in Figure 2.1(a) in Chapter 2, is shown in Figure 6.2. Two major frequencies can be observed. The wheel angular velocity causes the one close to 16 Hz and the load sensing bearing hub dynamics, specifically the bearing balls, cause the one close to 200 Hz. The noise model is time-varying as the noise depends on the wheel angular rate. However, in this work, a linear time-invariant noise model is considered as most experiments and analysis are carried out at constant speed.

The measurement noise is modeled with the dynamics shown in the bottom plot of Figure 6.2 in red dash-dot line. As it can be appreciated from Figure 6.2, the proposed model accurately describes the main features of the noise. The noise model dynamics is further transformed into state space representation with the system, input and output matrices A_N, B_N and C_N respectively. This noise model is used in the simulation studies in Section 6.5.1 to consider force measurement noise with comparable properties as the sample measurement shown in Figure 6.2.

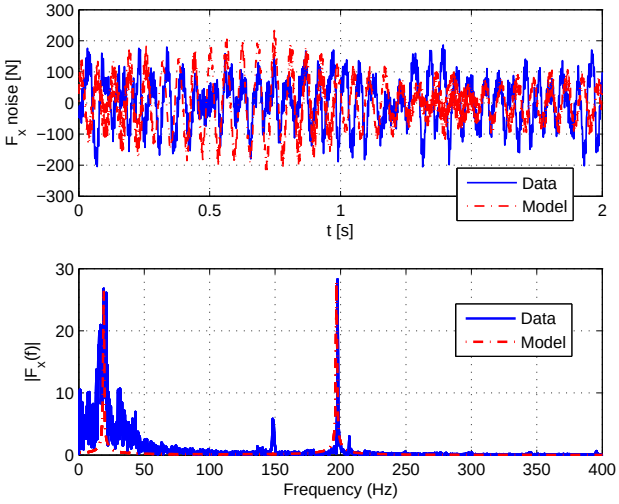

Figure 6.2: Sample F_x noise data from the test vehicle equipped with load sensing bearings, its frequency spectrum, sample noise model output and the noise model bode plot.

6.3. KALMAN-BASED VEHICLE SIDE SLIP ESTIMATION

In this section, a Kalman filter [82] is designed as the vehicle sideslip estimator. Before the estimator is designed, the system observability is studied.

6.3.1. OBSERVABILITY ANALYSIS

The observability of the system is studied when the vehicle is going straight. In (6.9), the observability matrix of the system in (6.6) and (6.7) is given.

$$Obsv = \begin{bmatrix} C \\ CA(t) \end{bmatrix} = \begin{bmatrix} 1 & 0 \\ 0 & \dot{\psi} \end{bmatrix}. \tag{6.9}$$

When the vehicle is going straight, the vehicle yaw rate $\dot{\psi}$ is zero and therefore the observability matrix $Obsv$ loses full rank. Hence an estimator designed based on the system in (6.6) and (6.7) would drift due to unobservability. To handle this unobservability issue, the open loop estimator dynamics in (6.3) is modified as shown in (6.10) when $|\dot{\psi}| < 0.1$ deg/s and $|F_y| < 500$ N.

$$\begin{bmatrix} \dot{\hat{v}}_x \\ \dot{\hat{v}}_y \end{bmatrix} = \begin{bmatrix} 0 & \dot{\psi} \\ -\dot{\psi} & f_v \end{bmatrix} \begin{bmatrix} \hat{v}_x \\ \hat{v}_y \end{bmatrix} + \begin{bmatrix} \frac{1}{m} & 0 \\ 0 & \frac{1}{m} \end{bmatrix} \begin{bmatrix} F_x \\ F_y \end{bmatrix}. \tag{6.10}$$

In the above equation, f_v is a negative valued function as shown in Figure 6.3 and is defined as:

$$f_v = \begin{cases} -20\left(1 - \frac{\dot{\psi}^2}{(0.1\frac{\pi}{180})^2}\right), & \text{if } |\dot{\psi}| < 0.1 \text{ deg/s and } |F_y| < 500 \text{ N} \\ 0, & \text{otherwise} \end{cases} \tag{6.11}$$

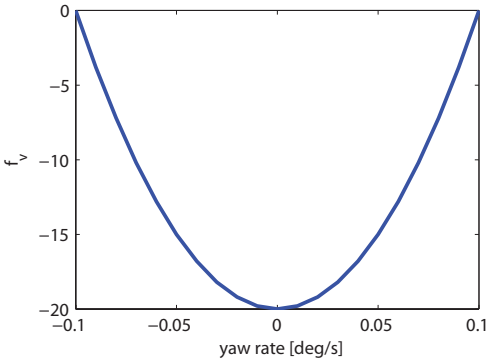

Figure 6.3: f_v as a function of vehicle yaw rate.

Here f_v is defined as a function of yaw rate to provide a smooth intervention of the observability correction so that the estimate decays to zero smoothly. When $|\dot{\psi}|$ is close to zero and $|F_y| < 500$ N, with the modified estimator dynamics in (6.10), the lateral velocity estimate $\hat{v}_y$ and therefore the sideslip estimate $\hat{\beta}$ converges to zero as the eigenvalue corresponding to $\hat{v}_y$ becomes negative. This is a reasonable approach as the sideslip is close to zero when $|\dot{\psi}| < 0.1$ deg/s and $|F_y| < 500$ N because the vehicle is going almost straight, and therefore the estimation error is acceptable compared to the estimate $\hat{\beta}$ drifting away from zero. This method to determine whether the vehicle is going straight is similar to the approach used in [85], where if the yaw rate is below a defined threshold for a given period, it is assumed that the vehicle is going straight. The approach used in [85] might fail when the vehicle experiences pure lateral drift whereas the inequalities used in (6.11) would hold. Forcing the f_v term onto the dynamics is equivalent to modifying the vehicle dynamics by adding a fictitious effect when the yaw rate and the lateral force are small. This heuristic solution is derived from the consideration that the only driving scenarios compatible with the above defined conditions are either straight driving with negligible side slip or pure, stable lateral drift on very low friction surfaces. The latter is obviously a very rare condition that can be discarded. A loss of stability on very low friction is indeed probable, but the vehicle dynamics analysis shows that in those conditions the vehicle would not be stable and thus the yaw rate would not be small.

6.3.2. ESTIMATOR DESIGN

The estimator is designed using the modified system dynamics in (6.10). Using zero-order hold approach, the continuous-time state space model in (6.6) and (6.7) with $A(t) = \begin{bmatrix} 0 & \dot{\psi} \\ -\dot{\psi} & f_v \end{bmatrix}$ is discretized as a linear time-varying system:

$$x(k+1) = A(k)x(k) + B(k)u(k) + w(k), \tag{6.12}$$

$$y(k) = C(k)x(k) + v(k). \tag{6.13}$$

As shown in Figure 6.4, the Kalman filter estimates both the present state $\hat{x}(k|k) =$

$\begin{bmatrix}\hat{v}_x(k|k)\\ \hat{v}_y(k|k)\end{bmatrix}$ and the one-step-ahead state $\hat{x}(k+1|k) = \begin{bmatrix}\hat{v}_x(k+1|k)\\ \hat{v}_y(k+1|k)\end{bmatrix}$ of the time varying system. The following equations (6.14-6.16) describe the present state $\hat{x}(k|k)$ [83].

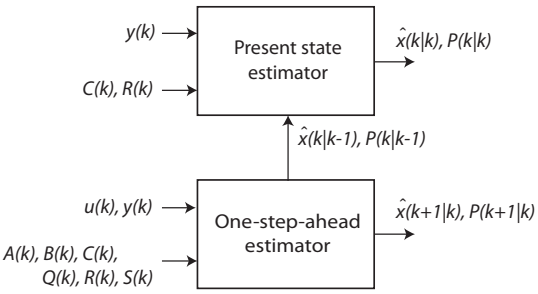

Figure 6.4: Kalman filter block diagram.

$$K'(k) = P(k|k-1) \times C(k)^T \left[R + C(k) P(k|k-1) C(k)^T\right]^{-1}, \tag{6.14}$$

$$\hat{x}(k|k) = \hat{x}(k|k-1) + K'(k)\left[y(k) - C(k)\hat{x}(k|k-1)\right], \tag{6.15}$$

$$P(k|k) = P(k|k-1) - K'(k) C(k) P(k|k-1). \tag{6.16}$$

Here $K'(k)$ is the Kalman gain, $P(k|k-1)$ is the one-step-ahead state error covariance matrix at time $k-1$, R is the measurement noise covariance matrix, $\hat{x}(k|k)$ is the state estimate at time k, $\hat{x}(k|k-1)$ is the one-step-ahead state estimate at $k-1$ and $P(k|k)$ is the state error covariance matrix at time k. The following equations (6.17-6.19) describe the one-step-ahead predicted state $\hat{x}(k+1|k)$.

$$K(k) = \left[S + A(k) P(k|k-1) C(k)^T\right] \times \left[R + C(k) P(k|k-1) C(k)^T\right]^{-1}, \tag{6.17}$$

$$\hat{x}(k+1|k) = A(k)\hat{x}(k|k-1) + B(k)u(k) + K(k)\left[y(k) - C(k)\hat{x}(k|k-1)\right], \tag{6.18}$$

$$P(k+1|k) = A(k) P(k|k-1) A(k)^T + Q - K(k)\left[S + A(k) P(k|k-1) C(k)^T\right]^T. \tag{6.19}$$

Here $K(k)$ is the Kalman gain, S is the cross-correlation matrix between the process and measurement noise, $\hat{x}(k+1|k)$ is the one-step-ahead state estimate at time k, $P(k+1|k)$ is the one-step-ahead state error covariance matrix at time k and Q is the process noise covariance matrix.

For the simulation studies, the measurement noise covariance R is calculated from a sample output measurement noise from the test vehicle. The process noise covariance Q is tuned during the estimator implementation and the cross-correlation S is assumed to be zero. For studies with the test data, Q and R matrices are found using an optimization algorithm. This is further discussed in Section 6.5.2.

From the present state estimate $\hat{x}(k|k) = \begin{bmatrix} \hat{v}_x(k|k) \\ \hat{v}_y(k|k) \end{bmatrix}$, the vehicle sideslip estimate $\hat{\beta}(k)$ is calculated as:

$$\hat{\beta}(k) = \frac{\hat{v}_y(k|k)}{\hat{v}_x(k|k)}. \tag{6.20}$$

6.3.3. SENSOR OFFSET COMPENSATION

Vehicle sideslip estimators are often sensitive to sensor offset values. For example, the effects of longitudinal and lateral accelerometer offsets are studied and reported in [81]. The tyre force sensors also have offset in the longitudinal and lateral measurements, and as the proposed estimator is observed to be sensitive to these offsets, the following algorithm is used to compensate for them.

$$\begin{aligned} IF\ |T_{EN}| < 2\ Nm\ AND\ P < 0.1\ bar \\ F_x^{offset} = moving\ average(F_x) \end{aligned} \tag{6.21}$$

$$\begin{aligned} IF\ |\delta| < 0.1\ deg\ AND\ |\dot{\psi}| < 0.01\ deg/s \\ F_y^{offset} = moving\ average(F_y) \end{aligned} \tag{6.22}$$

The moving average is calculated over a period of 0.2 s. In this duration, 100 measurement samples are available. Here T_{EN} is the engine torque and P is the brake pressure. The pressure is often directly measured, while an estimation of the engine torque is available on all modern engines.

6.4. ACCELEROMETER BASED VEHICLE SIDESLIP ESTIMATOR

IN this section, the accelerometer based vehicle sideslip estimator used to benchmark the proposed estimator is introduced. The accelerometer based sideslip estimator is an implementation of the Kinematic model based observer design proposed in [78]. The process noise covariance Q and measurement noise covariance R are tuned according to the same approach used to tune the force based estimator. The cross-correlation S is assumed to be zero.

When the CarSim multi-body vehicle model is set such that the accelerations are measured at the road level, the accelerometer based estimator gives accurate results. However in commercial vehicles, the accelerometers are typically placed close to the vehicle CoG. Therefore, the accelerometer measurements are often affected by the vehicle roll and pitch dynamics.

6.5. RESULTS

In this section, two sets of studies are performed and their results are discusssed.

1. First, various simulation studies are conducted with different configurations of the proposed vehicle sideslip estimator. The vehicle model being simulated is the CarSim multi-body model explained in Section 6.1. The results are compared with the real sideslip values and the accelerometer based sideslip estimator introduced in the previous section.

2. Next, the proposed estimator is validated with test data from a BMW 5 Series E60 model test vehicle. Here the objective is to study the effectiveness of the estimator in a real vehicle. This is further discussed in Section 6.5.2.

6.5.1. SIMULATION STUDIES

Using the CarSim simulation environment, the proposed vehicle sideslip estimator is studied in this section. The estimator is also compared with the real vehicle sideslip values and the accelerometer based vehicle sideslip estimator. In order to account for the load sensing bearing hub noise in these simulation studies, the longitudinal and lateral tyre force measurements from CarSim are polluted with filtered white noise according to the noise model identified in Section 6.2.1. The filtered white noise has comparable properties as the sample measurement shown in Fig. 6.2.

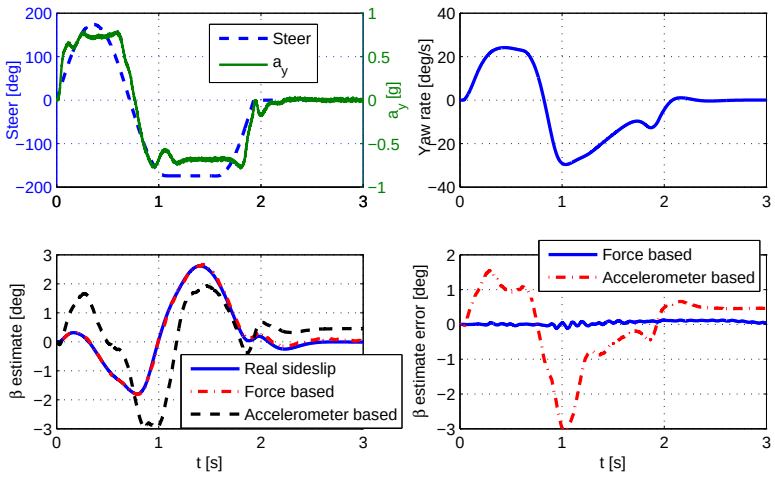

Figure 6.5: Vehicle sideslip estimation during the Sine with Dwell maneuver at a vehicle speed of 80 km/h.

In the first simulation study, the estimator is studied with the Sine with Dwell (SWD) steering input shown in Figure 6.5 at a vehicle speed of 80 km/h. In this simulation, no measurement bias is considered. From the results shown in Figure 6.5, it is observed that as the accelerometer measurements are corrupted with roll and pitch dynamics, the accelerometer based estimate does not track the reference well. This is caused by the

roll and pitch dynamics as discussed in Section 6.2, whereas the force based estimator is accurate. Due to the roll and pitch angle, the accelerometer measurements are not same as the accelerations on the road plane and this error affects the accuracy of the accelerometer based estimator. The differences in accelerations and the roll and pitch angle causing them are shown in Figure 6.6. Although the differences in accelerations in Figure 6.6 look small in magnitude, the sideslip estimator is sensitive to these differences because of its integral nature. On the other hand, as the measured tyre forces represent the forces acting at the road-tyre contacts, the force based estimate is not corrupted with the roll and pitch dynamics. It should be noted that even though the roll angle converges to zero for $t > 2.5$ s, the acceleromenter based estimate does not converge to zero for $t > 2.5$ s because of the unobservability issue when the yaw rate is close to zero. For the considered SWD maneuver, in the lateral acceleration range $\{-0.9, 0.9\}$ g, the force based estimator is able to estimate vehicle sideslip with RMSE less than 0.1 deg as shown in Table 6.1.

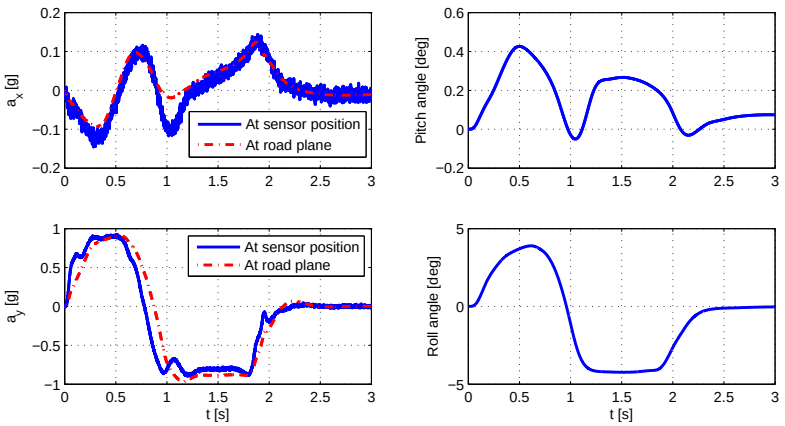

Figure 6.6: Vehicle accelerations, roll angle and pitch angle during the Sine with Dwell maneuver at 80 km/h.

Table 6.1: Estimator Root Mean Square Error

Simulation type	Force based	Accelerometer based
Sine with Dwell	0.0716 deg	1.4042 deg
Double Lane Change	0.0481 deg	0.8282 deg
Fish Hook	0.0423 deg	1.3517 deg
Low friction	0.2570 deg	6.0097 deg

In Figure 6.7-6.9, simulation results are shown for Double Lane Change, Fish Hook and low friction maneuvers. The RMSE values of these simulations are shown in Table 6.1.

From the Double Lane Change and Fish Hook maneuver simulation results in Figure 6.7 and 6.8, the force measurement based estimator has better accuracy than the

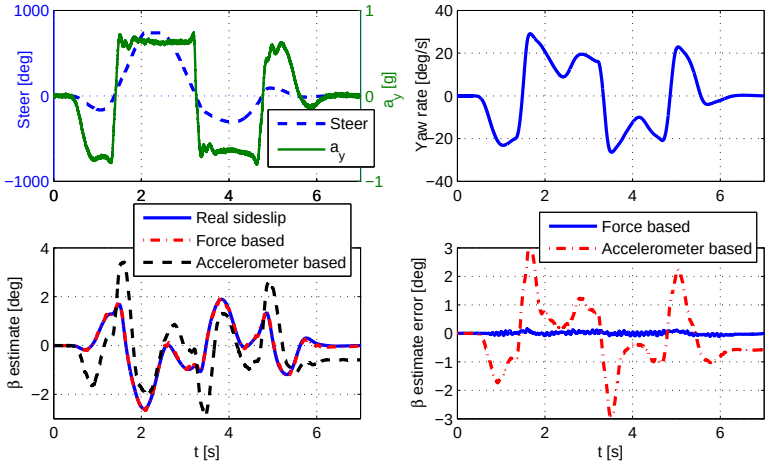

Figure 6.7: Vehicle sideslip estimation during the Double Lane Change maneuver with a speed of 80 km/h.

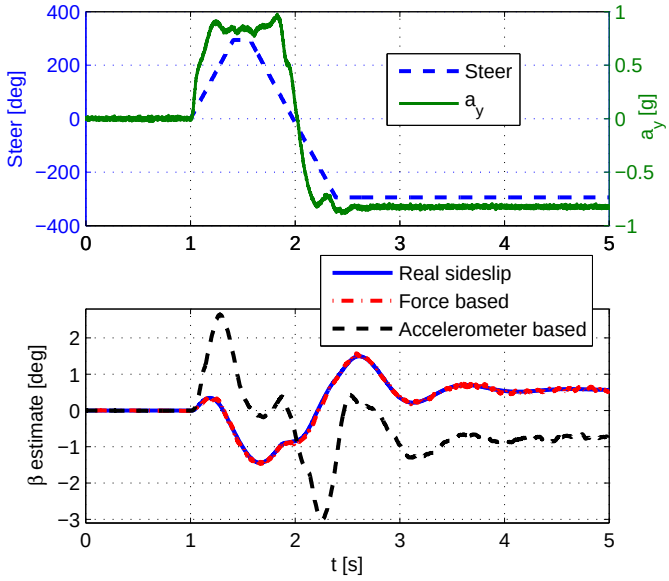

Figure 6.8: Vehicle sideslip estimation during the Fish Hook maneuver with a vehicle speed of 79 km/h.

accelerometer based estimator. As mentioned before, the unmodelled roll and pitch dynamics degrade the accelerometer based estimator accuracy. From Table 6.1, the force measurement based estimator estimates the sideslip with RMSE less than 0.1 deg. It must be noted that the accelerometer based estimator accuracy can be improved if roll

and pitch angle estimates are available.

Next, simulation studies are performed on a low friction surface with friction 0.2. In Figure 6.9, the throttle and steering wheel inputs are shown. They are chosen such that the vehicle experiences combined slip with high vehicle sideslip values. It is observed from the results shown in Figure 6.9 and Table 6.1 that even on low friction surfaces, the force measurement based estimator estimates the vehicle sideslip accurately. This is an advantage with respect to the physical model based estimation [76] discussed in Section 6.1. From Table 6.1, it is observed that the RMSE of the accelerometer based estimator is about 6 deg which is quite high for vehicle sideslip error, whereas the force based estimator gives RMSE less than 0.3 deg. It should be noted that in Table 6.1, the large increase in the RMSE of the low friction simulation is because the magnitude of the sideslip angle is much higher compared to the other cases simulated. The force based estimator's normalized RMSE is 0.0162, 0.0107, 0.0144, 0.0109 for the Sine with Dwell, Double Lane Change, Fish Hook and low friction maneuvers respectively, which are comparable.

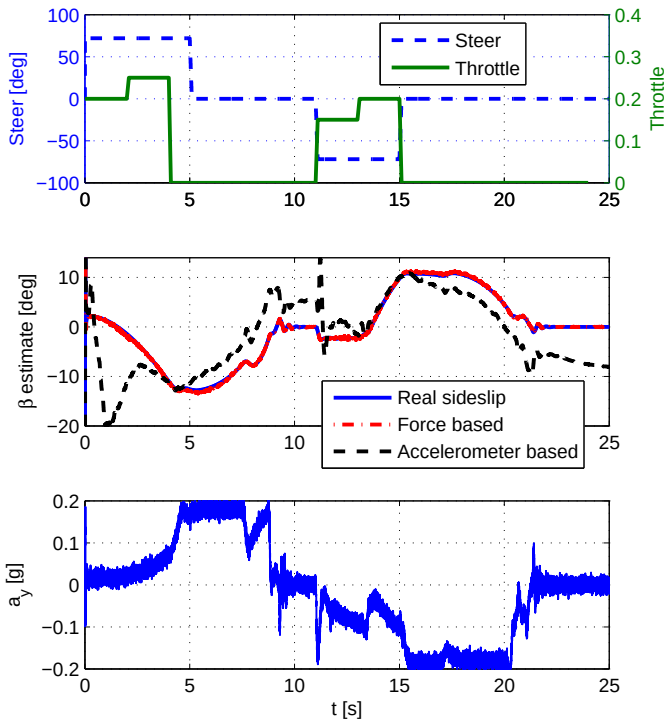

Figure 6.9: Vehicle sideslip estimation with road friction 0.2.

The unobservability issue discussed in Section 6.3.1 is studied next with a SWD manuever at a vehicle speed of 80 km/h in the presense of 200 N measurement bias in F_y. The SWD

steering profile as well as the simulation results are shown in Figure 6.10. It is seen that without the unobservability correction, the estimate is not accurate. The unobservability issue while the yaw rate is close to zero causes estimation error after the SWD cycle ends at 2.5 s and it causes the estimate to drift, whereas with the unobservability correction discussed in Section 6.3.1, the the vehicle sideslip estimate is accurate throughout the manuever. This is seen in Figure 6.10.

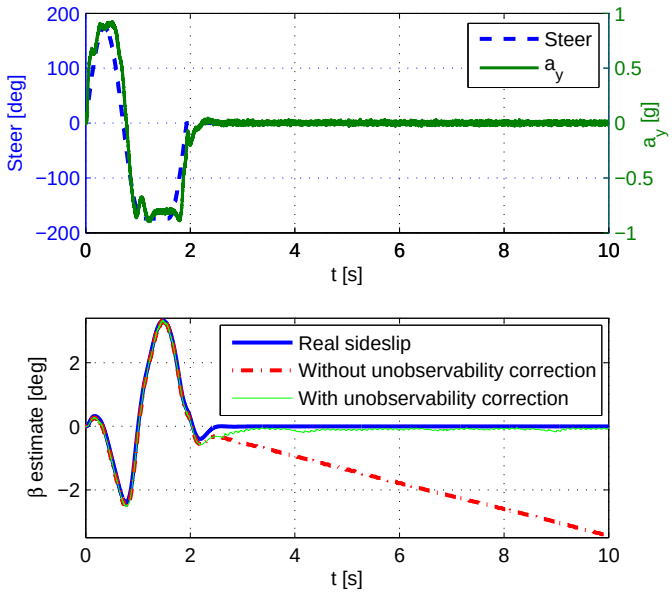

Figure 6.10: Vehicle sideslip estimation during Sine with Dwell maneuver at 80 km/h in the presense of 200 N measurement bias in F_y demonstrating the unobservability issue when the yaw rate is close to zero.

The unobservability issue is also seen in the low friction simulation results in Figure 6.9. As the accelerometer based estimator does not have the unobservability correction, when $t > 22$ s, the vehicle sideslip estimate drifts to higher negative values. It is indeed important for ESCs to have an accurate sideslip estimate in such low friction situations because such situations are prone to accidents. With the unobservability correction, the force measurement based estimate is accurate and there is no drift when $t > 22$ s.

6.5.2. VALIDATION WITH EXPERIMENTAL DATA

In this section, the proposed vehicle sideslip estimator is validated using the experimental data acquired with the test vehicle. The test vehicle configuration is described in Chapter 2. The test data is collected from ATP proving ground in Papenburg, Germany[1]. The real sideslip is calculated using the longitudinal and lateral speed measurements of the laser speed sensors.

[1] The test data has been collected by SKF and TNO in 2005.

The LSB based vehicle sideslip estimator is validated with test data from J turn, Lane Change and Slalom maneuvers. The LSB tyre force measurements from these maneuvers are shown in Figure 2.2-2.4 of Chapter 2. The Q and R matrices are initialized with their values from the simulation studies, and are further tuned using a constrained optimization algorithm. The optimization objective is to minimize the integral of the magnitude of the estimation errors in the considered three maneuvers and it is a constrained optimization such that $Q > 0$ and $R > 0$. The same procedure is used to tune the accelerometer based estimator. For the force based estimator, the optimized values of Q and R are $\begin{bmatrix} 0.1805 & 0 \\ 0 & 1.0167 \end{bmatrix}$ and 0.001 respectively, and for the accelerometer based estimator, the optimized values of Q and R are $\begin{bmatrix} 0.1 & 0 \\ 0 & 1.0 \end{bmatrix}$ and 0.01 respectively.

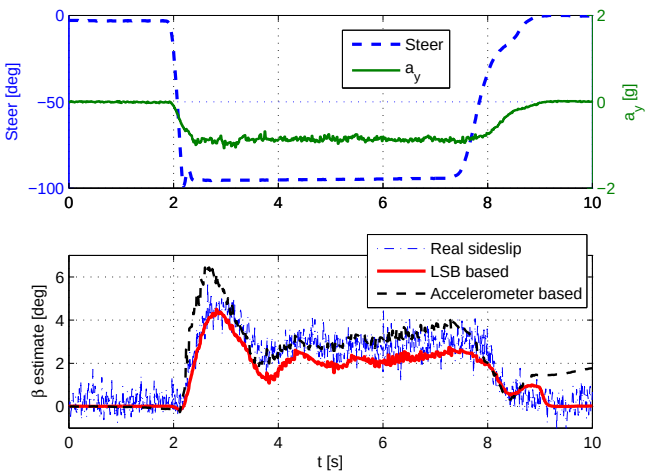

Figure 6.11: Steering wheel angle, lateral acceleration and vehicle sideslip estimate during a J turn maneuver at an initial vehicle speed of 100 km/h.

The J turn maneuver is performed at an initial vehicle speed of 100 km/hr and the applied steering profile is shown in the top plot of Figure 6.11. From the results shown in Figure 6.11, it is observed that both the LSB based and accelerometer based estimators are accurate during the maneuver. However, the accelerometer based estimate drifts away for $t > 9$ s due to unobservability, whereas the LSB based estimate is accurate for $t > 9$ s. It must be noted that for non-zero steering angles, the accelerometer based estimate error is lesser than the simulation studies in Section 6.5.1. This might be because of the test vehicle's anti-roll bar which reduces the roll angle.

Further validation of the estimator is performed with the experimental data from Slalom and Lane Change maneuvers. The results are shown in Figure 6.12 and 6.13. The vehicle experiences lateral acceleration in the range $\{-1, 1\}$ g as seen in the plots. In both the maneuvers, it is observed that the LSB based estimator estimates the vehicle sideslip accurately and gives better estimates compared to the accelerometer based estimator.

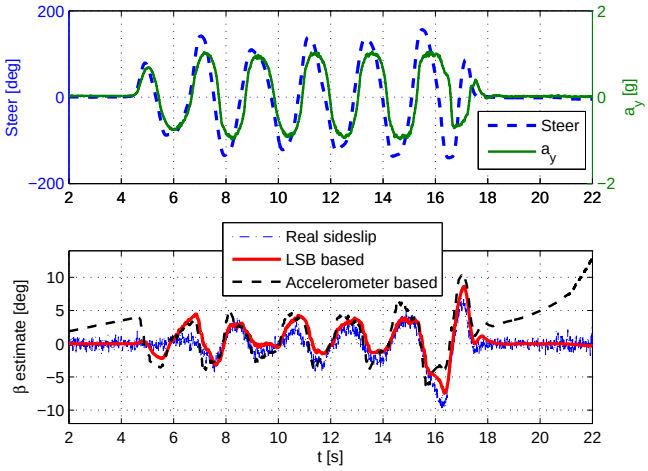

Figure 6.12: Vehicle sideslip estimation using test data from Slalom maneuver at an initial vehicle speed of 60 km/h.

In addition, the accelerometer based estimates drift when the vehicle is going straight because of the unobservability issue, whereas the LSB based estimates do not drift as the issue is addressed as discussed in Section 6.3.1.

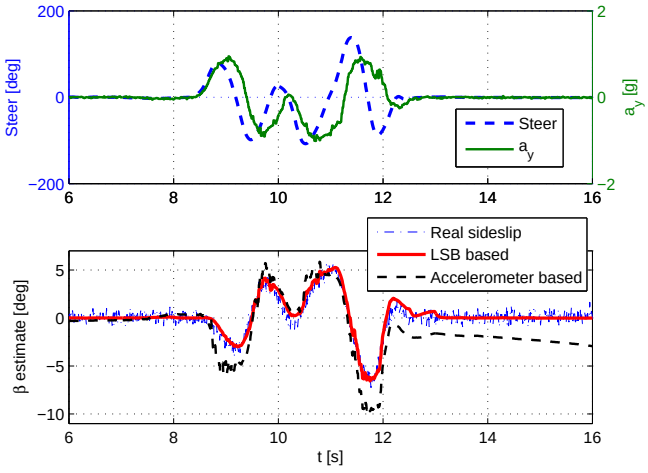

Figure 6.13: Vehicle sideslip estimation using test data from Lane Change maneuver at an initial vehicle speed of 104 km/h.

An interesting event is happening during the Lane Change maneuver around $t = 11.75$ s. The accelerometer based estimate has high error. This happens because the

Lane Change maneuver is pushing the vehicle to its limits of stable operating region. This is evident from the top plot of Figure 2.4(b) as ESP intervention (severe braking only on the front right tyre) is present around $t = 11.75$ s. During this time, pitch and roll dynamics are present, and the accelerometer based estimator is no more accurate, whereas the LSB based estimator is accurate. Similar event is happening around $t = 9$ s and is caused by another ESP intervention (as evident from the braking of only the front left tyre in Figure 2.4(a)). These events demonstrate that the proposed LSB based vehicle sideslip estimator is accurate during critical maneuvers. From the validation results in Figure 6.11, 6.12 and 6.13, it is concluded that the LSB based vehicle sideslip estimator is suitable for sideslip estimation in a real vehicle.

6.6. CONCLUSIONS

A TYRE force measurement based vehicle sideslip estimator is proposed in this chapter. Using the vehicle kinematic model, a Kalman filter is designed and studied as the vehicle sideslip estimator. This chapter also proposes a heuristic method to handle the unobservability issue with the kinematic model based vehicle sideslip estimation while the yaw rate is close to zero. The proposed estimator is finally validated with the test data from a BMW 5 Series E60 model test vehicle equipped with LSB technology.

The proposed vehicle sideslip estimator is tested using simulation studies as well as test data. From the simulation studies with Sine with Dwell, Double Lane Change, Fish Hook and low friction manuevers, the proposed estimator is found to be accurate with RMSE values shown in Table 6.1. Compared to the accelerometer based vehicle sideslip estimator, the proposed force based estimator is found to be more accurate. The benefit is mainly due to the insensitivity of the force based method to the roll and pitch dynamics. In the lateral acceleration range $\{-0.9, 0.9\}$ g, the proposed estimator shows good accuracy.

The vehicle sideslip estimator is also validated with experimental data from the test vehicle during a J turn, Lane Change and Slalom maneuver. The results show good accuracy in the sideslip estimation when compared with the real sideslip calculated using the laser speed sensors equipped in the test vehicle, and the estimator is more accurate than the accelerometer based vehicle sideslip estimator. The proposed estimator is also observed to be effective during ESP interventions.

In addition, the proposed sideslip estimator is used in the road-tyre friction estimator studied in Chapter 5, demonstrating the sideslip estimator's application in active vehicle safety systems. It is worth remembering that in Chapter 5, the friction estimator, which uses the sideslip estimator proposed in this chapter, is studied in open loop (using simulation and experimental data) as well as closed loop with the yaw rate controller from Chapter 4, and the lateral vehicle safety is improved as seen in the results of Chapter 5, showing the application of the sideslip estimator proposed in this Chapter.

Future works include experimenting the proposed estimator using the test vehicle on different road friction values.

7

CONCLUSIONS AND RECOMMENDATIONS

THIS dissertation primarily studies the benefits of tyre force measurements on active safety systems for lateral vehicle dynamics. In this direction, different components of active safety systems, such as Vehicle Dynamics Control (VDC) and Vehicle State Estimator (VSE), are studied.

7.1. CONTRIBUTIONS OF THIS DISSERTATION

THIS dissertation proves the potential of force based lateral VDC accounting for different aspects from estimation to control and considering different types of actuators. It shows that the force based methods can be adapted to many VDC aspects. In particular, the contributions of this dissertation are the proposed TUCC using individual front wheel steering actuators, yaw rate control using braking actuators, vehicle sideslip estimator and the road-tyre friction estimator considering combined tyre slip. Their contributions are further discussed in the following four subsections.

7.1.1. TYRE UTILIZATION COEFFICIENT CONTROL

IN Chapter 3, a new method for lateral vehicle dynamics control using tyre force measurements and active front steering is proposed. First, a simulation study exemplifies the fact that during cornering, the Tyre Utilization Coefficients (TUC) are not evenly employed. This can get one of the front tyres to hit saturation before the others, thereby possibly causing discomfort for an average driver or even an unstable situation. Next, the TUCC is proposed to address this issue with the objective of keeping the front left and front right TUCs equal i.e. $k_{FL} = k_{FR}$. As a consequence of the proposed TUCC, the vehicle is able to maintain the maximum possible lateral acceleration when a driver applies higher steering angles. The TUCC can be a useful idea for cars with active steering, for example the ongoing autonomous driving projects [2, 3].

The TUCC is designed using Sliding Mode Control theory. The proposed controller is

tested in several conditions ranging from quasi-steady state cornering to a more dynamically demanding Sine with Dwell (SWD) maneuver. During the ramp steering cornering, the TUCC is observed to be able to achieve the control objective $k_{FL} = k_{FR}$. During the SWD maneuver, it is observed that the vehicle is stable with the TUCC whereas the car goes unstable without the TUCC.

Secondly, another simulation study exemplifies that when an average driver applies steering higher than a certain threshold, assuming he will get more lateral acceleration, he might in fact be settling for a lesser lateral acceleration. Whereas with the TUCC, lateral acceleration is maintained very close to its maximum in such driving situations, thereby assisting the driver.

The TUCC is also found to be robust for different SWD amplitudes. In order to make the TUCC robust for different vehicle speeds, a speed dependent gain scheduling is used. The closed loop system is further tested in the presence of measurement noise and is found to be robust. Finally, the controller is studied for various peak road-tyre friction values and is found to be robust.

However, the TUCC assumes the road-tyre friction and vehicle sideslip to be known or an estimate to be available. In Chapter 5 and 6, road-tyre friction and vehicle sideslip estimation using tyre force measurements are studied as they are needed to implement the proposed TUCC.

7.1.2. YAW RATE CONTROL

ELECTRONIC Stability Control (ESC) in commercial cars typically controls vehicle yaw rate using braking actuators. In Chapter 4, how tyre force measurements can benefit the yaw rate control problem using braking actuators is studied. A novel computationally inexpensive feedback linearization based yaw rate controller using tyre force measurements is studied in this direction. Most of the yaw rate controllers use a tyre model that introduces modeling error because of the tyre model nonlinearities and uncertainties. This may degrade the controller performance, whereas the proposed yaw rate controller does not employ a tyre model. It uses tyre force measurements and a nonlinear yaw rate model. As a result, the control design and control gain do not directly depend upon the vehicle speed and vehicle sideslip.

The proposed controller is studied in split-μ and SWD simulations using Simulink and CarSim environment. During both simulations, it is observed that the vehicle is stable in closed loop, whereas the vehicle becomes unstable in open loop. The controller is also found to be robust to vehicle speed and to measurement noise in vehicle speed, yaw rate and tyre forces. Overall, with the availability of tyre force measurements, the proposed yaw rate control offers a robust and computationally inexpensive alternative in cars with braking actuators.

In Chapter 4, the yaw rate reference limit defined by the yaw rate reference model is calculated with a road-tyre friction value of 1. This can limit the controller performance for different friction values. A road-tyre friction estimator can address this issue and this is studied in Chapter 5.

7.1.3. ROAD-TYRE FRICTION ESTIMATION

In Chapter 5, a tyre force measurement based road-tyre friction estimator is proposed. The proposed estimator employs a tyre slip and tyre force representations where the longitudinal and lateral tyre slips and forces are combined into a single tyre slip and tyre force values. Therefore, the estimator is effective in the presence of longitudinal dynamics, lateral dynamics and both. The friction estimator uses the vehicle sideslip estimator proposed in Chapter 6 to calculate the combined tyre slip. The estimator is studied in a simulator environment and is also validated with the test data from a BMW 5 Series E60 model test vehicle equipped with Load Sensing Bearing (LSB) technology. The main benefits of the proposed estimator are: it is effective during combined tyre slip situations, it is robust as no parameterized tyre model is used, it can be employed to individual tyres and it is computationally inexpensive.

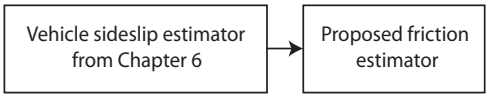

Figure 7.1: Block diagram of the open loop simulation studies and the open loop validation studies with experimental data, where the friction estimator is integrated with the sideslip estimator from Chapter 6.

The simulation studies are done using Simulink and CarSim simulation package. From the open loop simulation studies with steering, braking, braking with steering and μ jump maneuvers, the proposed estimator is found to be accurate. The estimator is also studied in closed loop with the yaw rate controller proposed in Chapter 4 and it is seen that the friction estimator is able to improve the yaw rate controller robustness to friction and it reduces the brake actuator usage.

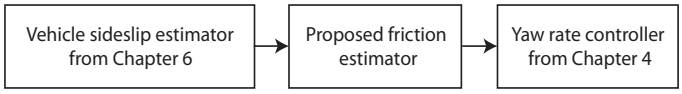

Figure 7.2: Block diagram of the closed loop simulation studies where the friction estimator, sideslip estimator from Chapter 6 and the yaw rate control from Chapter 4 are integrated.

The road-tyre friction estimator is also validated with experimental data from a test vehicle during slalom, braking and braking with steering maneuvers. The results show good accuracy in the friction estimation and shows robustness against the noise levels in the test data.

7.1.4. VEHICLE SIDESLIP ESTIMATION

In Chapter 6, a tyre force measurement based vehicle sideslip estimator is proposed. Using the vehicle kinematic model, a Kalman filter is designed and studied as the vehicle sideslip estimator. This chapter also proposes a heuristic method to handle the unobservability issue with the kinematic model based vehicle sideslip estimation while the yaw rate is close to zero. The proposed estimator is also validated with the test data from a BMW 5 Series E60 model test vehicle equipped with LSB technology.

The proposed vehicle sideslip estimator is tested using simulation studies as well as test data. From the simulation studies with Sine with Dwell, Double Lane Change, Fish Hook and low friction manuevers, the proposed estimator is found to be accurate with RMSE values shown in Table 6.1. Compared to the accelerometer based vehicle sideslip estimator, the proposed force based estimator is found to be more accurate. The benefit is mainly due to the insensitivity of the force based method to the roll and pitch dynamics. In the lateral acceleration range $\{-0.9, 0.9\}$ g, the proposed estimator shows good accuracy.

The vehicle sideslip estimator is also validated with experimental data from the test vehicle during a J turn, Lane Change and Slalom maneuver. The results show good accuracy in the sideslip estimation when compared with the real sideslip calculated using the laser speed sensors equipped in the test vehicle, and the estimator is more accurate than the accelerometer based vehicle sideslip estimator. The proposed estimator is also observed to be effective during ESP interventions.

As shown in Figure 7.1 and Figure 7.2, the sideslip estimator proposed in Chapter 6 is used by the friction estimator and the yaw rate controller, demonstrating its modularity with other active safety system components.

7.2. RECOMMENDATIONS

THIS dissertation is a part of the ongoing research at TU Delft on Load Sensing Bearing (LSB) [60] based active safety systems. In the previous PhD dissertation [4], longitudinal vehicle dynamics control using the LSB technology was the main focus of research [14–16]. This dissertation focuses on the lateral dynamics: two lateral vehicle dynamics controllers, a sideslip estimator and a road-tyre friction estimator are studied.

In the TUCC proposed in Chapter 3, the road-tyre friction and vehicle sideslip are assumed to be known, which is usually not the case. Therefore the TUCC should be integrated and studied with the road-tyre friction and vehicle sideslip estimators from Chapter 5 and 6. Another potential area of improvement is the TUCC design. It is presently designed using a linear tyre model and a vehicle model that depends on the vehicle speed. This necessitates the speed dependent gain scheduling. Instead it might be interesting to explore an alternative TUCC design without using a tyre model and a vehicle model that depends on the speed.

The yaw rate controller using braking actuators, proposed in Chapter 4, is so far studied only in simulation. Once the final LSB prototype is reached, the yaw rate controller may be tested in the BMW test vehicle at TU Delft as it is already equipped with braking actuators.

It is also recommended to experiment the road-tyre friction and vehicle sideslip estimators proposed in Chapter 5 and 6 using the test vehicle on different road friction values. The effect of road grade and road banking on the tyre force measurement based vehicle sideslip estimator should also be studied.

As seen in Chapter 2, the LSB technology (year 2005 version) has a standard deviation of the order 10 % from an expensive Corrsys tyre force sensor. In addition, the force calculations in Chapter 2, 5 and 6 use lateral acceleration and brake pressure measurements from the vehicle Controller Area Network (CAN) bus in addition to the six LSB strain gauge measurements. Because the LSB technology needs further development be-

fore it can be robust and can measure tyre forces without additional variables. Already research is being carried out in this direction at TU Delft and this dissertation reiterates its importance. The LSB measurements might be sensitive to the bearing wear and it should also be studied.

Overall, this dissertation offers a positive recommendation on LSB based lateral VDC. It is robust to changes in the tyre properties which otherwise can affect a VDC based on a tyre model. The control and estimation are computationally inexpensive as nonlinear tyre models are not needed. However, the LSB technology requires further development to make it more robust, accurate and independent of additional measurements. The LSB sensor might be sensitive to the bearing wear and the sensor offset drift can be problematic. These aspects should be studied. Finally, a production cost-benefit analysis is necessary. Such a cost analysis can not only help us understand its feasibility and benefits, but also attract potential industrial collaboration and funding.

The PhD Candidate is of the opinion that the LSB technology has the potential to improve vehicle active safety systems, autonomous driving technologies and cooperative driving technologies. For example, the road-tyre friction estimator in Chapter 5 can be used in a cooperative driving environment such that if a vehicle detects a change in friction, it can communicate the change to the vehicles behind to improve the cooperative driving safety as well as throughput. The TUCC proposed in Chapter 3 can be used in new Active Steering Systems designs for better tyre usage and vehicle safety. The friction estimator in Chapter 5 uses combined tyre force and combined tyre slip; similary, Anti-lock Braking System (ABS) design based on combined tyre force and/or combined tyre slip can be an interesting line of research as it may potentially improve ABS performance during combined tyre slip situations. Another interesting line of research is utilizing the LSB measurements to update the tyre models real-time. For example, the LSB measurements while driving the vehicle on a normal day, whether the road is wet or dry or snowy, can be used in combination with other available measurements and estimates to update the tyre model parameters real-time. This can potentially improve many of the existing VDCs and VSEs as they use tyre models. Overall, this dissertation offers a positive recommendation on LSB based VDC and VSE but more work needs to be done.

REFERENCES

[1] Statistical report, “Number of passenger cars and commercial vehicles in use worldwide from 2006 to 2013," *Statista - The Statistics Portal*, 2015.

[2] “The Dutch Automated Vehicle Initiative," ©2015DAVI. http://davi.connekt.nl/

[3] “The Netherlands to become a test country for self-driving cars," *Government of the Netherlands*, The Hague, 23 January 2015.

[4] M. P. Gerard, “Global chassis control and braking control using tyre forces measurement," *Doctoral dissertation, Delft University of Technology*, 2011.

[5] M. Doumiati, O. Sename, J. Martinez and L. Dugard, “Vehicle yaw control via coordinated use of steering/braking systems," *IFAC World Congress*, 2011.

[6] T. Shim and D. Margolis, “Using μ Feedforward for Vehicle Stability Enhancement," *Vehicle Systems Dynamics*, vol. 35, issue 2, 2001, pp. 103-119.

[7] A.K. Madhusudhanan, M. Corno, B. Bonsen and E. Holweg, “Solving Algebraic Riccati Equation real time for Integrated Vehicle Dynamics Control," *2012 American Control Conference*, Montreal, Canada, pp. 3593-3598, 27-29 June 2012.

[8] K.R. Buckholtz, “Use of Fuzzy Logic in Wheel Slip Assignment - Part I: Yaw Rate Control," *SAE 2002 World Congress*, Detroit, 2002.

[9] Y. Fukada, “Slip-Angle Estimation for Vehicle Stability Control", *Vehicle System Dynamics: International Journal of Vehicle Mechanics and Mobility*, vol. 32, issue 4-5, pp. 375-388, 1999.

[10] M. Abe, A. Kato, K. Suzuki and Y. Kano, “Estimation of Vehicle Side-Slip Angle for DYC by Using On-Board-Tire-Model" *AVEC 1998 Proceedings of 4th International Symposium on Advanced Vehicle Control*, Sep. 14-18, Nagoya, 1998.

[11] E. Bakker, L. Nyborg and H.B. Pacejka, “Tyre Modeling for use in Vehicle Dynamics Studies," SAE Technical Paper No. 870421.

[12] F. Braghin, M. Brusarosco, F. Cheli, A. Cigada, S. Manzoni and F. Mancosu, (2006), “Measurement of contact forces and patch features by means of accelerometers fixed inside the tire to improve future car active control," *Vehicle System Dynamics: International Journal of Vehicle Mechanics and Mobility*, 44:sup1, 3-13, DOI: 10.1080/00423110600867101

[13] B.G. Van Leeuwen, E.G.M. Holweg, F. Wit, E. Zaaijer and S. Ballegooij, (2005) *U.S. Patent No. 6,920,801*, Washington, DC: U.S. Patent and Trademark Office.

[14] M. Corno, M. Gerard, M. Verhaegen and E. Holweg, "Hybrid ABS Control Using Force Measurement," *IEEE Transactions on Control Systems Technology*, vol. 20, no. 5, pp. 1223-1235, September 2012.

[15] E. de Bruijn, M. Gerard, M. Corno M. Verhaegen and E. Holweg, "On the performance increase of wheel deceleration control through force sensing," *IEEE International Conference on Control Applications*, Yokohama, Japan, pp. 161-166, Sept. 2010.

[16] M. Gerard, M. Corno, M. Verhaegen, E. Holweg, "Force-Based ABS Control Using Lateral Force Measurement," *ASME 2011 Dynamic Systems and Control Conference and Bath/ASME Symposium on Fluid Power and Motion Control (DSCC2011)*, Arlington, Virginia, USA, vol. 2, pp. 831-837, 2011.

[17] A.K. Madhusudhanan, M. Corno and E. Holweg, "Lateral Vehicle Dynamics Control Based On Tyre Utilization Coefficients and Tyre Force Measurements," 52^{nd} *IEEE Conference on Decision and Control*, Florence, Italy, pp. 2816-2821, 10-13 December 2013.

[18] "CarSim Math Models," *Mechanical Simulation Corporation Brochures & Tech Memos*, September 2012.

[19] R.A. DeCarlo, S.H. Zak and G.P. Matthews, "Variable structure control of nonlinear multivariable systems: a tutorial," *Proceedings of the IEEE*, vol. 76, no. 3, pp. 212-232, 1988.

[20] B. Tongue, "Two brains, one car - actively controlled steering", *IEEE Control Systems Magazine*, vol. 25, no. 5, pp. 14-17, Oct. 2005.

[21] P. Yih and J.C. Gerdes, "Modification of vehicle handling characteristics via steer-by-wire", *IEEE Transactions on Control Systems Technology*, vol. 13, no. 6, pp. 965-976, Nov. 2005.

[22] D. Gualino and I.-J. Adounkpe, "Force-Feedback System Design for the Steer-By-Wire: Optimisation and Performance Evaluation," *2006 IEEE Conference in Intelligent Transportation Systems Conference*, pp.181-187, 17-20 Sept. 2006.

[23] R. Rajamani, G. Phanomchoeng, D. Piyabongkarn and J.Y. Lew, "Algorithms for Real-Time Estimation of Individual Wheel Tire-Road Friction Coefficients," *IEEE/ASME Transactions on Mechatronics*, vol.17, no. 6, pp. 1183-1195, Dec. 2012.

[24] J. Villagra, B. d'Andrea-Novel, M. Fliess and H. Mounier, "A diagnosis-based approach for tire-road forces and maximum friction estimation," *Control Engineering Practice*, vol. 19, no. 2, pp. 174-184, February 2011.

[25] R. Ghandour, A. Victorino, M. Doumiati and A. Charara, “Tire/road friction coefficient estimation applied to road safety," *18th Mediterranean Conference on Control & Automation (MED)*, pp. 1485-1490, 23-25 June 2010.

[26] C.P. Hartweg, “Fahrzeugstabilisierung durch reifenmodellbasierte Schätzung des Kraftschlusspotentials," FKA, 2011.

[27] C. Edwards and S.H. Spurgeon, “Robust output tracking using a sliding-mode controller/observer scheme," *International Journal of Control*, vol. 64, no. 5, pp. 967-983.

[28] “Federal Motor Vehicle Safety Standards (FMVSS) No. 126 - Electronic Stability Control Systems," *National Highway Traffic Safety Administration, U.S. Department of Transportation*, March 2007.

[29] A. Erke, “Effects of electronic stability control (ESC) on accidents: A review of empirical evidence," *Accident Analysis & Prevention*, vol. 40, no. 1, pp. 167-173, January 2008.

[30] R. Sivinski, “Crash Prevention Effectiveness of Light-Vehicle Electronic Stability Control: An Update of the 2007 NHTSA Evaluation," *National Center for Statistics and Analysis, National Highway Traffic Safety Administration*, Washington DC, June 2011.

[31] E. Esmailzadeh, A. Goodarzi and G.R. Vossoughi, "Optimal yaw moment control law for improved vehicle handling," *Mechatronics*, vol. 13, no. 7, pp. 659-675, September 2003.

[32] S. Zheng, H. Tang, Z. Han and Y. Zhang, “Controller design for vehicle stability enhancement," *Control Engineering Practice*, vol. 14, no. 12, pp. 1413-1421, December 2006.

[33] J.H. Park and W.S. Ahn, “H_∞ Yaw-moment control with brakes for improving driving performance and stability," *Proceedings of the 1999 IEEE/ASME International Conference on Advanced Intelligence Mechatronics*, Atlanta, September, 1999.

[34] N. Ding and S. Taheri, “An adaptive integrated algorithm for active front steering and direct yaw moment control based on direct Lyapunov method," *Vehicle System Dynamics*, vol. 48, no. 10, pp. 1193-1213, 2010.

[35] A.K. Madhusudhanan, M. Corno, B. Bonsen and E. Holweg, “Solving Algebraic Riccati Equation real time for Integrated Vehicle Dynamics Control," *American Control Conference 2012*, pp. 3593-3598, June 2012.

[36] A.T. Van Zanten, “Evolution of electronic control systems for improving the vehicle dynamic behavior," *Proceedings of the 6th International Symposium on Advanced Vehicle Control*, 2002.

[37] H.E. Tseng, B. Ashrafi, D. Madau, T. Allen Brown and D. Recker, “The development of vehicle stability control at Ford," *IEEE/ASME Transactions on Mechatronics*, vol. 4, no. 3, pp. 223-234, September 1999.

[38] Karl J. Astrom and and B. Wittenmark, “Adaptive control," *Courier Dover Publications*, 2013.

[39] Hassan K. Khalil, “Nonlinear systems," Third edition, *Upper Saddle River: Prentice hall*, 2002.

[40] F.W. Kienhofer, J.I. Miller and D. Cebon, “Design concept for an alternative heavy vehicle ABS system," *Vehicle System Dynamics*, vol. 46, supplement 1, pp. 571-583, 2008.

[41] K. Reif, “Bosch Professional Automotive Information: Fundamentals of Automotive and Engine Technology," Springer Fachmedien Wiesbaden, 2014.

[42] A. Hoye, “The effects of Electronic Stability Control (ESC) on crashes - An update," Accident Analysis & Prevention, vol. 43, no. 3, pp. 1148-1159, May 2011.

[43] H.E. Tseng, B. Ashrafi, D. Madau, T. Allen Brown and D. Recker, “The development of vehicle stability control at Ford," *IEEE/ASME Transactions on Mechatronics*, vol. 4, no. 3, pp. 223-234, September 1999.

[44] L. Alvarez, J. Yi, R. Horowitz and L. Olmos, “Dynamic Friction Model-Based Tire-Road Friction Estimation and Emergency Braking Control," *ASME Journal of Dynamic Systems, Measurement, and Control*, vol. 127, no. 1, pp 22-32, March 2005.

[45] C. Lee, K. Hedrick and K. Yi, “Real-time slip-based estimation of maximum tire-road friction coefficient," *IEEE/ASME Transactions on Mechatronics*, vol. 9, no. 2, pp. 454-458, June 2004.

[46] S. Muller, M. Uchanski, K. Hedrick, “Estimation of the Maximum Tire-Road Friction Coefficient," *ASME Journal of Dynamic Systems, Measurement, and Control*, vol. 125, no. 4, pp 607-617, 2004.

[47] C. Ahn, H. Peng and H.E. Tseng, “Estimation of road friction for enhanced active safety systems: Dynamic approach," *in Proceedings of the 2009 American Control Conference*, pp 1110-1115, 10-12 June 2009.

[48] G. Baffet, A. Charara and G. Dherbomez, “An Observer of Tire-Road Forces and Friction for Active Security Vehicle Systems," *IEEE/ASME Transactions on Mechatronics*, vol. 12, no. 6, pp. 651-661, December 2007.

[49] N. Ding and S. Taheri, “Application of Recursive Least Square Algorithm on Estimation of Vehicle Sideslip Angle and Road Friction," *Mathematical Problems in Engineering*, vol. 2010, Article ID 541809, 18 pages, 2010.

[50] Y. Zhang, J. Yi, T. Liu, “Embedded Flexible Force Sensor for In-Situ Tire-road Interaction Measurements," *IEEE Sensors Journal*, vol. 13, no. 5, pp. 1756-1765, May 2013.

[51] K. Nam, H. Fujimoto, Y. Hori, "Motion control of electric vehicles based on robust lateral tire force control using lateral tire force sensors," *2012 IEEE/ASME International Conference on Advanced Intelligent Mechatronics (AIM)*, pp. 526-531, 11-14 July 2012.

[52] K. Nam, H. Fujimoto and Y. Hori, "Advanced motion control of electric vehicles based on robust lateral tire force control via active front steering," *IEEE/ASME Transactions on Mechatronics*, vol. 19, no. 1, pp. 289-299, 2014.

[53] D. Gunji and H. Fujimoto, "Measurement Performance Evaluation of Lateral Tire Force Sensor for Yaw-rate Control of Electric Vehicle," *EVTeC and APE Japan 2014, Society of Automotive Engineers of Japan*, 2014.

[54] G. Lin, H. Pang, W. Zhang, D. Wang, and L. Feng, "A self-decoupled three-axis force sensor for measuring the wheel force," *Proceedings of the Institution of Mechanical Engineers, Part D: Journal of Automobile Engineering*, 2013.

[55] A. K. Madhusudhanan, M. Corno and E. Holweg, "Sliding Mode Based Lateral Vehicle Dynamics Control Using Tyre Force Measurements," *Vehicle System Dynamics*, vol. 53, no. 11, pp. 1599-1619, 2015.

[56] A. K. Madhusudhanan, M. Corno and E. Holweg, "Vehicle Sideslip Estimation Using Tyre Force Measurements," *the 23rd Mediterranean Conference on Control & Automation*, Torremolinos, Spain, June 16-19, 2015.

[57] A. K. Madhusudhanan, M. Corno and E. Holweg, "Vehicle Sideslip Estimator using Load Sensing Bearings," *Control Engineering Practice*, 2016. Accepted.
doi: 10.1016/j.conengprac.2016.05.008

[58] A. K. Madhusudhanan, M. Corno and E. Holweg, "Vehicle Yaw Rate Control Using Tyre Force Measurements," *the 14th European Control Conference*, Linz, Austria, July 15-17, 2015.

[59] A. K. Madhusudhanan, M. Corno, M. A. Arat and E. Holweg, "Load Sensing Bearing Based Road-Tyre Friction Estimation Considering Combined Tyre Slip," *Mechatronics*, 2016. Article in press.
doi: 10.1016/j.mechatronics.2016.03.011

[60] B. G. Van Leeuwen, E. G. M. Holweg, F. Wit, E. Zaaijer and S. Ballegooij, "Measurement device for measuring radial and/or axial forces," *U.S. Patent No. 6,920,801*. July 2005.

[61] J. J. Van Doornik, "Haptic feedback on the steering wheel near the vehicles handling limits using wheel load sensing," *Master thesis*, Delft University of Technology, the Netherlands, 2014.

[62] "Vehicle Dynamics & Durability," *Kistler Brochures*, www.kistler.com.

[63] S. M. Savaresi and M. Tanelli. "Active braking control systems design for vehicles," *Springer Science & Business Media*, ISBN 978-1-84996-349-7, 2010.

[64] S. Sastry and M. Bodson, "Adaptive control: stability, convergence and robustness," *Prentice Hall, Englewood Cliffs, New Jersey*, ISBN 0-13-004326-5, 1989.

[65] U. Kiencke and L. Nielsen, "Automotive Control Systems for Engine, Driveline, and Vehicle," *Springer-Verlag Berlin Heidelberg 2005*, ISBN 3-540-23139-0, Vehicle Modelling Chapter, pp. 301-349.

[66] "CarSim Tyre Models," *Mechanical Simulation Corporation Brochures & Tech Memos*, September 2012.

[67] M. Abe, Y. Kano, K. Suzuki, Y. Shibahata and Y. Furukawa, "Side-slip control to stabilize vehicle lateral motion by direct yaw moment," *Society of Automotive Engineers of Japan Review*, vol. 22, no. 4, pp. 413-419, October 2001.

[68] R. Tchamna and I. Youn, "Yaw rate and side-slip control considering vehicle longitudinal dynamics," *International Journal of Automotive Technology*, vol. 14, no. 1, pp. 53-60, February 2013.

[69] Y. Shibahata, K. Shimada and T. Tomari, "Improvement of Vehicle Maneuverability by Direct Yaw Moment Control," *Vehicle System Dynamics: International Journal of Vehicle Mechanics and Mobility*, vol. 22, no. 5-6, pp. 465-481, 1993.

[70] Van Zanten, Anton T., R. Erhardt and G. Pfaff, "VDC, the vehicle dynamics control system of Bosch," *SAE Technical Paper*, no. 950759, 1995.

[71] S. Inagaki, I. Kshiro and M. Yamamoto, "Analysis on vehicle stability in critical cornering using phase-plane method," *Proceedings of the International Symposium on Advanced Vehicle Control*, Tsukuba-shi, Japan, 1994.

[72] J. Ryu, E. J. Rossetter and J. C. Gerdes, "Vehicle sideslip and roll parameter estimation using GPS," *In Proceedings of the AVEC International Symposium on Advanced Vehicle Control*, 2002.

[73] J. Stephant, A. Charara and D. Meizel, "Virtual sensor: application to vehicle sideslip angle and transversal forces," *IEEE Transactions on Industrial Electronics*, vol. 51, no. 2, pp. 278,289, April 2004.

[74] J. Stephant, A. Charara and D. Meizel, "Evaluation of a sliding mode observer for vehicle sideslip angle," *Control Engineering Practice*, vol. 15, no. 7, pp. 803-812, July 2007.

[75] G. Baffet, A. Charara and D. Lechner, "Estimation of vehicle sideslip, tire force and wheel cornering stiffness," *Control Engineering Practice*, vol. 17, no. 11, pp. 1255-1264, November 2009.

[76] Seung-Han You, Jin-Oh Hahn and H. Lee, "New adaptive approaches to real-time estimation of vehicle sideslip angle," *Control Engineering Practice*, vol. 17, no. 12, pp. 1367-1379, December 2009.

[77] G. Phanomchoeng, R. Rajamani, and D. Piyabongkarn, “Nonlinear observer for bounded Jacobian systems, with applications to automotive slip angle estimation" *IEEE Transactions on Automatic Control*, vol. 56, no. 5, pp. 1163-1170, 2011.

[78] J. Farrelly, P. Wellstead, “Estimation of vehicle lateral velocity," *Proceedings of the 1996 IEEE International Conference on Control Applications*, pp. 552-557, September 1996.

[79] J. Oh, Y. Noh and S. B. Choi, “Real-time offset error compensation of 6D IMU mounted on ground vehicles using disturbance observer," *Proceedings of the International Conference on Intelligent Information and Networks*, Male, Maldives, February 2013.

[80] D. Piyabongkarn, R. Rajamani, J. A. Grogg and J. Y. Lew, “Development and experimental evaluation of a slip angle estimator for vehicle stability control," *IEEE Transactions on Control Systems Technology*, vol. 17, no. 1, pp. 78-88, 2009.

[81] G. Panzani, M. Corno, M. Tanelli, S. M. Savaresi, A. Fortina and S. Campo, “Control-oriented vehicle attitude estimation with online sensors bias compensation," *ASME 2009 Dynamic Systems and Control Conference*, Hollywood, USA, pp. 819-826, January 2009.

[82] R. E. Kalman, “A new approach to linear filtering and prediction problems," *Transactions of the ASME-Journal of Fluids Engineering*, vol. 82, Series D, pp. 35-45, 1960.

[83] M. Verhaegen and V. Verdult (2007), *Filtering and System Identification: A Least Squares Approach*, Cambridge University Press, New York.

[84] D. M. Bevly, J. Ryu and J. C. Gerdes, “Integrating INS sensors with GPS measurements for continuous estimation of vehicle sideslip, roll, and tire cornering stiffness," *IEEE Transactions on Intelligent Transportation Systems*, vol. 7, no. 4, pp. 483-493, 2006.

[85] J. G. Ryan and D. M. Bevly “On the Observability of Loosely Coupled Global Positioning System/Inertial Navigation System Integrations With Five Degree of Freedom and Four Degree of Freedom Inertial Measurement Units," *Journal of Dynamic Systems, Measurement, and Control*, vol. 136 no. 2, 021023, March 2014.

ACKNOWLEDGEMENTS

It is overwhelming to write this part of the dissertation as it makes you think about the past four years and the people who influenced these four years. First of all, I would like to thank Matteo for being an amazing promotor. Although you moved to Italy in the first year of my PhD, I appreciate our regular and efficient skype meetings. I also appreciate your efforts in guiding me how to write scientific articles. I would also like to thank my promotor, Edward, for being optimistic even in the face of uncertainties and for your encouragement throughout the past four years. I must also add that your contribution in teaching me how to make effective presentations is quite big. I would also like to thank Arturo for the helpful discussions when the road ahead was uncertain. I thank the anonymous conference and journal reviewers for their valuable contribution. I also thank TNO Automotive, Helmond and SKF Automotive Division, Nieuwegein for their support. A big thanks to everyone at the PME department for the numerous coffee breaks and social events.

I would like to thank Andrea for suggesting Leiden when I was looking for a socially active city for international students. It improved my work-life balance dramatically. I would also like to thank organizers of the International Student Network Leiden for the movie nights, cooking nights, day trips and much more! Carl, I enjoyed our regular drinks at De Twee Spieghels and I wish you the best. Ken, thank you for being a good friend and I enjoyed our trips to Barcelona, Lille and Belgian exclaves. Wolfgang, I enjoyed hanging out with you in Leiden and Rotterdam, and I wish you good luck with your new life in Munich. Thanks for being a good friend. Jannie, our random city walks were one of a kind and thanks for being a good friend. Gulnaz, I enjoyed our philosophical talks. Swathi, thank you for being a good friend and I wish you good luck at EPFL. I would also like to thank PromooD and ISN Leiden yoga club for allowing me to volunteer as a board member.

Priyanka, Rajeev and Reddy, thank you for being good friends and for finding time to visit us in Kerala. Finally and most importantly, I would like to thank my family for their support, without which I would not have made it. Lakshmi, thank you for your patience and not kicking me out while I was working on the thesis during weekends!

CURRICULUM VITÆ

Anil KUNNAPPILLIL MADHUSUDHANAN

Anil Kunnappillil Madhusudhanan was born in Thodupuzha, India on 20 August 1985. He received Bachelor of Technology in Electronics and Communication Engineering from Motilal Nehru National Institute of Technology, Allahabad, India in 2006. During the years 2006 to 2009, he worked at STMicroelectronics (Greater Noida, India), Indian Institute of Science (Bangalore, India) and Cranes Software (Bangalore, India) for one year each.

He went abroad for higher studies in 2009 and received Master of Science *Cum Laude* in Systems and Control from Delft University of Technology (TU Delft), The Netherlands in 2011. During the years 2011 to 2015, he did PhD reseach at TU Delft in the area of Lateral Vehicle Dynamics Control and Vehicle State Estimation using Tyre Force Measurements under the supervision of Prof. Edward Holweg of TU Delft and Prof. Matteo Corno of Politecnico di Milano, Italy. He is now working at the Netherlands Organization for Applied Scientific Research (TNO) as a Junior Scientist Innovator at their Vehicle Dynamics Estimation and Control research group.

List of Publications

1. A. K. Madhusudhanan, M. Corno and E. Holweg, “Sliding Mode Based Lateral Vehicle Dynamics Control Using Tyre Force Measurements," *Vehicle System Dynamics*, vol. 53, no. 11, pp. 1599-1619, 2015.
   doi: 10.1080/00423114.2015.1066018

2. A. K. Madhusudhanan, M. Corno, M. A. Arat and E. Holweg, “Load Sensing Bearing Based Road-Tyre Friction Estimation Considering Combined Tyre Slip," *Mechatronics*, 2016. Article in press.
   doi: 10.1016/j.mechatronics.2016.03.011

3. A. K. Madhusudhanan, M. Corno and E. Holweg, “Vehicle Sideslip Estimator using Load Sensing Bearings," *Control Engineering Practice*, 2016. Accepted.
   doi: 10.1016/j.conengprac.2016.05.008

4. A. K. Madhusudhanan, M. Corno and E. Holweg, “Lateral Vehicle Dynamics Control Based On Tyre Utilization Coefficients and Tyre Force Measurements," *the* 52^{nd} *IEEE Conference on Decision and Control*, Florence, Italy, pp. 2816-2821, 10-13 December 2013.
   doi: 10.1109/CDC.2013.6760310

5. A. K. Madhusudhanan, M. Corno and E. Holweg, “Vehicle Sideslip Estimation Using Tyre Force Measurements," *the 23rd Mediterranean Conference on Control & Automation*, Torremolinos, Spain, pp. 88-93, June 16-19, 2015.
   doi: 10.1109/MED.2015.7158734

6. A. K. Madhusudhanan, M. Corno and E. Holweg, “Vehicle Yaw Rate Control Using Tyre Force Measurements," *the 14th European Control Conference*, Linz, Austria, pp. 2582-2587, July 15-17, 2015.
   doi: 10.1109/ECC.2015.7330926